MODELING AND EVALUATING THE DISPERSION OF AN UNDERWATER SOUR GAS RELEASE IN SHALLOW WATERS

A Thesis

by

WAFA IMRAN

Submitted to the Office of Graduate and Professional Studies of
Texas A&M University
in partial fulfillment of the requirements for the degree of

MASTER OF SCIENCE

Chair of Committee,	Konstantinos Kakosimos
Committee Members,	Luc Véchot
	Aziz Rahman
Head of Department,	Arul Jayaraman

August 2020

Major Subject: Chemical Engineering

ABSTRACT

In the ocean, at offshore production facilities, subsea gas releases can occur from the rupture of subsea pipelines, failure in flow lines, gas export lines and subsea equipment. There have been many subsea gas release incidents in the oil and gas industry, where natural gas is released. An increasing numbers of sour gas reserves are being found, with a high number within the Middle East. The release of sour gas can cause toxic exposure, fire and explosion issues, leading to major environmental and safety impacts. Therefore it is important to understand the phenomena of subsea gas release as it will aid in controlling and quantifying the risks associated with it. From literature it is found that Computational Fluid Dynamics (CFD) models are developed to quantify the severity of risks associated with subsea releases of natural gas. The usage of CFD models is expensive and time consuming hence in this project a nomograph was generated in order to extract data for risk assessment in an easier and more efficient way. In order to do so a transient, Eulerian-Eulerian CFD model was developed to model the release of sour gas in shallow waters to obtain simulation results to construct the nomograph. The model was validated against Engebretsen's 1997 experiment. The simulation results showed excellent agreement with the experimental data. The validated model was expanded to predict the behavior of the bubble plume for several scenarios for Qatar's industry, for release depths between 25 and 100 m, release mass flow rates between 20 and 80 kg/s, release hole diameters between 0.05 and 0.25 m and sour gases with H_2S compositions of 11 and 22 % by mass. A sensitivity analysis was performed that indicated high concentrations of CH_4 and H_2S on the surface, suggesting that dispersion modelling be carried out to determine what offshore facilities are within the vicinity of flammable and toxic clouds. The results obtained from the expanded CFD model include surface mass flux, rise time

and surface gas concentrations. Using the results a nomograph was generated in order to extract data for risk assessment.

DEDICATION

This thesis is dedicated to my family, specifically my parents, Mr. Imran Mushtaq and Mrs. Nahid Imran. Thank you for teaching me the value of education and motivating me to further study and obtain a Master's degree. My parents have always provided me with endless support, love, affection and care. Thank you for always being by my side. I thank God every day for the most wonderful and beautiful parents and family given to me.

ACKNOWLEDGMENTS

I would like to thank the Mary Kay O'Connor Process Safety Center at Qatar for allowing me to work on this project, and the member industry companies for their support and encouragement.

I would like to give a special thanks to my committee chair, Dr. Konstantinos Kakosimos for his guidance, patience, support, encouragement and time throughout the course of the research project. I would also like to thank Dr. Luc Véchot, my committee member, for his continuous support, encouragement and time. Also for the opportunities he provided me throughout the course of my research, by giving me exposure to individuals from the industry. Thanks to my third committee member, Dr. Aziz Rahman for his cooperation, support and time. Without my committee this would not have been possible.

Thanks to the Research Computing department of Texas A&M University at Qatar for the technical support they have provided me with regarding the use of the supercomputer.

Thanks also go to all my friends and colleagues in the Mary Kay O'Connor Process Safety Center at Qatar, and the Chemical Engineering department faculty for making my time at Texas A&M University memorable. They motivated and supported me throughout all the ups and downs I faced throughout my research. Especially Neil Adia, Ola Srour, Mohammad Lameh and Jack Altwal, without you all I would not have been able to make it this far.

Finally, I would like to thank my parents: Nahid Imran and Imran Mushtaq, my sisters: Mariam Imran and Iman Imran and lastly my brother: Mohammad Ali Alamdar Imran for their motivation, encouragement, patience, support and love. They have always supported me to follow

my dreams and tried to help me to their best abilities to make me happy and achieve my goals. A special heartfelt thanks to my mother for all her prayers to get me where I am now.

CONTRIBUTORS AND FUNDING SOURCES

This work was supervised by a thesis committee consisting of three professors; Dr. Konstantinos Kakosimos and Dr. Luc Véchot from the Chemical Engineering Department and Dr. Aziz Rahman from the Petroleum Engineering Department at Texas A&M University at Qatar.

All the work in the thesis was conducted independently by the student.

The graduate student was funded by the Consortium of Mary Kay O'Connor Process Safety Center at Qatar and a fellowship from Texas A&M University at Qatar.

TABLE OF CONTENTS

Page

ABSTRACT ii

DEDICATION iv

ACKNOWLEDGMENTS v

CONTRIBUTORS AND FUNDING SOURCES vii

TABLE OF CONTENTS viii

LIST OF FIGURES xi

LIST OF TABLES xiv

1 INTRODUCTION 1

2 LITERATURE REVIEW 5

2.1 Governing Physics of Bubble Plume 5
2.2 Mechanisms Governing the Bubble Plume 6
2.2.1 Buoyancy 6
2.2.2 Drag 8
2.2.3 Turbulent Dispersion 8
2.2.4 Gas Dissolution 8
2.2.5 Hydrate Formation 10
2.2.6 Ocean Currents and Stratification 11
2.3 Bubble Size Distribution 13
2.4 Modeling Subsea Gas Release 14
2.4.1 Integral Models 15
2.4.2 CFD Models 20

3 THEORETICAL MODELS USED FOR CFD MODEL 26

3.1 Eulerian-Eulerian Modelling Approach 26
3.1.1 The Continuity Equation Solved in ANSYS Fluent [30] 27
3.1.2 The Momentum Equations Solved in ANSYS Fluent [30] 27
3.1.3 The Energy Equation Solved in ANSYS Fluent [30] 29
3.2 Turbulence Models 29
3.2.1 RANS Equations 31
3.2.2 $k - \varepsilon$ Models 32
3.3 Interfacial Area Concentration 37
3.3.1 Hibiki-Ishii (2000) 38

3.4 Species Transport 41
3.5 Mass Transfer with Multiphase Species Transport 42

4 RESEARCH OBJECTIVES 45

5 METHODOLOGY 47

5.1 Experimental Work Selection 47
5.2 CFD Modeling 48
5.2.1 Geometry 49
5.2.2 Meshing 49
5.2.3 Fluent Setup 49
5.3 Model Validation 50
5.4 Expansion of Model and Sensitivity Analysis 50
5.5 Nomograph Generation 51

6 IMPLEMENTATION OF METHODOLOGY 52

6.1 Selecting Experiment for Validation of CFD Model 52
6.1.1 Engebretsen's Experiment 52
6.2 Design of CFD Model for the Simulation of Underwater Sour Gas Release 53
6.2.1 Creating the Geometry 53
6.2.2 Meshing the Geometry 54
6.2.3 Fluent Setup 56

7 MODEL CONFIGURATION 64

7.1 Geometry Design Selection 64
7.2 Mesh Independence Study 67
7.3 Primary Phase Selection 70
7.4 Turbulence Model Selection 72

8 VALIDATION OF CFD MODEL 76

9 MODEL EXPANSION AND DATA COLLECTION 86

10 SENSITIVITY ANALYSIS 90

10.1 Effect of Mass Release Flow Rate 90
10.2 Effect of H_2S Content in Released Gas 92
10.3 Effect of Release Depth 94
10.4 Effect of Hole Diameter 96

11 DIMENSIONLESS ANALYSIS 98

12 NOMOGRAPH DEVELOPMENT 102

12.1 Steps Preformed to Construct Nomograph 102

12.2 Nomograph and How to Use it 107
12.3 Uncertainty Analysis 110
12.3.1 Assumptions 111
12.3.2 Computation of Uncertainties of Results Obtained from Nomograph 111

13 CONCLUSIONS 116

14 FUTURE WORK 119

REFERENCES 120

LIST OF FIGURES

Page

Figure 1: Reprinted from Olsen et al. (2016) article showing an illustration of the different zones for a subsea gas release.[1] 6

Figure 2: Reprinted from Olsen et al. (2016) article showing a graph indicating the error of using the ideal gas law for different release depths.[1] 7

Figure 3: Reprinted from Janacki et al. (2014) article showing the stability curve for methane and carbon dioxide hydrates. [17] 11

Figure 4: Reprinted from Socolofsky et al. (2011) article showing the behavior of a subsea gas release for pure stratification. [19] 12

Figure 5: Reprinted from Socolofsky et al. (2011) article showing the behavior of a subsea gas release for pure current. [19] 12

Figure 6: Reprinted form Olsen et al. (2016) article showing the change of bubble diameter in the plume when a 1 mm bubble is released at a 2550 m depth.[1] 13

Figure 7: 2-D geometry designed in ANSYS Workbench, based on Engebretsen's experimental setup. 54

Figure 8: An image of the geometry used for generating a mesh finer in the bubble plume region (on the left) and the generated mesh (on the right). 56

Figure 9: UDF for pressure distribution for the boundaries of the water body. 60

Figure 10: Sample job file. 63

Figure 11: Sample journal files. 63

Figure 12: Geometry with circular disk and tube. 64

Figure 13: Comparison of centerline velocity, volume fraction and rise time results for simulations with different geometry design and experiment. 67

Figure 14: Meshes generated with different resolutions to be used for mesh independent study. The meshes differ in the cell sizes in the domain. 68

Figure 15: Comparison of centerline velocity, volume fraction and rise time for simulations with different primary phases and experiment. 72

Figure 16: Comparison of centerline velocity, volume fraction and rise time results for simulations with different turbulence models and experiment. 73

Figure 17: Air volume fraction contours after 8 seconds of release for different release rates. 78

Figure 18: Diagram showing points at which velocity and volume fraction results were taken to perform analysis of CFD results. 79

Figure 19: Comparison of simulation and experimental results for centerline velocity. 80

Figure 20: Comparison of simulation and experimental results for centerline volume fraction results. 82

Figure 21: Comparison of simulation and experimental results for rise time. 84

Figure 22: Comparison of simulation and experimental results for maximum fountain height, for two different volumetric flow rates. 85

Figure 23: Graph showing depth/release rate range of concern. 87

Figure 24: Graph showing the time series of CH_4 surface gas concentration. 88

Figure 25: Effect of mass flow rate on surface mass flux (a), rise time (b), CH_4 surface gas concentration (c), and H_2S surface gas concentration (d) results for underwater gas release from 50 m depth and 15 mm hole diameter. 92

Figure 26: Effect of H_2S content in sour gas on surface mass flux (a), rise time (b), CH_4 surface gas concentration (c), and H_2S surface gas concentration (d) results for underwater gas release of 20 kg/s from 50 m depth and 25 mm hole diameter. 93

Figure 27: Effect of release depth on surface mass flux (a), rise time (b), CH_4 surface gas concentration (c), and H_2S surface gas concentration (d) results for underwater gas release of 80 kg/s from 25 mm hole diameter. 95

Figure 28: Effect of release hole diameter on surface mass flux (a), rise time (b), CH_4 surface gas concentration (c), and H_2S surface gas concentration (d) results for underwater gas release of 20 kg/s from 50 m depth. 97

Figure 29: Correlation matrix showing the correlations between different combinations of the derived dimensionless groups. 102

Figure 30: Graph of Π2 versus Π5 for different hole diameters. 104

Figure 31: Graph used to obtained the correction factor from the given hole diameter and reference hole diameter of 0.05 m 105

Figure 32: Graph of Π4 versus Π2 showing the data points and polynomial fitting. 106

Figure 33: Graph of Π3 versus Π4 showing the data points and linear fitting. 107

Figure 34: Nomograph developed to determine rise time, surface mass flux, and surface gas concentration for subsea release of sour gas (11 % H_2S and 89 % CH_4 by mass) from a rupture in a pipeline, for given release height, release hole diameter and release mass flow. 109

LIST OF TABLES

Page

Table 1: List of known experiments and their release depths and rates. 48

Table 2: Mass diffusivity values used for each pair of species. 57

Table 3: Van't Hoff correlation parameters used in simulations. 59

Table 4: Mesh independence study results. 69

Table 5: Release rates of gas used in the experimental work. 76

Table 6: Mass flow rate of air inputted in the model for the boundary condition. 77

Table 7: Different depths, release rates, hole diameters, hydrogen sulfide content used for sensitivity analysis 87

Table 8: List of all simulations performed and the simulation results. 89

Table 9: Dimensions of all variables used for dimensionless analysis. 98

1 INTRODUCTION

In the ocean, at offshore production facilities, gas spills occur that lead to gas releases ranging from major to minor gas leaks. Subsea gas release can occur from various different causes. For example, rupture of subsea pipelines, failure in flow lines, gas export lines and subsea equipment. Release of gas can also result from corrosion, erosion, and wear in valves and process units. The type of gas release present can be classified into four different categories, including seeps, leaks, ruptures and blowouts. A seep is a release from the seabed, which may occur naturally.[1] A seep is a release where the gas release rate is very low, similar to a minor leak; hence both these releases are undetectable until the release continues for long periods of time.[2] A rupture occurs in an underwater pipeline, and usually results in a major leak that is detected relatively early.[1] Similarly a blowout is also a major leak that occurs in a well, as a result of loss of containment. When releases such as seeps or minor leaks occur there is no significant effect on the surface, not much gas reaches the surface, and so the major hazard associated with such releases are toxic environments for marine life forms.[2] Whereas, in the case of releases such as ruptures or blowouts there is added risk for human life and loss of assets. In an offshore production facility, the gas released is natural gas which consists of methane and impurities, carbon dioxide and hydrogen sulfide. When natural gas is released on the surface it may cause an explosion or fire due to the presence of ignitable components. Some of the gas components are toxic and so when released into the atmosphere can cause asphyxiation. An underwater gas release can have disastrous consequences as it can cause toxic exposure, fire and explosion issues, leading to major environmental and safety impacts.[1]

In the past, several underwater gas release incidents have occurred, in the oil and gas industry. In 1989, in Nigeria, an explosion and fire resulted due to a blowout occurring during a drilling operation in the Al Baz field. The released gas ignited causing the death of the derrick man. Four other crew members died from injuries and drowning after they jumped overboard to escape the fire. In total there were five fatalities, and the rig sank. In 2004 in the North Sea another incident occurred due to a hole in a pipeline. At the Jotun A field, a pressure drop was detected in an export pipeline which was present because of a breach in an export pipeline inlet.[1] Gas released from the pipeline and reached the surface. ExxonMobil, Gassco and Statoil handled the incident in a cooperative effort and the consequences were limited. In 2010, in the Gulf of Mexico a blowout occurred that resulted in the largest offshore oil spill in US history.[1] During a drilling operation at the Deepwater Horizon rig a blowout occurred resulting in an explosion and fire. From this incident, eleven fatalities were reported, and the rig sank. Like the three incidents described above there are many more incidents that have occurred as a result of different types of releases.

Due to the increased demand for energy, in the world, more pipelines and wellheads are being installed increasing the chances of more incidents and the risk to environment, human life and assets. Nowadays there is an increasing number in offshore production of shallow sour gas reserves, leading to greater concern of subsea gas release. Middle East covers a large portion of the world supply of natural gas and many of the reserves present in the Middle East are sour gas reserves. In sour gas reserves, toxic hydrogen sulfide gas is present and the release of such a gas at the surface can have disastrous consequences. Therefore, the risks associated with underwater gas release are severe, and need to be addressed, mitigated and controlled. The key parameters that need to be determined in order to carry out a risk assessment for underwater gas release include; the time taken for the gas to reach the surface, the area of the gas pool created on the surface, and

the gas surface flux rates.[2] Knowing the rise time and the surface area of the gas pool is important as it helps in detecting the leakage and defining the exclusion zones during an emergency. It aids in deciding where to position floating equipment and surface vessels in normal operations and emergency situations.[3] Additionally, it is essential to know the gas surface flux rates as it provides information regarding the existence of fire and health hazards.[2] On a whole, analysis of these parameters can aid in hazard identification, risk analysis and development of emergency response plans for subsea gas release incidents.

The abovementioned key parameters depend on a number of mechanisms that affect the behavior of a subsea gas release. The mechanisms include; buoyancy, drag, turbulence, gas dissolution, ocean currents, stratification, and hydrate formation.[1] In order to understand how these mechanisms affect the behavior of a subsea gas release, the governing physics of a bubble plume need to be understood. Therefore, for the quantification of the risk an understanding of the governing physics and the significant parameters that effect the dispersion of gas resulting from the gas release is required. In order to understand the governing physics of the dispersion of gas resulting from a gas release, simulating a real case scenario is essential, which is expensive. Hence modeling is used. In the past Integral models and Computation Fluid Dynamics (CFD) models were used. Integral models were developed by 'Ditmars and Cederwall' in 1970 [4], 'Fannelop and Sejon' in 1980, 'Milgram' in 1984 [5], and 'Fannelop and Betelini' in 1993 [6]. Integral models had some fluid flow issues and so CFD models were later developed in order to solve the full transient and 3-D Navier-Stokes equations for momentum conservation.[1] CFD models were developed by 'Moros and Dand' in 1990 [6], 'Swan and Moros' in 1993 [7], 'Cloete and Olsen' from 2009 [8], 'Olsen and Skjetne' in 2012 [9] and 2016 [10], 'Wu et al.' in 2017 [11], and 'Chen et al.' in 2018 [3]. Experimental data related to subsea gas release is available but limited. For certain depths and release rates,

experiments have been carried out from which velocity, void fraction and bubble size profiles, and information regarding rise time and surface area can be acquired.[1] The results of such experiments have been used to validate the developed models.

All existing models developed model the subsea release of natural gas. However there is a growing number of sour gas reserves being found, especially in the Middle East. Therefore in this thesis work a three-dimensional, transient CFD model will be developed to model subsea releases of sour gas in shallow waters. Important assessment parameter values will be obtained from the model that will aid in generating a nomograph for subsea gas release which will aid in conducting risk assessments in a more efficient and inexpensive way.

2 LITERATURE REVIEW

2.1 Governing Physics of Bubble Plume

When gas is released underwater a bubble plume is generated. The physics that govern a bubble plume change as it ascends through the water column, hence a bubble plume is split into three main zones, as shown in Figure 1. In the first zone, called the zone of flow establishment, the gas is released into the water body and rises as a bubbling jet or a gaseous jet depending on whether the flow is choked or non-choked, respectively. The initial momentum of the gas dominates the flow of gas in this zone. This zone is relatively small. The plume then enters the zone of flow establishment in which the jet breaks up and the gas rises as dispersed bubbles, due to buoyancy. In this zone momentum is no longer significant and the driving force for the plume is buoyancy. There is drag force acting on the bubbles due to the interactions between the dispersed bubbles and continuous water phase. In this zone, the gas continues to expand due to pressure differences, and water in the vicinity of the plume is entrained. Ocean currents may be present that will cause the bubble plume to sway sideways and move radially. Other mechanisms including turbulence and gas dissolution affect the movement of the bubble plume, as well.[1] As the plume approaches water depths less than the plume radius in enters the third zone, called the surface zone.[12] In the surface zone the gas is released to the atmosphere. The rising water will travel radially away from the plume center, dragging some of the gas away with it. Sometimes the gas and water escape to the atmosphere creating a boil zone. In the boil zone a fountain of water will be seen as water moves up vertically.[1]

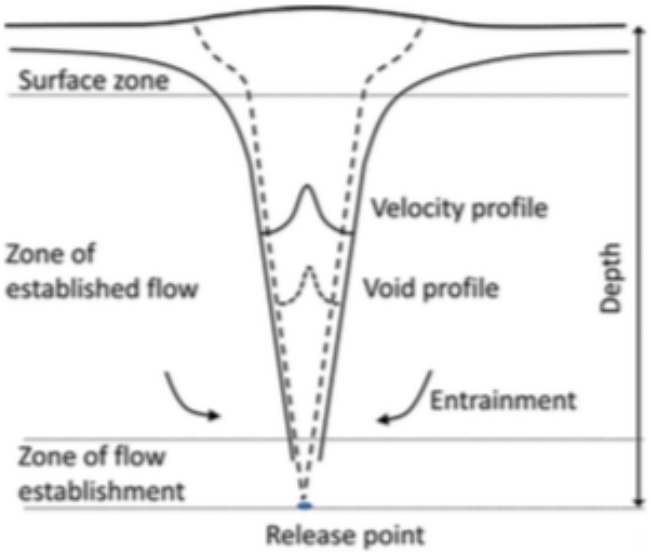

Figure 1: Reprinted from Olsen et al. (2016) article showing an illustration of the different zones for a subsea gas release.[1]

2.2 Mechanisms Governing the Bubble Plume

A number of mechanisms describe the behavior of the bubble plume, including; buoyancy, drag, turbulent dispersion, gas dissolution, hydrate formation, ocean currents and stratification.

2.2.1 Buoyancy

From the available knowledge about a bubble plume, it is known that buoyancy is the main driving force in a bubble plume.[1] Buoyancy force is a result of differences in density between the gas and water body. Density itself is a function of temperature and pressure. The density of a gas increases with increasing pressure and decreasing temperature. In the water body the density of the gas increases with depth, as the temperature and pressure of the water body decreases and increases, respectively. So, as the gas rises through the water column the gas expands. The volume of the gas doubles in the last 10 m below the sea surface.[1] The gas gets strongly compressed as it

goes deeper in the sea. Therefore, in order to quantify the buoyancy force an equation of state needs to be used. In 2016, Olsen analyzed the relative errors of assuming ideal gas law to estimate the buoyancy, by assuming that the gas released was pure methane.[1] The results from the study are shown below in Figure 2.

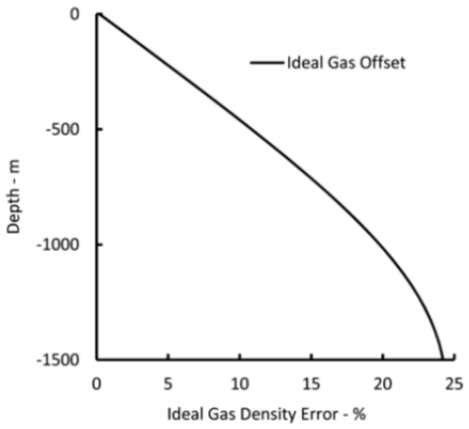

Figure 2: Reprinted from Olsen et al. (2016) article showing a graph indicating the error of using the ideal gas law for different release depths.[1]

From Figure 2 it is observed that as the depth increases the ideal gas density percentage error increases, the assumption of ideal gas law becomes less accurate. Hence it is concluded that assuming ideal gas law is only a valid assumption when the depth of the water body is considered shallow depth.[1] According the Innomar, the seawater depth is classified as shallow when the depth ranges between 25 and 350 m, depths greater than 350 m are considered as deep.[13] Therefore, for this project, assuming that the gas released underwater is an ideal gas is applicable, as the Arabian Gulf has shallow depths only.

2.2.2 Drag

As mentioned above, along with the buoyancy force, drag force acts on the bubbles. The drag force accelerates the water, setting the water in an upward motion. The velocity difference between the moving gas bubbles and water is the variable used to quantify the drag force. This particular velocity difference is called the slip velocity. The slip velocity depends on the drag coefficient, which in turn depends on the bubble size.[1] There are bubbles present with several different sizes and the way in which the slip velocity is approximated depends on assumptions made considering a specific shape for the bubble and the bubble size profile in the plume. The drag force is found based on a mean velocity of the gas bubbles in the plume.[14]

2.2.3 Turbulent Dispersion

In reality the gas bubbles are exposed to instantaneous velocities that are functions of mean velocities and fluctuating components of the velocites.[14] These fluctuations in velocity from the mean velocity give rise to fluctuations in the drag force, which results in turbulent dispersion.[1] Bubble dispersion and water entrainment occur due to turbulence, which then leads to the widening of the plume. Turbulence is a three-dimensional, time-dependent, nonlinear phenomenon.[15] Eddies of different sizes can be visualized in turbulent flow.[16] Turbulent dispersion can be described by using the Navier-Stokes equations.

2.2.4 Gas Dissolution

As the plume ascends through the water column, there is a possibility that the gas will dissolute in the water. When there is a concentration difference of a particular gas component between the gas bubbles and water gas dissolution takes place. In order to quantify the gas dissolution solubility data is required as well as knowledge on the mass transfer coefficients.

Solubility is a function of temperature, pressure and salinity. Mass transfer coefficient is a function of slip velocity, bubble size and diffusivity.[1] Therefore, gas dissolution is considered a mass transfer phenomenon that depends on residence time, slip velocity, solubility, diffusivity and bubble size.[1] Gas dissolution can be described using the following equation[1]:

$$\dot{m}_i = -\pi {d_b}^2 k_i (c_i{}^{sol} - c_i{}^{l}) \qquad \textbf{Equation 1}$$

Where $\dot{m}_i$ is the mass transfer rate of gas component i, d_b is the bubble diameter, k_i is the mass transfer coefficient, $c_i{}^{sol}$ is the solubility, and $c_i{}^{l}$ is the concentration of gas component i in the surrounding liquid.[1]

In 2014, Olsen stated that gas dissolution is a transient process and that it increases with residence time, but then levels off as no more gas can be dissolved. As residence times for deep gas releases are expected to be greater than those of shallow releases, it is known that gas dissolution will have a greater impact on deep releases.[14] Olsen performed a study in 2014 to determine the effect of release depth on methane gas dissolution. The results of the study showed that at 30 m depth and a release rate of 10 kg/s the gas dissolution percentage is 0.3% compared to almost 100% in 300 m at the same flow rate. The study confirms that increase in release depth increases the amount of gas dissolution.[14] The study also showed that as the release rate increases the gas dissolution increases, as at 30 m depth for a release rates of 1 kg/s and 10 kg/s the dissolution percentages were given as 6.7 and 0.3 %, respectively. The study implies that in shallow depths gas dissolution of methane is not significant. However, this may not be the case for any existing hydrogen sulfide particles in the gas, as hydrogen sulfide readily dissolves in water unlike methane. Therefore, the effects of gas dissolution on the behavior of the bubble plume will

be evaluated in this project, to determine the significance of H_2S gas dissolution on the behavior of bubble plumes.

2.2.5 Hydrate Formation

When a gas is released underwater there is potential for gas hydrates to form. Gas hydrates are ice-like compounds composed of water and gas.[17] Gas hydrates are formed in an exothermic reaction at very low temperatures and high pressures where the gas undergoes a first order phase transition.[1] A gas hydrate is a cage-like structure, where a lattice of water molecules encloses gas molecules.[17] Several components present in natural gas can form gas hydrates.

Hydrates are a concern for several reasons. Hydrates can cause the plugging of equipment available for leak detection in the water and enable released gas to travel from the deep sea to shallow depths and then to the surface.[18] When a gas is released underwater, the hydrates formed cause the bubbles in the plume to gain a hydrate skin coating the gas.[1] Moreover, dissolution of the hydrate skin bubbles is then controlled by hydrate solubility instead of gas solubility. This results in more gas reaching the surface. Therefore another danger of hydrate formation is when the gas released contains toxic hydrogen sulfide, which will result in the formation of hydrogen sulfide hydrates and hydrogen sulfide shells for the bubbles, transporting toxic gas to the surface.[18]

The stability curve for methane and carbon dioxide gas hydrates in seawater is shown below in Figure 3. Depending on the water temperature, geothermal gradient, salinity, gas pressure or velocity, methane hydrates in subsea gas operations can be found beyond approximately 300 m depths.[17] As natural gas is composed of mostly methane, it can be assumed that when natural gas is released underwater hydrate formation is only possible or significant at depths greater than 300 m. As only very shallow depths are considered in this project, hydrate formation is neglected.

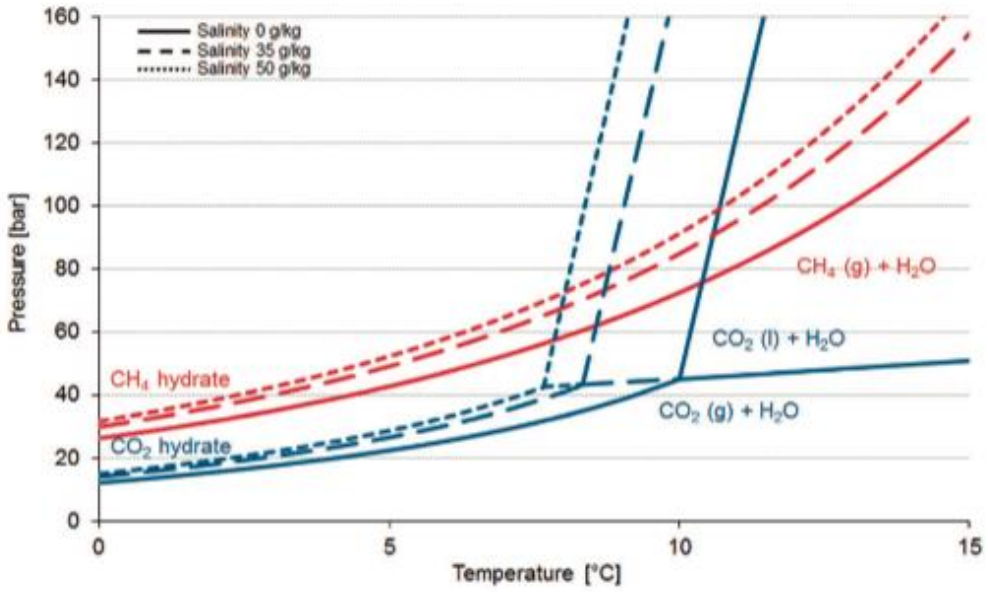

Figure 3: Reprinted from Janacki et al. (2014) article showing the stability curve for methane and carbon dioxide hydrates. [17]

2.2.6 Ocean Currents and Stratification

The bubble plume formed when a subsea gas release occurs is a multiphase plume. The gas can be referred to as a dispersed phase and the water as a continuous phase. The behavior of the multiphase plume depends on stratification and crosscurrents.[19]

In the multiphase plume when the bubbles rise, they entrain water. Due to stratification eventually the negative buoyancy acting on the entrained water becomes larger than the drag force of the bubbles and the water detrains. This forms an outer downdraught plume of seawater and dissolved gas that moves downwards until neutral buoyancy is reached and then spreads laterally. Whereas the bubbles continue to rise as they are still buoyant (Figure 4).[20] Stratification can be defined as a specific water mass or a specific cross-section volume that has different properties, for example, temperature, salinity, and density at different depths. [19]

When there are large horizontal currents in the sea, the entrained fluid in the plume may be separated from the dispersed phase (Figure 5). This may occur at a certain height from the gas release point. Up to this point the bubble behaves as a mixed, coherent plume.[21] The horizontal currents can be defined by the current speed and direction; the speed varies with depth and time. [19]

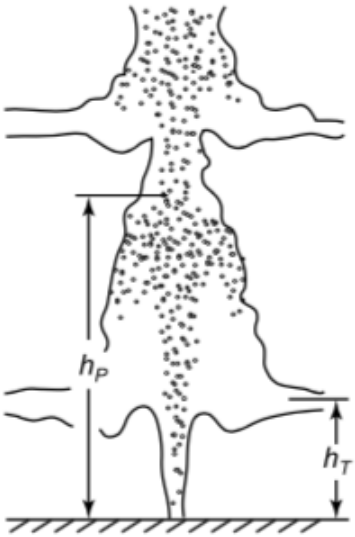

Figure 4: Reprinted from Socolofsky et al. (2011) article showing the behavior of a subsea gas release for pure stratification. [19]

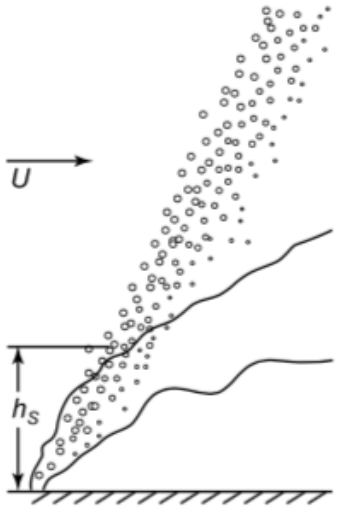

Figure 5: Reprinted from Socolofsky et al. (2011) article showing the behavior of a subsea gas release for pure current. [19]

In this project pure water is used instead of seawater, with a constant density and temperature. It is assumed that ocean currents are insignificant hence overall effects of stratification are neglected.

2.3 Bubble Size Distribution

In the zone of established flow the gas rises as dispersed bubbles. The bubble size is governed by a number of mechanisms; gas expansion, gas dissolution, bubble breakage and bubble coalescence. Bubble breakage may occur due to turbulence. Turbulent eddies may collide with the bubbles causing the bubbles to break down into bubbles with sizes at the turbulent level. Bubble coalescence may occur when neighboring bubbles with small distances between them collide. Therefore the size of the bubbles may change throughout the plume. Figure 6 below shows how the bubble diameter changes with depth, for a 1 mm bubble released under water at a depth of 2550 m.

Depth (m)	Pressure (bar, 100 kPa)	Diameter (mm)
2550	256	1.000
1270	128	1.260
630	64	1.587
310	32	2.000
150	16	2.520
70	8	3.175
30	4	4.000
10	2	5.040
0	1	6.350

Figure 6: Reprinted form Olsen et al. (2016) article showing the change of bubble diameter in the plume when a 1 mm bubble is released at a 2550 m depth.[1]

The size of bubble has an effect on the mechanisms governing the behavior of the bubble plume. For example gas dissolution and drag coefficient depend strongly on bubble size. Therefore in this project a bubble size distribution will be used.

2.4 Modeling Subsea Gas Release

After understanding the several mechanisms that describe the behavior of bubble plumes, key parameters such as rise time, surface area of gas pool, gas surface flux rates can be determined in order to carry out a risk assessment. To study these key parameters realistic subsea gas release experiments need to be conducted, which are costly and extremely dangerous. In the past small scale experiments have been performed to study the key parameters, these experiments were performed by; Kobus in 1968[22], Topham in 1975[23], Milgram in 1983[24], Milgram and Burgess in 1984[5], Loes and Fannelop in 1989, Engebretsen in 1997, Rye and Brandvik in 1997[25] and Johansen in 2003. The experiments only cover a small range of combinations of release depths and gas flow rates compared to most existing depths and flow rates at offshore sites. Therefore the information obtained from these experiments cannot be applied to real-life scenarios in order to carry out risk assessment and emergency planning.[1] Additionally some of these experiments only provide qualitative information, and so models have been designed to provide qualitative as well as quantitative information.[2]

Different types of models have been developed including integral and CFD models. Integral models use sets of governing equations that are based on an integral over the width of the profiles, making the plume models one-dimensional with respect to ocean depth.[1] Whereas, CFD models solve the full transient and three-dimensional Navier-Stokes equations for momentum conservation.[1] Integral models have aided in providing a good representation of the rising bubble plume if the model coefficients (e.g. entrainment coefficient, momentum amplification factor) are tuned properly.[8] The foundation for the integral model was developed by the work of three scientists, Evans, Taylor and Morton et al.[26] From their work many integral models have been developed by: Ditmars and Cederwall in 1970[4], Fannelop and Sjoen in 1980[27], Milgram in 1983[24],

Bettelini and Fannelop in 1993[6] and Einarsrud and Brevik in 2013[28] (Refer to Section 2.4.1).[1] The methods used to develop the models does not allow for accurate result prediction in the surface zone of the bubble plume. Integral models are good to determine parameters only in the zone of established flow. Therefore integral models do not aid in emergency planning when it comes to learning where to place floating equipment and surface vessels in emergency situations.[1] So CFD models are developed that provide information on the bubble plume and the interaction of the bubble plume with the atmosphere. Different CFD models have been developed by: Cloete et al. in 2009[8], Skjetne and Olsen in 2012[9] and 2016[10], Wu et al. in 2017[11], and Chen et al. in 2018[26] (Refer to Section 2.4.2).

2.4.1 Integral Models

In 1956 Morton et al. published a paper 'Turbulent gravitational convection from maintained and instantaneous sources', in which a plume of light gas rising in a stably stratified fluid was modelled. Three main assumptions were made that are the foundation of all integral models:

1. The lateral profiles of velocity and buoyancy are similar at all heights[26]
2. All the fluids are incompressible and the local variations in density are very small relative to the reference density, throughout the whole plume system[26]
3. The rate of entrainment at the edge of the plume is proportional to the mean axial plume velocity[26]

Based on the above-mentioned assumptions, several scientists presented integrals models for two-phase plumes.

In 1970, Ditmars and Cederwall analyzed the behavior of air-bubble plumes. It was assumed that the bubbles rise through water at isothermal conditions. Boussinesq assumption was used to

simplify the momentum equation, so density differences between mixture of gas and fluid and fluid only were neglected. The density differences were only included in the buoyancy terms. Also, it was assumed that lateral velocity profiles and density distributions can be approximated by Gaussian distributions[4]:

$$u = u_m e^{-\frac{r^2}{b^2}} \qquad \textbf{Equation 2}$$

$$(\rho_a - \rho_m) = \Delta\rho_m e^{-\frac{r^2}{\lambda^2 b^2}} \qquad \textbf{Equation 3}$$

Where u is the local mean velocity, u_m is the centerline velocity, b is the nominal half-width of the plume a function of the standard deviation of the velocity profile, ρ_a is the density of the ambient fluid, ρ_m is the local density of the mixture, $\Delta\rho_m$ is the centerline density difference between ρ_a and ρ_m, and λ is the ratio of the lateral spreading of the bubbles to the expansion of the plume.

Ditmars and Cederwall (1970) model covers two and three dimensional cases, their model includes slip velocity between the bubbles and ambient fluid in the plume and gas compressibility. To verify the developed integral model and the proposed theory the results obtained were compared to experimental results from Kobus (1968) experiment. The best comparison of theoretical and experimental results was obtained when λ was less than 1, and the slip velocity was 0.3 m/s. Overall it was found that there was good agreement between the experimental and theoretical observations for plume widths and centerline velocities, for the three-dimensional case. The developed model was simple as it described a single plume driven by buoyancy only. It is a model for the zone of established flow, as it provides no results for the surface zone.[4]

Based on the work of Ditmars and Cederwall (1970), Fannelop and Sjoen (1980) also developed an integral model. They assumed that the density of the gas varies with the vertical distance from the release by a polytropic law, with the following form:[27]

$$\frac{\rho_g(z)}{\rho_{g_0}} = \left(\frac{P(z)}{P_0}\right)^{\frac{1}{n}} \qquad \textbf{Equation 4}$$

Where ρ_{g_0} and $\rho_g(z)$ are the densities of the gas at the seabed and at a vertical distance from the seabed, P and $P(z)$ are the pressures at the seabed and at a vertical distance from the seabed, and n is an adjustable exponent, its value is between 1 and the heat capacity ratio (Cp/Cv).

In their work they represented the buoyancy flux differently to Ditmars and Cederwall. They use tophat as well as Gaussian velocity profiles and include the bubble slip velocity. Similarity and numerical solutions where obtained for two different λ values, 0.8 and 1, using tophat and Gaussian profiles for two gas release flow rates, 20.6 and 38.7 Nm^3/s.[27]

Unlike Ditmars and Cederwall it models the interaction on the free surface as well as for the zone of flow establishment and zone of established flow. In order to present an integral model for the surface zone Fannelop and Sjoen (1980) made a few assumptions. It was assumed that as the plume approaches the surface it is deflected radially outward with little or no loss of momentum. Additionally it was assumed that the horizontal velocity distribution is Gaussian, and that the rate of entrainment of the horizontally spreading flow is proportional to an entrainment coefficient (β), the contact area and centerline velocity.[27] The governing equations for mass and momentum for the plume are shown below: [27]

$$\frac{d}{dr}\left(\pi^{\frac{3}{2}}\rho_w h_w v_m r\right) = 2\pi r \rho_w \beta v_m \qquad \textbf{Equation 5}$$

$$\frac{d}{dr}\left[\left(\frac{\pi^3}{2}\right)^{\frac{1}{2}} \rho_w h_w {v_m}^2 r\right] = 0 \qquad \textbf{Equation 6}$$

Where r is the radial distance, ρ_w is the density, h_w is the thickness of the outward moving layer of the plume, and v_m is the velocity difference.

Fannelop and Sjoen (1980) integral model was verified by performing experiments at 5.5 and 10 m depths. The accuracy of the equations for the surface zone is poor due to the under predication of turbulence in the plume resulting from the interactions on the surface.[27]

Like Fannelop and Sjoen, in 1983 Milgram developed an integral model that includes the interactions of the plume with the surface. Similar to the above mentioned integral models, Milgram (1983) model assume the velocity and density have Gaussian profiles. In addition, Milgram's model uses an isothermal expansion law to represent the density of the gas as a function of water depth using the hydrostatic pressure:[24]

$$\rho_g(z) = \frac{\rho_T(H_B - z)}{H_T} \qquad \textbf{Equation 7}$$

Where H_B is the total pressure head at the level of the gas release, and H_T is the atmospheric pressure head.

The gas volume flux, momentum flux and buoyancy per unit height is expressed in the following form: [24]

$$Gas\ Volume\ Flux, q(z) = 2\pi \int_0^\infty [U(r,z) + U_b]\, f(r,z) r\, dr \qquad \textbf{Equation 8}$$

$$Momentum\ Flux, M(z) = 2\pi\gamma \int_0^\infty (U^2(r,z)\rho_w[1 - f(r,z)] + [U(r,z) + U_b]^2 \rho_g(z) f(r,z)) r\, dr \qquad \textbf{Equation 9}$$

$$Buoyancy, B(z) = 2\pi g \int_0^\infty [\rho_w - \rho_g(z)] f(r,z)) r\, dr \qquad \textbf{Equation 10}$$

Where $U(r,z)$ is the local vertical fluid velocity, U_b is the bubble slip velocity, $f(r,z)$ is the local mean gas fraction given by the expression $f(r,z) = \frac{\rho_w - \rho_p(r,z)}{\rho_w - \rho_g(z)}$, and $\rho_p(r,z)$ is the local mass density of the plume. In the momentum flux equation, γ is the momentum amplification factor, which accounts for the added momentum due to turbulence.

Milgram solved the equations using a numerical integration scheme which approximates the derivatives in z using a finite difference scheme. Afterwards, using Newton iteration it solves for the centerline velocity, centerline gas fraction and plume width. The model results were validated used Kobus (1968) experiment. It was found that the values of slip velocity, λ, and γ are 0.35 m/s, 0.8 and 1, respectively.[24]

All above described integral models do not take into account the transient behavior of the plume. In 1993, Bettelini and Fannelop developed a model for the initial transient behavior of the plume which leads to the generation of an initial spherical cap on the rising plume. Bettelini and Fannelop developed unsteady equations for mass and momentum, and integrated them using numerical Runga-Kutta forth order scheme. The model was tested for a range of entrainment

coefficients. The results were compared with Loes and Fannelop (1989) experimental data. Good agreement was obtained with the experimental results when an entrainment coefficient of 0.15 was used. The model gave an acceptable representation of the behavior of the bubble plume up to the zone of established flow.[6]

2.4.2 CFD Models

There are two main approaches by which CFD can be used to simulate the bubble plume system: Eulerian-Lagrangian and Eulerian-Eulerian approach. In the past, several CFD models have been developed using the Eulerian-Lagrangian approach. Whereas only a few models are present that use the Eulerain-Eulerian method.

2.4.2.1 CFD Models that Use the Eulerian-Lagrangian Method

In 2009, Cleote et al developed a CFD model to simulate the bubble plume and free surface behavior from a subsea gas release occurring as a result of pipeline rupture. A coupled discrete phase model (DPM) and volume of fluid (VOF) model is used. The software used to implement the model is Fluent. In this model the air above the surface and water body are treated as Eulerian phases, which are continuous phases that interact with one another. The bubbles are treated as Lagrangian particles, discrete bubbles. The VOF model is used to solve for the conservation of mass and momentum equations and to sharpen the interface between the phases. The mixture density is given by the following equation[8]:

$$\rho = \sum \alpha_q \rho_q \qquad \textbf{Equation 11}$$

The viscosity is given by the following equation[8]:

$$\mu = \mu_T + \mu_M \qquad \textbf{Equation 12}$$

Where μ_T is the turbulent viscosity, which is given by the standard k-ε turbulence model, and μ_M is the molecular mixture viscosity.

The DPM tracks the discrete bubbles by implementing a force balance on each particle to account for the forces acting on the bubble such as the buoyancy, drag, lift and virtual mass force. The force balance is[8]:

$$\frac{d\overrightarrow{u_p}}{dt} = F_D\left(\vec{u} - \overrightarrow{u_p}\right) + \frac{\vec{g}(\rho_p - \rho)}{\rho_p} + \overrightarrow{F_p} \qquad \textbf{Equation 13}$$

Lift and virtual mass forces may act on the bubbles but are negligible for this model setup. The drag force depends on the bubble size and shape which is accounted for by using a drag coefficient that depends on the Eotvos number. Turbulent dispersion of the particles is accounted for in the model by using a stochastic tracking (random walk) approach. In this approach the fluctuating velocity components are determined by the following equation[8]:

$$u' = \zeta\sqrt{\overline{u'^2}} \qquad \textbf{Equation 14}$$

The amount of time spent by the particle inside of a turbulent eddy governs the amount of turbulent dispersion occurring and is found by the following equation[8]:

$$T_L = C_L\frac{k}{\varepsilon} \qquad \textbf{Equation 15}$$

Where the value recommended for C_L is 0.15.

In this CFD model the abovementioned drag law and a bubble size model is added as user defined functions. The bubble size model is added to account for any mass transfer mechanisms and is described by the equation shown below in the Lagrangian framework[8]:

$$\frac{\partial \rho_b d_b}{\partial t} = \rho_b \frac{{d_b}^{eq} - d_b}{\tau_{rel}} \qquad \textbf{Equation 16}$$

Where ρ_b is the bulk density, τ_{rel} is the relaxation time, and ${d_b}^{eq}$ is the mean equilibrium diameter.

The computational grid used to simulate the model consists of 464 500 cells with 5 cm cells in the plume and 4 cm cells in the surface zone. The model was validated against Engebrsten's experiment. The model showed an excellent agreement with the experimental data. The largest discrepancies were observed when comparing results regarding the surface flow. The model under predicted the surface velocities due to an incomplete turbulence model. In the region of the free surface there is increased turbulent kinetic energy dissipation that was not accounted for. [8]

Skjetne and Olsen modified this model in 2012 and 2016. In 2012, the effects of gas dissolution of methane were implemented into the model. The effects of gas dissolution are expressed by the following equation[9]:

$$\dot{m} = \pi d^2 k_{CH_4} \rho_{H_2O} \left({n_{CH_4}}^{sol} \frac{M_{CH_4}}{M_{H_2O}} - {Y_{CH_4}}^{W} \right) \qquad \textbf{Equation 17}$$

Where M symbolizes the molar weights, Y the mass fractions, n the mole fractions, k is the mass transfer coefficient and d is the bubble diameter. This modeling concept can be used for other gases as well. The model suggested that gas dissolution is only important for large release depths.

In 2016, virtual mass force was added in the force balance shown by Equation 13. In the virtual mass force term fluctuations in the velocity are also accounted for by using the random walk model. In the study carried out in 2016, a through grid dependence study was also conducted in order to determine the effect of the grid on the model results, especially for large-scale scenarios. The model was validated against three experiments, all which where performed by Engebretsen. Comparing the model with one of the experiments showed that the model under predicted the spreading of the plume. This was due to the chosen turbulent model. It is recommended by the author that a more scale resolving turbulence model be used that accounts for bubble induced turbulence. The model performs well for shallow depths, however for deep depths it is found that the correlation chosen to compute the mass transfer coefficient affects the results for the amount of gas dissolution occurring. The study does not aid in determining which correlation should be used in order to obtain the best results.[10]

In 2018, Chen et al developed a CFD model that uses the model principles of Cloete et al 2009 model, with mass transfer effects. However, instead of using a bubble size model in the Lagrangian framework it used a bubble size model in the Eulerian framework that was developed by Laux and Johansen. Another difference in this study from the Cloete et al. model is that it uses the realizable k-ε turbulence model.

The simulation was performed with seawater domain. The software used to implement the model is Fluent. The computational domain was 180 m x 100 m x 110 m, the grid size around the release diameter was 1.5 m and was 1 m around the surface. The boundary conditions used to simulate the model include pressure inlet and outlet, no slip wall, velocity inlet and outlet. The model was validated against experimental data obtained from Engebrsten's experiment. Overall the simulation results agree with the experimental data. It is found that the centerline velocities

found from the model are greater than those of the experiment, and that this difference decreases with an increase in release depth. These discrepancies may be due to the nature of the turbulence model being used. The model also over predicts the momentum transfer from bubble to liquid due to assumptions made in the DPM. The differences presented could be accepted to a certain extent. After the validation of the model, the model was extended to simulate underwater gas release and dispersion behavior in full-scale scenarios.[3]

2.4.2.2 CFD Models that Use the Eulerian-Eulerian Method

In 2017, Wu et al developed a CFD model using the homogenous Multiple Size Group (MUSIG) model. The software used to implement the model is ANSYS CFX software. The model is based on a Eulerian-Eulerian approach, as even the bubbles are modeled using the Eulerian approach. In the MUSIG model the bubbles of different properties are separated into different groups. Conservation of mass equation is solved for each bubble group whereas one momentum conservation equation is solved for all the bubble groups, as it is assumed that all bubbles move with the same velocity. A modified Grace drag model is used to account for the drag force acting on the bubbles. The lift force experienced by the bubbles is also described in this model by using equations presented by the Tomiyama model. Plume coalescence and bubble breakup phenomenon is also accounted for by incorporating the models developed by Prince and Blanch, and Luo and Svendsen, respectively. Effects of the virtual mass force and turbulent dispersion was also added to the model by using available models in the CFD software being used. The computational grid used included approximately one million cells. A mesh sensitivity study was performed in this study to ensure that the results obtained from the model simulation were independent of the grid. The boundary conditions used to simulate the model include, no slip condition on the sides and lower boundaries, and pressure outlet set to atmospheric pressure on the upper boundary.

In this study, four different numerical approaches were used to assess the suitability to model the behavior of the plume. For all four approaches the model was validated against experimental data presented by Fannelop and Sojen in 1980. The different numerical approaches include, standard k-ε turbulence model, modified k-ε turbulence model, Large Eddy Simulation (LES) approach and Scale-Adaptive Simulation (SAS) approach. For all the approaches except for the LES approach, when comparing the model with the experimental data it was found that the model over predicts the centerline velocity and that it under predicts the plume width. The LES approach resulted the most accurate results, however this model requires long simulation times and the use of very small time steps in order to avoid stability issues.[11]

2.4.2.3 Previous Work Conducted by Colleague, Moustafa Ali

In 2018, Moustafa Ali my colleague developed a transient, two-dimensional Eulerian-Eulerian model using the RNG k-ε turbulence model for the subsea release of methane gas. He validated the model against Engebretsen's experimental work. The simulations results showed excellent agreement with the experimental data. He then expanded the model geometry to model the release of methane gas from a depth of 50 m, as this is the average depth of the Arabian Gulf Sea. He tested the expanded model for three different release mass flow rates and determined the effect of mass flow rate on the rise time, surface mass flux and methane percentage on the surface. It was found that as the mass flow rate increases the rise time decreases, the surface mass flux and methane percentage on the surface increases. In this project his developed model is used as a starting point to develop a new CFD model for release of sour gas underwater in the Arabian Gulf Sea.[29]

3 THEORETICAL MODELS USED FOR CFD MODEL

In order to develop a CFD model to study the behavior of bubble plumes an understanding for the following types of theoretical models is required.

3.1 Eulerian-Eulerian Modelling Approach

The process of underwater gas release and dispersion is modelled as a multiphase flow system with the regime of a bubbly flow. In this bubbly flow a discrete gas phase, sour gas, flows through continuous fluid phases, water and the air above the sea surface. Unlike most CFD models developed in the past, the discrete and continuous phases are treated as Eulerian phases, as the multiphase flow is mathematically described using the Eulerian-Eulerian approach. Eulerian-Lagrangian approach is not considered in this project as the amount of computational power and time required to solve a system with increasing dispersed phase hold up with Eulerian-Lagrangian is large as more and more particles have to be tracked. In the Eulerian-Eulerian approach the different phases will be treated as interpenetrating continua. The volume fractions will be computed and are assumed to be continuous functions of time and space. The sum of the volume fractions for the different phases will be equal to 1. Conservation equations are derived for each phase in the controlled volume design.

In ANSYS Fluent there are three types of Eulerian-Eulerian models; Volume of Fluid (VOF), Mixture and Eulerian model. Eulerian model is the most complex multiphase model, as it solves separate momentum and continuity equations for each phase in the system, making it more accurate. The Eulerian model is recommended for applications such as bubbly flows and it can be used to track the bubbles in the system, hence in this project the Eulerian model will be used. In

this model a single pressure is shared by all the phases. In addition all k-ε and k-ω turbulence models can be solved for the individual phases or the mixture. [30]

The Eulerian model solves for the conservation of mass, momentum and energy, the equations are shown below in the following sections.

3.1.1 The Continuity Equation Solved in ANSYS Fluent [30]

$$\frac{1}{\rho_{rq}}\left(\frac{\partial}{\partial t}\left(\alpha_q \rho_q\right) + \nabla.\left(\alpha_q \rho_q \vec{v}_q\right) = \sum_{p=1}^{n}\left(\dot{m}_{pq} - \dot{m}_{qp}\right)\right) \qquad \textbf{Equation 18}$$

Where ρ_{rq} is the volume averaged density of phase q, α_q is the volume fraction of phase q, ρ_q is the physical density of phase q, $\vec{v}_q$ is the velocity of phase q, $\dot{m}_{pq}$ equates to the mass transfer from phase p to phase q and similarly $\dot{m}_{qp}$ equates to the mass transfer from phase q to phase p. [30]

The continuity equation is solved to obtain the volume fraction for each secondary phase in the process, from the solution the primary phase volume fraction can be found. This is possible as the volume fractions sum to one.

3.1.2 The Momentum Equations Solved in ANSYS Fluent [30]

$$\frac{\partial}{\partial t}\left(\alpha_q \rho_q \vec{v}_q\right) + \nabla.\left(\alpha_q \rho_q \vec{v}_q \vec{v}_q\right)$$

$$= -\alpha_q \nabla \mathrm{p} + \nabla.\bar{\bar{\tau}}_q + \alpha_q \rho_q \vec{g} + \sum_{p=`}^{n}\left(K_{pq}\left(\vec{v}_p - \vec{v}_q\right) + \dot{m}_{pq}\vec{v}_{pq}\right. \qquad \textbf{Equation 19}$$

$$\left. - \dot{m}_{qp}\vec{v}_{qp}\right) + \left(\vec{F}_q + \vec{F}_{lift,q} + \vec{F}_{wl,q} + \vec{F}_{vm,q} + \vec{F}_{td,q}\right)$$

Where $\bar{\bar{\tau}}_q$ is the stress-strain tensor for phase q, K_{pq} is the interphase momentum exchange coefficient, $\vec{F}_q$ is an external body force, $\vec{F}_{lift,q}$ is the lift force acting on a secondary phase p in a primary phase q and similarly $\vec{F}_{wl,q}$ is the wall lubrication force, $\vec{F}_{vm,q}$ is the virtual mass force, $\vec{F}_{td,q}$ is the turbulent dispersion force acting on the phase. [30]

The stress-strain tensor is given by the following formula: [30]

$$\bar{\bar{\tau}}_q = \alpha_q \mu_q \left(\nabla \vec{v}_q + \nabla \vec{v}_q{}^T\right) + \alpha_q \left(\lambda_q - \frac{2}{3}\mu_q\right) \nabla \cdot \vec{v}_q \bar{\bar{I}} \qquad \textbf{Equation 20}$$

Where μ_q is the shear viscosity of phase q, λ_q is the bulk viscosity of phase q and $\bar{\bar{I}}$ is the unit tensor. [30]

The interphase momentum exchange coefficient for bubbly flows, such as this system is given as: [30]

$$K_{pq} = \frac{\rho_p f}{6\tau_p} d_p A_i \qquad \textbf{Equation 21}$$

Where, d_p is the particle diameter of phase p and A_i is the interfacial area. τ_p is the particulate relaxation time which is given as: [30]

$$\tau_p = \frac{\rho_p {d_p}^2}{18\mu_q} \qquad \textbf{Equation 22}$$

In this expression μ_q is the viscosity of phase q.

The expression for K_{pq} consists of the term f, it is the drag function described by the expression shown below. [30]

$$f = \frac{C_D Re}{24} \qquad \textbf{Equation 23}$$

In this expression, Re is the relative Reynolds number and C_D is the drag coefficient. The drag coefficient is computed based on the model developed by Schiller and Naumann: [30]

$$C_D = \begin{cases} 24(1 + 0.15Re^{0.687})/Re & Re \leq 1000 \\ 0.44 & Re > 1000 \end{cases} \qquad \textbf{Equation 24}$$

Schiller and Naumann model is used, as it is the default model in fluent, it is applicable for all fluid-fluid pairs of phases, and is very stable. It is recommended as only spherical bubbles are considered in the system. [30]

3.1.3 The Energy Equation Solved in ANSYS Fluent [30]

$$\frac{\partial}{\partial t}(\alpha_q \rho_q h_q) + \nabla.(\alpha_q \rho_q \vec{u}_q h_q) = \alpha_q \frac{dp_q}{dt} + \bar{\bar{\tau}}_q : \nabla \vec{u}_q - \nabla \cdot \vec{q}_q + S_q + \sum_{p=`}^{n} (Q_{pq} + \dot{m}_{pq} h_{pq} - \dot{m}_{qp} h_{qp}) \qquad \textbf{Equation 25}$$

Where h_q is the specific enthalpy of phase q, $\vec{q}_q$ is the heat flux, S_q is a source term consisting of the enthalpies from external sources, Q_{pq} is the intensity of heat exchange between the two phases p and q, and h_{qp} is the interphase enthalpy. [30]

3.2 Turbulence Models

There are two types of flow regimes, laminar and turbulent flow. Laminar flow is a streamline flow, where the fluid layers do not interfere with one another. Turbulent flow is an

irregular, chaotic flow of fluid. Eddies can be visualized, which are the swirling motion of the fluid. In turbulent flow the velocity and pressure changes continuously with time. Turbulence is a 3-D, time dependent, nonlinear phenomena, which is described by Naiver-Stokes equations. The Naiver-Stokes equations are the fundamentals of fluid flow. The Reynolds number is a parameter present in the equations, which gives a measure of the relative importance of inertial and viscous forces. When the Reynolds number is increased beyond 2000, turbulent flow is observed.

A turbulent flow is characterized in terms of mean value of the flow properties and their fluctuating components. This is called Reynolds decomposition, and is described by the following equation: [31]

$$\Phi = \overline{\varphi} + \varphi' \qquad \textbf{Equation 26}$$

Where Φ is the instantaneous value of the flow property, $\overline{\varphi}$ is the time average of the flow property and φ' is the fluctuating component of the flow property.

The time average of the flow property is defined by the following equation: [31]

$$\overline{\varphi} = \frac{1}{\Delta t}\int_0^{\Delta t} \varphi(t)\, dt \qquad \textbf{Equation 27}$$

Where Δt is larger than the time scale of the slowest variation in the flow property.

Several numerical methods have been developed to predict the effects due to turbulence. They are categorized into three main groups: [31]

- Reynolds-Averaged Navier-Stokes (RANS) equations
- Large Eddy Simulation (LES)
- Direct Numerical Simulation (DNS) [31]

3.2.1 RANS Equations

RANS equations are most widely used to model turbulence. RANS equations focus on the effect of turbulence on the mean flow properties. The RANS equations for continuity and momentum are as follows: [31]

$$\frac{\partial \rho}{\partial t} + \frac{\partial}{\partial x_i}(\rho u_i) = 0 \qquad \textbf{Equation 28}$$

$$\frac{\partial}{\partial t}(\rho u_i) + \frac{\partial}{\partial x_j}(\rho u_i u_j) = -\frac{\partial p}{\partial x_i} + \frac{\partial}{\partial x_j}\left[\mu\left(\frac{\partial u_i}{\partial x_j} + \frac{\partial u_j}{\partial x_i} - \frac{2}{3}\delta_{ij}\frac{\partial u_l}{\partial x_l}\right)\right] + \frac{\partial}{\partial x_j}\left(-\rho\overline{u'_i u'_j}\right) \qquad \textbf{Equation 29}$$

The Reynold stresses, $-\rho\overline{u'_i u'_j}$ present in the equation occur from the interactions between the turbulent fluctuations. These terms must be modeled to close the equations. They can be modeled by the following different models: [31]

- Mixing length model
- Spalart-Allmaras model
- $k - \varepsilon$ model
- $k - \omega$ model
- Algebraic stress model
- Reynolds stress model [31]

Mixing length and $k - \varepsilon$ models and the most widely used. In the literature review section, nearly all of the described CFD models use the $k - \varepsilon$ model. The $k - \varepsilon$, $k - \omega$ and Spalart-

Allmaras model use the Boussinesq hypothesis to relate the Reynolds stresses to the mean rates of deformation. [31]

$$-\rho\overline{u'_i u'_j} = \mu_t\left(\frac{du_i}{dx_j}+\frac{du_j}{dx_i}\right)-\frac{2}{3}\left(\rho k+\mu_t\frac{du_k}{dx_k}\right)\delta_{ij} \qquad \textbf{Equation 30}$$

The Boussinesq hypothesis assumes that the turbulent viscosity (μ_t) is isotropic.[30]

In this project $k-\varepsilon$ models will be used to model turbulence, as the existing CFD models suggest it is sufficient to predict good results.

3.2.2 $k-\varepsilon$ Models

There are three types of $k-\varepsilon$ models:

- Standard $k-\varepsilon$ model
- RNG $k-\varepsilon$ model
- Realizable $k-\varepsilon$ model

All three models are two equation models. There are transport equations for the kinetic energy (k) and for the rate of dissipation of kinetic energy (ε). The three models differ in the ways of calculating the turbulent viscosity, model constants, and the formulation of the dissipation rate transport equation.

3.2.2.1 Standard $k-\varepsilon$ Model

The standard $k-\varepsilon$ model assumes that the flow is fully turbulent, and so the effects of molecular viscosity are negligible. The transport equations formed are as follows: [30]

$$\frac{\partial}{\partial t}(\rho k) + \frac{\partial}{\partial x_i}(\rho k u_i) = \frac{\partial}{\partial x_j}\left[\left(\mu + \frac{\mu_t}{\sigma_k}\right)\frac{\partial k}{\partial x_j}\right] - \rho\overline{u'_i u'_j}\frac{\partial u_j}{\partial x_i} + \beta g_i \frac{\mu_t}{Pr_t}\frac{\partial T}{\partial x_i} - \rho\varepsilon - 2\rho\varepsilon\frac{k}{a^2} + S_k \quad \textbf{Equation 31}$$

$$\frac{\partial}{\partial t}(\rho\varepsilon) + \frac{\partial}{\partial x_i}(\rho k\varepsilon u_i) = \frac{\partial}{\partial x_j}\left[\left(\mu + \frac{\mu_t}{\sigma_\varepsilon}\right)\frac{\partial \varepsilon}{\partial x_j}\right] + C_{1\varepsilon}\frac{\varepsilon}{k}\left(-\rho\overline{u'_i u'_j}\frac{\partial u_j}{\partial x_i} + C_{3\varepsilon}\beta g_i \frac{\mu_t}{Pr_t}\frac{\partial T}{\partial x_i}\right) - C_{2\varepsilon}\rho\frac{\varepsilon^2}{k} + S_\varepsilon \quad \textbf{Equation 32}$$

Where μ_t is the turbulent viscosity and is equal to $\rho C_\mu \frac{k^2}{\varepsilon}$, where C_μ is a constant with the value 0.09. $\sigma_k, \sigma_\varepsilon, C_{1\varepsilon}, C_{2\varepsilon}$ are all constants with the values 1, 1.3, 1.44, and 1.92, respectively. The coefficient of thermal expansion is $\beta = -\frac{1}{\rho}\left(\frac{\partial \rho}{\partial T}\right)_p$. g_i is the gravitational vector in the i[th] direction and Pr_t is the turbulent Prantl number for energy, which is a constant for this model with the value 0.85. a is the speed of sound. $C_{3\varepsilon} = \tanh\left|\frac{v}{u}\right|$, where v is the component of the flow velocity parallel to the gravitational vector and u is the component of the flow velocity perpendicular to the gravitational vector.[30]

3.2.2.2 RNG $k-\varepsilon$ Model

The RNG model differs from the standard model, the equations are derived using a statistical technique called renormalization group (RNG) methods. Due to this additional terms

appear in the transport equation to improve the accuracy and reliability of the model for a wider class of flows. [30]

$$\frac{\partial}{\partial t}(\rho k) + \frac{\partial}{\partial x_i}(\rho k u_i) = \frac{\partial}{\partial x_j}\left[a_k \mu_{eff} \frac{\partial k}{\partial x_j}\right] - \rho\overline{u'_i u'_j}\frac{\partial u_j}{\partial x_i} + \beta g_i \frac{\mu_t}{Pr_t}\frac{\partial T}{\partial x_i} - \rho\varepsilon - 2\rho\varepsilon\frac{k}{a^2} + S_k \quad \textbf{Equation 33}$$

$$\frac{\partial}{\partial t}(\rho\varepsilon) + \frac{\partial}{\partial x_i}(\rho\varepsilon u_i) = \frac{\partial}{\partial x_j}\left[a_\varepsilon \mu_{eff} \frac{\partial \varepsilon}{\partial x_j}\right] + C_{1\varepsilon}\frac{\varepsilon}{k}\left(-\rho\overline{u'_i u'_j}\frac{\partial u_j}{\partial x_i} + C_{3\varepsilon}\beta g_i \frac{\mu_t}{Pr_t}\frac{\partial T}{\partial x_i}\right) - C_{2\varepsilon}\rho\frac{\varepsilon^2}{k} - R_\varepsilon + S_\varepsilon \quad \textbf{Equation 34}$$

Where $C_{1\varepsilon}$ and $C_{2\varepsilon}$ are constants equal to 1.42 and 1.68, respectively. The inverse effective Prantl numbers, a_k and a_ε are approximately equal to 1.393.

A differential equation for the turbulent viscosity results from the application of RNG methods, which is used for low Reynolds numbers: [30]

$$d\left(\frac{\rho^2 k}{\sqrt{\varepsilon\mu}}\right) = 1.72\frac{\hat{v}}{\sqrt{\hat{v}^3 - 1 + C_v}}d\hat{v} \quad \textbf{Equation 35}$$

Where $\hat{v} = \frac{\mu_{eff}}{\mu}$ and C_v is approximately 100.

For high Reynolds number the turbulent viscosity is given by the same expression as for the standard model, but the value of the constant C_μ is 0.0845.

The RNG model can also account for the effects of swirl and rotational motion by modifying the turbulent viscosity in ANSYS Fluent. [30]

The additional term in the ε equation, R_ε: [30]

$$R_\varepsilon = \frac{C_\mu \rho \eta^3 (1 - \frac{\eta}{\eta_0})}{1 + \beta \eta^3} \frac{\varepsilon^2}{k} \qquad \textbf{Equation 36}$$

Where $\eta = \frac{Sk}{\varepsilon}$, and η_0 and β are constant with the values 4.38 and 0.012, respectively. This additional term allows the RNG model to accurately predict results for rapidly strained flows.[30]

3.2.2.3 Realizable $k - \varepsilon$ Model

The realizable model consists of a modified equation for the dissipation rate and a different expression for the turbulent viscosity. In has been proven that it performs the best out of the three $k - \varepsilon$ models. [30]

$$\frac{\partial}{\partial t}(\rho k) + \frac{\partial}{\partial x_j}(\rho k u_j) = \frac{\partial}{\partial x_j}\left[\left(\mu + \frac{\mu_t}{\sigma_k}\right)\frac{\partial k}{\partial x_j}\right] - \rho\overline{u'_i u'_j}\frac{\partial u_j}{\partial x_i} + \beta g_i \frac{\mu_t}{Pr_t}\frac{\partial T}{\partial x_i} - \rho\varepsilon - 2\rho\varepsilon\frac{k}{a^2} + S_k \qquad \textbf{Equation 37}$$

$$\frac{\partial}{\partial t}(\rho\varepsilon) + \frac{\partial}{\partial x_j}(\rho\varepsilon u_j)$$

$$= \frac{\partial}{\partial x_j}\left[\left(\mu + \frac{\mu_t}{\sigma_\varepsilon}\right)\frac{\partial \varepsilon}{\partial x_j}\right] + \rho C_1 S\varepsilon - \rho C_2 \frac{\varepsilon^2}{k + \sqrt{v\varepsilon}} \qquad \textbf{Equation 38}$$

$$+ C_{1\varepsilon}\frac{\varepsilon}{k}\left(C_{3\varepsilon}\beta g_i \frac{\mu_t}{Pr_t}\frac{\partial T}{\partial x_i}\right) + S_\varepsilon$$

Where $C_1 = \max\left[0.43, \frac{\eta}{\eta+5}\right]$, $\eta = S\frac{k}{\varepsilon}$, and $S = \sqrt{2S_{ij}S_{ij}}$, $S_{ij} = \left(\frac{\partial u_j}{\partial x_i} + \frac{\partial u_i}{\partial x_j}\right)$. In the equations, $C_{1\varepsilon}, C_2, \sigma_k, \sigma_\varepsilon$ are constants with the values 1.44, 1.9, 1.0 and 1.2, respectively.

The turbulent viscosity is given by the same expression as in the standard model, however the C_μ is no longer constant. [30]

$$C_\mu = \frac{1}{\omega_k + A_s\frac{kU^*}{\varepsilon}} \qquad \textbf{Equation 39}$$

Where $U^* = \sqrt{S_{ij}S_{ij} + \widetilde{\Omega}_{ij}\widetilde{\Omega}_{ij}}$, and $\widetilde{\Omega}_{ij} = \overline{\Omega_{ij}} - \varepsilon_{ijk}\omega_k - 2\varepsilon_{ijk}\omega_k$, $\overline{\Omega_{ij}}$ is the mean rate of rotation tensor relative to the angular velocity, ω_k. A_0 and A_s are constants with the values 4.04 and $\sqrt{6}\cos(\frac{1}{3}\cos^{-1}(\sqrt{6}\frac{S_{ij}S_{jk}S_{ki}}{\sqrt{S_{ij}S_{ij}}^3}))$. [30]

The definition of turbulent viscosity consists effects of mean rotation, which causes it to produce non-physical turbulent viscosities when both rotating and stationary fluid zones are present. Care must be taken when these situations exist.[30]

3.3 Interfacial Area Concentration

A multiphase flow is the flow of a mixture of phases. In the current system, three phases are present, air, water and sour gas. The sour gas is a dispersed phase that flows in the water and air, the continuous phases. The dispersed phase contains bubble particles, which have a size distribution controlled by different mechanisms: expansion due to pressure changes, breakage and coalescence. Bubble breakage occurs when turbulent eddies collide with the bubbles. The bubbles deform and stretch, and once the surface becomes unstable the bubble splits into two bubbles of equal or unequal diameter. Bubble coalescence occurs when different bubbles in the system collide. When the bubbles collide, a liquid film is trapped between the bubbles. In the coalescence process the liquid film drains until it reaches a critical thickness. At this specific thickness the film ruptures and then coalescence occurs, a larger bubble is formed.

In ANSYS Fluent the bubble particles can be tracked in the Eulerian framework by using the interfacial area concentration model.[30] Interfacial area concentration is the interfacial area between two phases per unit mixture volume. The interfacial area concentration model uses a transport equation to solve for the mass, momentum and energy transfer between two different phases. [30]

$$\frac{d(\rho_g \chi_p)}{dt} + \nabla.\left(\rho_g \bar{u}_g \chi_p\right) = \frac{1}{3}\frac{D\rho_g}{Dt}\chi_p + \frac{2}{3}\frac{\dot{m}_g}{\alpha_g}\chi_p + \rho_g(S_{RC} + S_{WE} + S_{TI}) \quad \text{Equation 40}$$

The first two terms on the right side of the transport equation account for gas expansion due to compressibility and mass transfer, respectively. The next three terms are the sink and source

terms for coalescence due to random collision induced by turbulence in the continuous phase, wake entrainment and breakage due to the collision of turbulent eddies with the bubble particles. [30]

In the interfacial area concentration transport equation ρ_g is the gas density, χ_p is the interfacial area concentration, α_g is the gas volume fraction, and $\dot{m}_g$ is the mass transfer rate into the gas phase per unit mixture volume. [30]

In ANSYS Fluent, three models are available to model bubble coalescence and breakage. The 3 models are:

- Hibiki and Ishii (2000)
- Ishii and Kim (2001)
- Yao and Morel (2004)

These models are designed to simulate interactions for bubbly flows within a pipeline. Therefore care must be taken when these models are applied to the current case of this project, as in this project the bubbly flow occurs in open waters. From literature it is found that the Hibiki and Ishii (2000) model is derived using the assumption that the bubbles are within an infinite space and there are no interactions of the bubbles with the pipeline walls. Therefore Hibiki-Ishii (2000) model is the most suitable for this project and will be used.[32]

3.3.1 Hibiki-Ishii (2000)

The model developed by Hibiki and Ishii does not contain contributions from bubble coalescence due to wake entrainment. In order to compute the bubble coalescence rate it is assumed that the bubbles act as ideal gas particles, and follow the kinetic theory of gases. The coalescence rate is given as a function of collision frequency and collision efficiency. In order to obtain an expression for the collision frequency, a constant velocity for all the bubbles is assumed and the

concept of excluded volume is introduced. This is the idea that part of the available volume in the system is excluded as bubbles not taking place in the collision are present. The following expression for bubble collision frequency is obtained:[33]

$$f_{coll} = \frac{\gamma'_c \alpha \varepsilon^{\frac{1}{3}}}{d_p^{\frac{2}{3}}(\alpha_{max} - \alpha)} \qquad \textbf{Equation 41}$$

Where γ'_c is an adjustable constant, whose value is set by authors to be 0.00261, which is based on experimental data. The limiting value for the void fraction, α_{max} is also a constant with the value 0.52.

In order to obtain the bubble coalescence rate, it is necessary to determine the coalescence efficiency. The coalescence efficiency is an exponential function of the time required for bubble coalescence given by liquid film thinning model and a contact time for two bubbles. Hibiki and Ishii used a film drainage model, which assumed that the film drained by a laminar flow with no slip at the interfaces. The formulated expression is shown below. [33]

$$\eta_c = \exp\left(-\frac{t_{contact}}{t_{drainage}}\right) = \exp\left(-K_c^{\,6}\sqrt{\frac{d_p^{\,5}\rho_f^{\,3}\varepsilon^2}{\sigma^3}}\right) \qquad \textbf{Equation 42}$$

Where K_c a coefficient with the value 1.29, which is obtained by assuming that the initial and critical film thickness, which is the point where the film ruptures, to be $10^{-4}m$ and $10^{-8}\,m$, respectively.

In order to compute the bubble breakage rate the same assumptions are made as for the coalescence rate. An expression for the eddy-bubble collision frequency is derived based on the

concept that only the turbulent eddies with a characteristic length of the order of magnitude as the bubble diameters have enough energy to break the bubbles. [33]

$$f_{b,coll} = \frac{\gamma'_b \alpha \varepsilon^{\frac{1}{3}}}{d_p^{\frac{2}{3}}(\alpha_{max} - \alpha)} \qquad \textbf{Equation 43}$$

Where γ'_b is an adjustable constant, whose value is set by authors to be 0.00367, which is based on experimental data.

The breakage efficiency is an exponential function of average energy of a single eddy and average energy required for bubble breakup.

$$\eta_b = \exp\left(-\frac{E_b}{\eta E_e}\right) = \exp\left(-K_b \frac{\sigma}{\rho_f d_p^{\frac{5}{3}} \varepsilon^{\frac{2}{3}}}\right) \qquad \textbf{Equation 44}$$

Where K_b a coefficient with the value 1.37, which is obtained by assuming that the ratio of the eddy to bubble size is 1.

Final expressions for the source and sink terms for spherical bubbles are:[33]

$$S_{RC} = -72\gamma'_c \left(\frac{\alpha}{\alpha_i}\right)^2 \frac{\alpha^2 \varepsilon^{\frac{1}{3}}}{d_p^{\frac{11}{3}}(\alpha_{max} - \alpha)} \exp\left(-K_c^6 \sqrt{\frac{d_p^5 \rho_f^3 \varepsilon^2}{\sigma^3}}\right) \qquad \textbf{Equation 45}$$

$$S_{TI} = 72\gamma'_b \left(\frac{\alpha}{\alpha_i}\right)^2 \frac{\alpha(1-\alpha) \varepsilon^{\frac{1}{3}}}{d_p^{\frac{11}{3}}(\alpha_{max} - \alpha)} \exp\left(-K_b \frac{\sigma}{\rho_f d_p^{\frac{5}{3}} \varepsilon^{\frac{2}{3}}}\right) \qquad \textbf{Equation 46}$$

3.4 Species Transport

Qatar's north gas field is one of the largest non-associated gas fields in the world, covering around 6000 square meters. The production comes from the Khuff formation. The gas obtained is sour gas with 6 % hydrogen sulfide by volume. Sour gas is natural gas with a significant amount of Hydrogen Sulfide (H_2S). Natural gas consists of several chemical species, with methane (CH_4) present in abundance. As in sour gas the crucial chemical species are H_2S and CH_4, in this project the gas released underwater will be modeled as a mixture consisting of these two species.

In this project, conservation equations will be solved for the chemical species in each phase. The general form of the conservation equation in Fluent is as follows:[30]

$$\frac{\partial}{\partial t}\left(\rho_q \alpha_q Y_{iq}\right) + \nabla.\left(\rho_q \alpha_q \vec{v}_q Y_{iq}\right) = -\nabla \cdot \alpha_q \vec{J}_{iq} + \alpha_q R_{iq} + \alpha_q S_{iq} + \sum_{p=1}^{n}\left(\dot{m}_{p^i q^j} - \dot{m}_{q^j p^i}\right) + \mathcal{R} \qquad \text{Equation 47}$$

Where Y_{iq} is the local mass fraction of species i for phase q, R_{iq} is the net rate of production of homogeneous species i by chemical reaction for phase q, S_{iq} is the rate of creation of species i by addition from external sources. In addition $\dot{m}_{p^i q^j}$ equates to the mass transfer of species i and j from phase p to phase q and $\mathcal{R}$ is the heterogeneous reaction rate. $\vec{J}_{iq}$ is the diffusion flux for species i in phase q, and takes the following form for turbulent flows:[30]

$$\vec{J}_{iq} = -\left(\rho D_{i,m} + \frac{\mu_t}{Sc_t}\right)\nabla Y_i - D_{T,i}\frac{\nabla T}{T} \qquad \text{Equation 48}$$

Where $D_{i,m}$ is the mass diffusion coefficient for species i in the mixture, μ_t is the turbulent viscosity, Sc_t is the turbulent Schmidt number with a default value of 0.7, and $D_{T,i}$ is the thermal diffusion coefficient for species i in the mixture. [30]

3.5 Mass Transfer with Multiphase Species Transport

As the released gas disperses in the water, the gas dissolves in the water and interphase mass transfer occurs. Therefore the transport of the species in the system is modelled using the following equation in Fluent:[30]

$$\frac{\partial}{\partial t}\left(\rho_q \alpha_q Y_{iq}\right) + \nabla.\left(\rho_q \alpha_q \vec{v}_q Y_{iq}\right) = -\nabla \cdot \alpha_q \vec{J}_{iq} + \alpha_q R_{iq} + \alpha_q S_{iq} + \sum_{p=1}^{n}\left(\dot{m}_{p^i q^j}\right) + \mathcal{R} \qquad \textbf{Equation 49}$$

Where the mass transfer of species i and j from phase p to phase q is given by the following formula:[30]

$$\dot{m}_{p^i q^j} = k_{pq} A_i \left(K^{\rho}{}_{p^i q^j} \rho^{j}{}_{p} - \rho^{i}{}_{p}\right) \qquad \textbf{Equation 50}$$

Where k_{pq} is the overall volumetric mass transfer coefficient between phases p and q, A_i is the interfacial area, $K^{\rho}{}_{p^i q^j}$ is the equilibrium ratio for the mass concentration, and $\rho^{j}{}_{p}$ is the mass concentration of species j in phase p. [30]

The overall volumetric mass transfer coefficient between phase p and phase q depends on the phase specific mass transfer coefficients through the following relationship:[30]

$$\frac{1}{k_{pq}} = \frac{1}{k_q} + \frac{K^{\rho}{}_{p^i q^j}}{k_p} \qquad \textbf{Equation 51}$$

The phase specific mass transfer coefficient may be defined using the Sherwood number, diffusivity and characteristic length of the phase.[30]

$$k_q = \frac{Sh_q D_q}{L_q} \qquad \textbf{Equation 52}$$

The Hughmark model is used to model the Sherwood number.[30]

$$Sh_q = \begin{cases} 2 + 0.6 Re_q{}^{\frac{1}{2}} Sc_q{}^{\frac{1}{3}} & 0 \le Re_q < 776.06 \quad 0 \le Sc_q < 250 \\ 2 + 0.27 Re_q{}^{0.62} Sc_q{}^{\frac{1}{3}} & 776.06 \le Re_q \quad 0 \le Sc_q < 250 \end{cases} \qquad \textbf{Equation 53}$$

Hughmark's model uses an exponential expression for Sherwood number, and the constants are obtained using experimental data considering mas transfer from rigid spheres.[34] It is applicable for a wide range of Reynolds and Schmidt numbers. The coefficients in the model equation can easily be altered in Fluent to model the mass transfer coefficient of gas in contaminated water opposed to clean water. Hence this model was chosen for this project. User defined functions could be added to model the mass transfer coefficient to better model the gas dissolution however at the cost of additionally computational power.

The equilibrium ratio for the mass concentration is expressed as:[30]

$$K^{\rho}{}_{p^i q^j} = \frac{c_q}{c_p} K^{X}{}_{p^i q^j} \qquad \textbf{Equation 54}$$

Where ${K^X}_{p^i q^j}$ is the mole fraction equilibrium ratio, which is calculated based on an equilibrium model. In this project Henry's law is used as it is assumes that a non-ideal mixture is present. According to Henry's law,[30]

$$ {K^X}_{p^i q^j} = \frac{P}{H^X} \qquad \textbf{Equation 55} $$

Where H^X is Henry's constant. It is a function of temperature and computed using the Van't Hoff correlation described below.[30]

$$ H^X = \left(\frac{{c_{q,e}}^i}{{X_{q,e}}^i} \right) \frac{1}{K_H} \qquad \textbf{Equation 56} $$

$$ K_H = {K_H}^0 e^{\left(-\frac{\Delta_{soln} H}{R} \left(\frac{1}{T} - \frac{1}{T_{ref}} \right) \right)} \qquad \textbf{Equation 57} $$

Where ${c_{q,e}}^i$ is the equilibrium molar concentration of species i in phase q, ${X_{q,e}}^i$ is the equilibrium molar fraction of species i in phase q. K_H is Henry's constant as a function of temperature, and ${K_H}^0$ is Henry's constant at the reference temperature, the reference T_{ref}. The temperature dependence of Henry's constant is computed using the following formula, which uses the enthalpy of solution, $\Delta_{soln} H$.[30]

$$ -\frac{d Ln K_H}{d\left(\frac{1}{T}\right)} = \frac{\Delta_{soln} H}{R} \qquad \textbf{Equation 58} $$

4 RESEARCH OBJECTIVES

In order to perform a risk assessment or develop an emergency response plan for underwater gas release, information regarding key parameters need to be obtained from the simulation results of models. The development and simulation of these models, especially CFD models is expensive and time consuming. Hence the aim of this research is to construct a nomograph using the results of a well-developed, validated CFD model. So that it is possible to evaluate assessment parameters, for example, the surface gas concentration, in a more efficient and inexpensive way.

An increasing number of sour gas reserves are being explored, especially in the Middle East. Therefore, it is more likely for hydrogen sulfide to be present in the underwater release accidents. The existing CFD models are unable to represent the behavior of the bubble plume generated from the release of sour gas underwater, as all the previous models release either air or pure methane gas. These models are not universal and include deficiencies that will impact the risk assessment. Hence the results of the previous models cannot be used to generate the nomograph. Therefore, in this project a three-dimensional, transient CFD model will be developed to model subsea releases of sour gas in shallow waters, in specific Qatar's waters (Arabian Gulf Sea). Also, the existing models mostly use the Eulerain-Lagrangian modeling concept and so require a huge amount of computational power and money to simulate, due to the large number of particles in the flow field. Hence in this project the Eulerian-Eulerian modeling concept will be used. The developed model will be able to compute assessment parameters from a given gas composition, release area, leak direction, gas flow rate, and release depth. The assessment parameters computed include, velocity and void fraction profiles for the released gas, rise time, surface gas concentrations, and gas surface flux rate. The CFD model will be developed using my colleague, Moustafa Ali's work as a basis.

The model will be validated and expanded to test a range of release depths, release flow rates and release areas.

5 METHODOLOGY

The aim of this research is to construct a nomograph that can be used to evaluate subsea gas releases in a quick and efficient manner without access to expensive and sophisticated softwares, using a data analysis approach. In order to do so a CFD model has to be developed to understand and predict the behavior of bubble plumes generated in shallow waters from the release of sour gas underwater. ANSYS Fluent version 18.2 is used for this project.

The methodology for this research project is split into different sections; experimental work selection, CFD modeling, validation of developed model, expansion of model, sensitivity analysis and nomograph development.

5.1 Experimental Work Selection

From literature it has been found that several researchers have performed experiments for an underwater gas release. An experiment will be selected to evaluate the success of the CFD model created and the reliability and accuracy of its results. In 2016, Olsen and Skjetne described the current experimental work available based on the release depth and release rates tested, which is summarized below in Table 1.[1]

Table 1: List of known experiments and their release depths and rates.

Experimental Work	Release Depth (m)	Release Rate (Nm^3/s)
Kobus (1960)[22]	4.7	0.0055
Topham (1975)[23]	23 60	0.06-0.65 0.3-0.4
Fannelop and Sjoen (1980)[27]	10	0.005-0.022
Milgram and Van Houten (1982)[35]	4	0.00021-0.0023
Milgram (1983)[5]	50	0.024-0.59
Loes and Fannelop (1989)[36]	50	0.6-1.3
Rye and Brandvik (1997)[25]	100	0.15-1.35
Engebretsen (1997)[37]	7	0.083-0.75
Johansen (2003)[38]	844	0.6 and 0.7

In order to select the experiment that will be used for the validation of the CFD model several aspects will be examined, for example the release depths, the release rates, the accuracy of the results, the type of results presented, and the number of times the experiment has already been used for validation.

5.2 CFD Modeling

The subsea gas release will be simulated using a CFD software, ANSYS version 18.2, as it solves the Naiver-Stokes equations for flow in a cost-effective manner. Three main steps will be carried out to complete the simulation; geometry design and build up, meshing of the geometry, and the model setup using Fluent. In this project a two-dimensional (2-D) model will be developed.

5.2.1 Geometry

At this stage the geometry is created using Design Modeler in ANSYS Workbench. The geometry is created to resemble the experimental setup of the selected experiment. A 2-D geometry will be created with three bodies, atmosphere body, water body, and pipeline with a hole through which the gas release will occur. The 2-D domain size will be specified. The circular cross-section of the pipeline will be sketched. The pipeline will have a diameter of 1 m and the hole diameter will be specified based on the experiment chosen for validation.

5.2.2 Meshing

After the geometry is constructed, the mesh will be generated using Design Modeler in ANSYS. In the meshing process the system is divided into cells creating a grid. Nodes are created, and the CFD code is run at each node. The accuracy of results, convergence of residuals, and computational time required for simulation depend on the number of the nodes. Therefore meshing is performed several times to obtain the optimal mesh that gives good accurate results with the shortest computational time. The optimal mesh will undergo a series of refinement to conduct a mesh independent study.

It is desired to use hexahedral elements in the mesh to minimize the overlapping elements in the system. Therefore methods will be used to minimize the presence of tetrahedral elements in the mesh.

5.2.3 Fluent Setup

The meshed geometry will then be inserted into ANSYS Fluent Setup. In the setup various parameters and models will be inputted. The multiphase, turbulence, and bubble interaction models are selected. An unsteady state, Eulerian model will be solved. The components present in the

system are air, water, methane and hydrogen sulfide gas. The turbulence model selected will be the Realizable $k-\varepsilon$ model. The boundary conditions, methods, and controls required for calculation are inputted. Once all parameters are inputted the flow will be initialized and the case simulated.

The parameters that will be changed to assess their effect on the results include the geometry design, mesh size, primary phase and turbulence model choice.

5.3 Model Validation

The developed model is validated using the selected experimental data. The model will be altered to match the input parameters to the experiment. The simulation will be run for a similar time period as stated in the experimental work. The simulation results are compared with the existing experimental data, in order to determine the accuracy of the model. The results compared include the velocity and void fraction profiles, the rise time data, the fountain heights and the pressure distribution in the system. Graphs and tables will be generated in order to present the validation results.

5.4 Expansion of Model and Sensitivity Analysis

Once the model is validated the model will be expanded. The geometry will be altered to resemble scenarios of Qatar's offshore underwater gas release. The depth of the water body will be altered to match Arabian Gulf Sea. The Arabian Gulf has minimum, average and maximum depth of 10, 50 and 100 m. A sensitivity analysis will be performed where gas released depths, release flow rates, and release hole diameters varying from small to large will be tested. Depths between 25 and 100 m will be tested. Gas flow rates between 20 and 80 kg/s will be tested.

Additional hole diameters between 0.05 and 0.25 m will be tested. The developed CFD model's geometry and meshing will be altered to simulate results for the several cases.

5.5 Nomograph Generation

The subsea gas release system will be defined and all the key variables required to describe the system will be listed; release depth, release hole diameter, gas release flow rate, gas density, rise time, surface mass flux, and surface gas concentration. Using Buckingham Pi's theorem numerous dimensionless groups will be derived. The number of dimensionless groups is equal to the number of variables minus the number of dimensions. The dimensionless groups will be grouped to form either new dimensionless numbers or already existing dimensionless numbers such as the Reynold's number.

Using the data obtained from the above mentioned cases simulated for the sensitivity analysis, results for the created dimensionless numbers, will be recorded and provided in a table. The data in the table will be used to generate a correlation matrix. The correlation matrix will be used to determine the dimensionless numbers that will represent the different axes of a nomograph. The results obtained from the developed CFD model will be plotted on the graph. The generated nomograph can then be used to know the values of variables of interest from known variables of a problem. The accuracy of the developed nomograph is limited by the precision of the results obtained from the CFD model.

6 IMPLEMENTATION OF METHODOLOGY

6.1 Selecting Experiment for Validation of CFD Model

As described above many experiments have been performed to provide information regarding subsea gas releases. The experiments are listed in Table 1.

From Table 1, it can be seen that experiments performed by Kobus, Fannelop and Sjoen, and Milgram and Van Houten are very weak in terms of release rates. Very low release rates are tested, hence these experiments will not be selected. When Topham carried out the experiment, issues were reported with the measuring equipment hence the data obtained, especially for velocities profiles, is not accurate. Therefore Tophman's experiment is also removed as a validation option. Rye and Brandivk, and Johasen performed experiments with a co-release of dyed water/oil and gas whereas in this project methane gas and sulfur gas will be released. Also they used sonar imaging to monitor the plume, no measuring equipment was in place. As the type of results required for this project are not directly provided from these two experiments they will also be discarded.[1]

Milgram's and Engebretsen's experiment both cover a good range of release depths and provide data on velocity profiles in the bubble plume. However Engebretsen's experiment has been widely used in literature to validate developed CFD and integral models. Hence Engebretsen's experiment will be used to validate the model created for this project.

6.1.1 Engebretsen's Experiment

The main objective of the experiment is to describe the interaction of the steady state plume with the ocean surface, and to predict the gas concentrations in the atmosphere.

To achieve the goal, an experiment was performed in a 7 m deep rectangular basin with a cross section of 6 m by 9 m. The basin was exposed to the atmosphere from the top. The gas released was either air or a mixture of 40 % helium and air. Air was released when parameters below the water surface were to be investigated, and the mixture was released when gas concentrations were measured. The gas was released from a piston type valve from the bottom of the basin in a vertical direction. A circular disk was located downstream of the release point to limit the vertical momentum of the initial jet. The disk was enclosed in a tube to direct the horizontal motion of the gas to the vertical direction. A constant gas flow rate was maintained throughout the experiment, by keeping the pressure constant through the use of a pressure regulator. Three different flow rates were tested: 0.083 Nm^3/s (0.05 m^3/s), 0.17 Nm^3/s (0.1 m^3/s) and 0.75 Nm^3/s (0.45 m^3/s).

Video cameras were placed at different locations to obtain information regarding the bubble shapes, sizes, and overall plume behavior. Measuring equipment were placed at several vertical and horizontal positions to measure the velocity, void fraction profiles, and gas concentration above the ocean surface.[37]

6.2 Design of CFD Model for the Simulation of Underwater Sour Gas Release

6.2.1 Creating the Geometry

A 2-D geometry was created using Design Modeler in ANSYS Workbench (Figure 7). First, a rectangle was sketched on the XY plane. Dimensions of the rectangle were set; 12 m in the y-direction and 6 m in the x-direction. Next the rectangle was split at a height of 9 m to create two different bodies. The upper rectangle represents the 2-D atmosphere body with dimensions 3 m by 6 m. The lower rectangle represents the 2-D water body with dimensions 9 m by 6 m. Third; a

circle was sketched on the XY plane with a diameter of 1 m. The position of the center of the circle was set: 3 m in the positive x-direction and 1.5 m in the positive y-direction. The circle was placed 1 m from the bottom of the water body. The position of the pipeline in the water body was chosen in order to obtain convergence of results and may be altered throughout the project. Then using the Split option, two points on top of the circle were selected to split the circle into 2 sections, the pipeline inlet and wall. The size of the pipeline inlet was set to 0.17 m. The surfaces of the water and atmosphere body were selected and using the Modeling tab surfaces from sketches was generated. The pipeline circle was then a hollow circle in the water body.

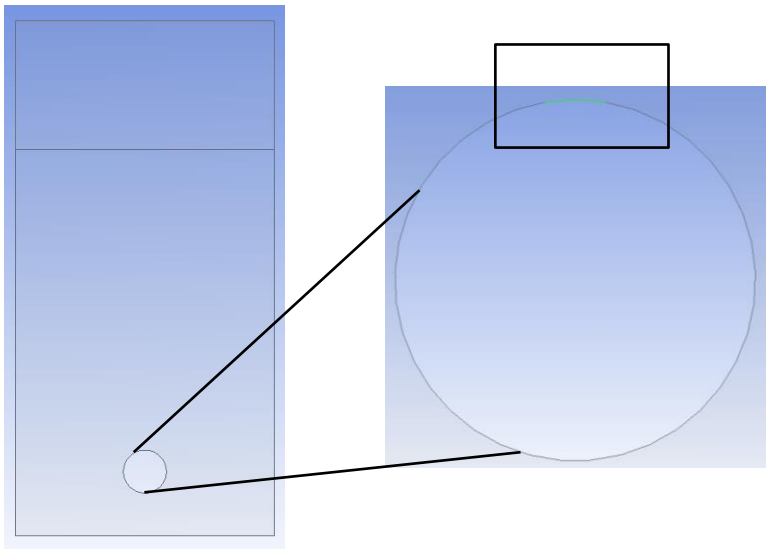

Figure 7: 2-D geometry designed in ANSYS Workbench, based on Engebretsen's experimental setup.

6.2.2 Meshing the Geometry

In the meshing process, first the surfaces and bodies are named. The named selections are:

- Atmosphere body, which is the upper body in the geometry.
- Water body, which is the lower body in the geometry.
- Pipe wall, which is the edge of the pipeline.
- Inlet, which is the opening on the pipe wall.
- Water boundary, which are edges, the sides of the water body.
- Atmosphere boundary, which are edges, the sides of the atmosphere body.
- Water bottom, which is the edge at the bottom of the water body.
- Atmosphere top, which is the edge at the top of the atmosphere body.
- Surface, which is the edge that separates the atmosphere and water bodies.

Once the selected regions are named the process of mesh generation begins. Suitable sets of global mesh controls were assigned. The dialog box for global mesh controls appears when mesh is selected in the tree outline. In the default group CFD was chosen for the physical preference and Fluent chosen for the solver preference. Next in the sizing group the relevance center was set to fine and the relevance was set to 100 in order to obtain a high quality mesh.

In order to generate a mesh that is finer in the areas where the bubble plume will be, the water body is split into many parts, to generate edges and surfaces to which edge sizing, face sizing and face meshing can be applied (Figure 8). The element size was set to 2 cm in the bubble plume region in the water body, and 4 cm for the remaining sections of the water body. Next, edge sizing was inserted on the pipeline inlet section of the circle, with an element size of 1 mm. The behavior of all the edge sizing applied were set to hard. Next edge sizing and face meshing were applied to the edges and surfaces of the atmosphere body. The mesh was generated, by generating it on each body separately. The mesh generated consists of 86,774 cells and 87,400 nodes. The average skewness of the mesh is 0.027 and the average orthogonal quality is 0.99.

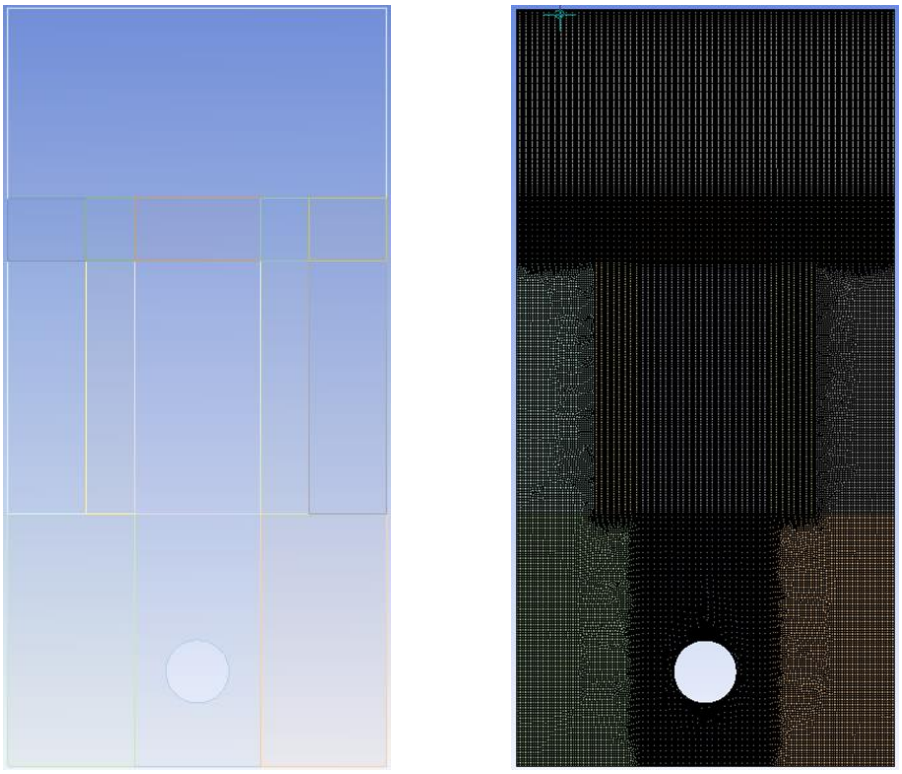

Figure 8: An image of the geometry used for generating a mesh finer in the bubble plume region (on the left) and the generated mesh (on the right).

6.2.3 Fluent Setup

6.2.3.1 General Settings

In this section the general settings required are selected, for example the solver type is chosen to be pressure based, the velocity formulation is chosen as absolute and a 2-D problem is to be calculated. It is desired to obtain results regarding the release of gas overtime; therefore the time is set as transient. The gravity direction and value is specified to be y direction and -9.81 m/s^2, respectively.

6.2.3.2 Materials Addition

The materials will be added, which include the fluids and solids; methane gas, H_2S gas, air and water. In order to test for sour gas release, mixture materials are required. The SPECIES TRANSPORT MODEL will be activated to generate mixture materials. Two mixture materials will be created. The gas released will be a mixture of H_2S and methane gas (Mixture 1). The second mixture material will consist of three fluid species, methane, H_2S and liquid water (Mixture 2). The third material will not be a mixture, it will contain air only. Properties for the mixtures created are required. In the mixture materials dialog box the mass diffusivity is set as multicomponent and is specified for each pair of species. The values inputted are shown in Table 2 below.

Table 2: Mass diffusivity values used for each pair of species.

Mass Diffusivity at 25 °C and Atmospheric Pressure (cm^2/s)		
Methane/hydrogen sulfide[39]	Methane/Water[39]	Hydrogen sulfide/Water[39]
1e-30	1.84e-05	1.36e-05

6.2.3.3 Multiphase Model Selection

The current case of a bubble plume is categorized as a multiphase flow; which is the flow of a mixture of more than one phase. The released gas is referred to as the dispersed phase, whereas the air and water are the continuous phases. Hence a multiphase model will be used for the development of the CFD model. The Eulerian model will be selected, as it is recommended for applications such as bubbly flows and it can be used to track the bubbles in the system.

Three phases will be specified. Mixture 2, the material consisting of water will be set as the primary phase, and Mixture 1 and air will be set as the two secondary phases in the system. Mixture 1 is a dispersed phase which consists of bubbles, which have a size distribution controlled by different mechanisms, including bubble breakage and coalescence. In the model an additional transport equation will be solved for the interfacial area concentration in order to account for the bubble size distribution due to different mechanisms. In the secondary phase dialog box for Mixture 1 (methane and H_2S), interfacial area concentration box will be ticked. The diameter will be set as sauter-mean, the surface tension will be set as 0.072 N/m, and the minimum and maximum bubble diameters will be 0.00001 and 0.01, respectively. The model chosen to model the breakage and coalescence mechanisms is Hibiki-Ishii (2000). A model is also selected of the dispersion rate, fluent-ke. Hibiki-Ishii model is the most suitable model for gas release in open waters.

6.2.3.4 Phase Interactions: Mass Transfer Addition

Mass transfer mechanisms will be added to account for the gas dissolution of methane and H_2S gas in water phase. In the phase interactions dialog box, mass transfer mechanism chosen for the transfer of species methane and H_2S is the species mass transfer. The mass transfer coefficient from the gas phase to the water phase will be modelled using Hughmark's equation. Henry's law will be used to obtain the solubility data. It is assumed that Henry's constant is a function of temperature which is given by Van't Hoff correlation. The input parameters for Van't Hoff correlation for each of the species is shown in Table 3 below.

Table 3: Van't Hoff correlation parameters used in simulations.

Species	K_H (M/atm)	$\frac{dLnH_{cp}}{d\left(\frac{1}{T}\right)}$ (K)
Methane (CH_4)[40]	1.4186e-03	1900
Hydrogen Sulfide (H_2S)[41]	0.10133	2100

6.2.3.5 Viscous Model Selection

Turbulent flow is an irregular, chaotic flow of fluid. Eddies can be visualized, which are the swirling motion of the fluid. In turbulent flow the velocity and pressure changes continuously with time. Turbulence will be modeled in this project using realizable $k-\varepsilon$ model. Reasons for why this particular turbulence model is selected is provided in the model configuration section of thesis. The model constants are set as default. Scalable wall functions are selected for near-wall treatment. The turbulent multiphase model is solved for each phase separately.

6.2.3.6 Boundary Conditions

The boundary conditions are defined in order to solve the equations in Fluent. Boundary conditions are associated with the different selections of the geometry. The type of boundary conditions, and other required information for the selections are listed below.

- For the pipeline wall, and water bottom the type of boundary condition is 'wall'.
- For the atmosphere top and boundaries of the atmosphere body the type of boundary condition is 'pressure outlet', the outlet is the atmosphere hence the gauge pressure for this condition is set to zero.

- For the water body boundaries the type of boundary condition is ‘pressure outlet’, the pressure is specified by the addition of a User-Defined-Function (UDF). The text file for the UDF is shown in Figure 9

```
/**************************************************

boundary condition for pressure outlet on water boundary

**************************************************/

#include "udf.h"

DEFINE_PROFILE(pressure_profile,t,i)
{

real x[ND_ND];
real y;
face_t f;
begin_f_loop(f,t)
{
F_CENTROID(x,f,t);
y = x[1];
F_PROFILE(f,t,i) = 998.2*9.81*(9-y);
}

end_f_loop(f,t)
}
```

Figure 9: UDF for pressure distribution for the boundaries of the water body.

- For the inlet, the type of boundary condition is ‘mass flow inlet’. The direction of the flow is set as normal to the boundary. The flow rates for the phases with air and water are set to zero and the flow rate for the released gas phase is changed over the course of the project. The amount of H_2S species in this gas phase is set to 6 volume percent, which is equivalent to 11% by mass. This gas composition has been obtained from one of the sour gas reservoirs in Qatar.

6.2.3.7 Methods

In this section the methods used to calculate the solution will be selected. The scheme used for the pressure velocity coupling is Phase Coupled SIMPLE. The spatial discretization for the gradient will be derived used the Least Square Cell Based method. The spatial discretization for the momentum, volume fraction, energy, turbulent kinetic energy and dissipation rate are derived from the Second Order Upwind schemes. The transient formulation is solved using the First Order Implicit scheme. The schemes used may be changed throughout the process to improve accuracy of results and to decrease computational time.

The under relaxation factors for the solution controls for the pressure, density, body forces, momentum, volume fraction, energy, turbulent kinetic energy, dissipation rate and viscosity may also be varied throughout the process to achieve convergence of results.

6.2.3.8 Initialization and Patching

The simulations run for this project are all transient and so initial conditions are required and are automatically set by ANSYS Fluent based on the inputs made in previous sections. Once the model is initialized, various parameters are patched. Patching is the process of specifying initial conditions to some regions of the meshed geometry. Patching is performed to specify the volume fraction of the secondary phases in the different cell zones, the atmosphere and water bodies. The volume fraction of air phase in the atmosphere body is set to 1 and in the water body is set to 0. Similarly, the volume fraction of Mixture 1(dispersed gas phase) is set to 0 in both the atmosphere and water bodies. The mass fraction of the species in the primary and secondary phases will also be patched. The mass fractions of methane and H_2S are 0 in both the atmosphere and water bodies, for all the phases.

6.2.3.9 Run Calculation

Next the information regarding the time step size, number of time steps, and number of iterations per time step will be specified. The time step size is not specified as a fixed value, an adaptive time stepping method is chosen. This method allows for the time step to be computed automatically based on the estimation of the truncation error associated with the time integration scheme. In the adaptive time setting dialog box the truncation error tolerance is set to 0.01, the ending time is set to 200 s and the minimum and maximum time step sizes are set as 0.001 and 0.01, respectively. The number of time steps will be altered with different runs, ranging in between 5000 and 30000. Similarly the number of iterations per time step will also be varied for each run, the value ranges between 100 and 5000.

Next, the generated Fluent file will be exported as a case file and uploaded on Supercomputer RAAD 2 at Texas A&M University at Qatar, to increase the computational power in order to reduce the computational time. Job and journal files will be created that are shown below in Figure 10 and Figure 11, respectively. The job files are submitted on the supercomputer. Multiple files are submitted simultaneously, and the result files are obtained. For each scenario first a case file without any gas release is submitted to evaluate the pressure distribution in the water body. The result of this case is then read to simulate the results of the case file with gas release.

```
#!/bin/bash
#SBATCH -J Case_035_v1
#SBATCH -p 1_long
#SBATCH --qos 11
#SBATCH --time=168:00:00
#SBATCH -N 2
#SBATCH --ntasks-per-node=24
##SBATCH --ntasks=16
#SBATCH --output=e_ansys_sim.%j
#SBATCH --error=o_ansys_sim.%j
#SBATCH --hint=nomultithread
##SBATCH --mail-type=ALL
#SBATCH --mail-user=wafa.imran@qatar.tamu.edu
#SBATCH --gres=craynetwork:0

## Get job Stats
echo "Starting at "`date`
echo "SLURM_JOBID="$SLURM_JOBID
echo "SLURM_JOB_NODELIST"=$SLURM_JOB_NODELIST
echo "SLURM_NNODES"=$SLURM_NNODES
echo "SLURMTMPDIR="$SLURMTMPDIR
echo "working directory = "$SLURM_SUBMIT_DIR


# Load Ansys Module
module use /lustre/sw/xc40ac/modulefiles
module load ansys/182

# Load Intel Compiler if needed for simulation
# module swap PrgEnv-cray/5.2.82 PrgEnv-intel


# Start Simulation
echo "Starting Simulation.."

fluent 3ddp -g -t24 -i journal.jou >f_Case_035_v1.out


echo "Ending at "`date`
echo "Simulation Ended"

```

Figure 10: Sample job file.

```
/file/read-case /lustre/projects/MKOPSCQ/2019.SubSurface.Wafa/Case_014/Case_014_v1.cas
;/rc c:\Users\k.kakosimos\!DATA\FluentDDPM\Trial_v2_files\dp0\FLU-2\Fluent\SYS.2-Setup-Output.cas.gz
/solve/initialize/initialize-flow
/solve/patch p-water airbody () mp 0
/solve/patch p-water waterbody () mp 1
/solve/patch p-methane airbody () mp 0
/solve/patch p-methane waterbody () mp 0
solve/dual-time-iterate 20 5000
/file/write-data Case_014_v1
exit
yes

```

```
/file/read-case /lustre/projects/MKOPSCQ/2019.SubSurface.Wafa/Case_035/v1/Case_035_v1.cas
;/rc c:\Users\k.kakosimos\!DATA\FluentDDPM\Trial_v2_files\dp0\FLU-2\Fluent\SYS.2-Setup-Output.cas.gz
/file/read-data Case_014_v1.dat
solve/dual-time-iterate 5000 5000
/file/write-data Case_035_v1
exit
yes

```

Figure 11: Sample journal files.

7 MODEL CONFIGURATION

In order to construct a CFD model with the best performance and results a few parameters were investigated. The parameters that were investigated are: the geometry design, mesh size, primary phase selection, and $k-\varepsilon$ turbulence model selection. The CFD model described in the above section, is the final model with the best performance.

7.1 Geometry Design Selection

In Engebretsen's experiment, a circular disk is placed within a tube above the release point. To fully replicate the experimental design, the geometry shown in Figure 7 is edited to include these additional components. A rectangle with length 40 cm and height 1 cm is sketched 25 cm above the release point, it represents the circular disk. A tube with thickness 1 cm is sketched around the circular disk. The new geometry design in the release point region is shown in Figure 12.

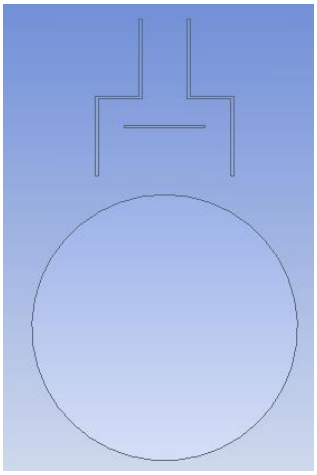

Figure 12: Geometry with circular disk and tube.

The fluent setup described above is simplified to release air underwater, as given in the experimental work. A transient, 2-D, Eulerian model with 2 phases is solved. No mass transfer effects are added. The turbulence model used is realizable $k-\varepsilon$ model. Air is selected as the primary phase and a constant bubble diameter is used. The mass flow inlet for the air phase is set as 0.12 kg/s, which is equivalent to a volumetric flow rate of 0.1 m^3/s (one of the flowrates tested in the experimental work). The results obtained from the simulation using geometry design 1 (shown in Figure 7) and geometry design 2 (shown in Figure 12) are compared to one another and to the experimental results. The results are shown in the figure below (Figure 13).

In Figure 13 (a) the results for the centerline velocity are shown. It is observed that the centerline velocities obtained for the simulation using geometry 1 are a little smaller than the experimental data, but follow the same trend. The centerline velocity decreases with increasing vertical distance from release point. For geometry design 2, at a vertical distance of 3.8 m from the release point, the centerline velocity is a lot greater than the experimental result. Due to this result the basic trend of the experimental data is not followed. The average percentage error between the simulation and experimental data for geometry design 2 is 6 % whereas between geometry design 1 and experiment is 5 %. Therefore, the centerline velocity results favor the use of geometry design 1.

In Figure 13 (b) the results for the centerline volume fraction are shown. The results obtained with geometry 1 show that the volume fractions are greater than the experimental observations. Whereas for geometry 2, the volume fraction simulation results are lower than the experimental data. For both geometry designs the trend of experiment data is followed, as the vertical distance from release point increases the volume fraction decreases. The average percentage error between geometry 1 and experimental results is 33 %, and between geometry 2

and experimental data is 28 %. As the average percentage error for geometry 2 volume fraction results is smaller, geometry design 2 is favored.

In Figure 13 (c) the rise time results are displayed. It can be seen from the bar chart that the rise time obtained using geometry 1 is closer to the experimental rise time compared to geometry 2 rise time result. The percentage error between geometry 1 and geometry 2 with the experimental results are 23 % and 48 %, respectively. Therefore, the rise time result favors the use of geometry 1.

Overall, the simulation results from geometry design 1 are closer to the experimental results. In addition, in the experimental work no information about the position and size of the circular disk and tube are provided, suggesting that adjustments to the size and position could be made during geometry design to obtain better results. This is not desirable as the results would be over fitted, making the model unreliable for future cases. Hence geometry 1 is selected to be used for the CFD model in this project.

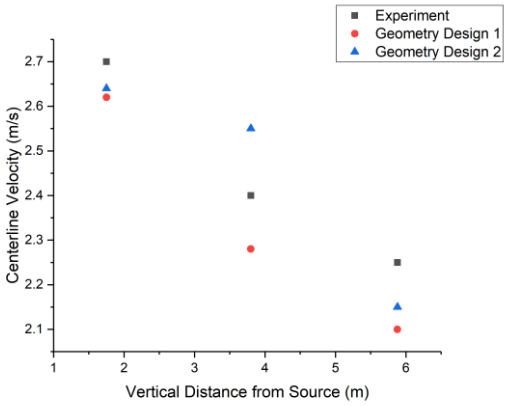

(a)Centerline Velocity

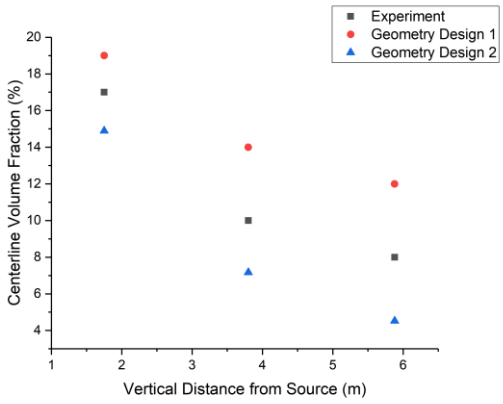

(b)Centerline Volume Fraction

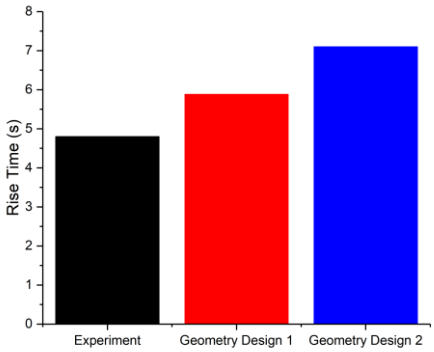

(c)Rise Time

Figure 13: Comparison of centerline velocity, volume fraction and rise time results for simulations with different geometry design and experiment.

7.2 Mesh Independence Study

The results obtained from simulations of models with different meshes differ as the meshes have different resolutions. Hence a mesh independence study is carried out to obtain a solution that is independent of the mesh resolution. Three different meshes were designed and are shown below in Figure 14.

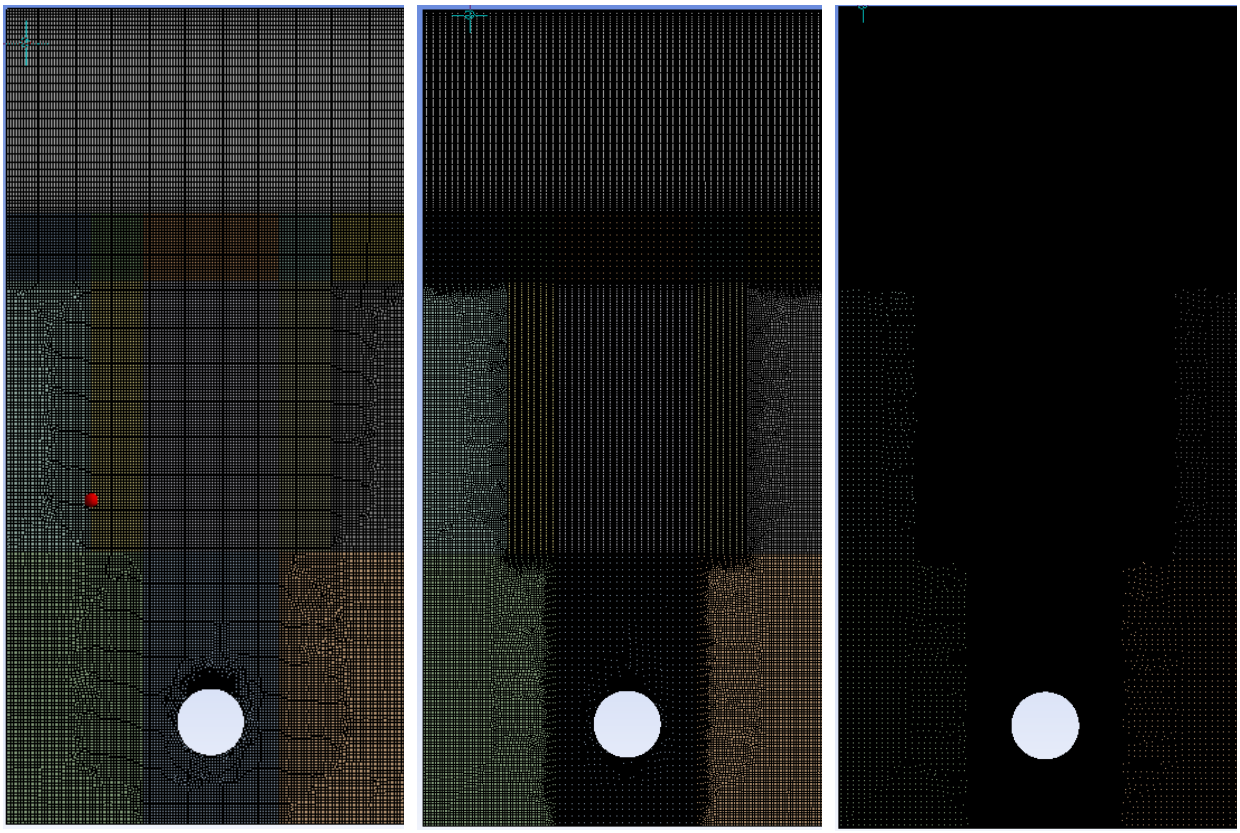

(a)Mesh A (b)Mesh B (c)Mesh C

Figure 14: Meshes generated with different resolutions to be used for mesh independent study. The meshes differ in the cell sizes in the domain.

The meshes shown in Figure 14 are all meshed in a similar manner. The mesh is finer at the release point and the regions where the bubble plume is most likely to be found. The cell size at and near the release point is set to 1 mm. For Mesh A the cell size in the bubble plume region is 4 cm and outside this region is 6 cm. Mesh B is a refinement of Mesh A, where the cell size is 2 cm in the bubble plume region and 4 cm outside this region. Similarly, Mesh C is a refinement of Mesh B. The cell sizes are 1 cm and 3 cm in the bubble plume region and outside, respectively. As the mesh was refined from Mesh A to Mesh B, there was a change in the rise time results,

which is the time taken for the bubble plume to reach the surface, the centerline velocity and volume fraction results (Table 4). The rise time changed from 9.5 s to 8 s. The centerline velocity and volume fractions at different vertical distances from the release point increased significantly. However when the mesh was refined from Mesh B to Mesh C, the rise time, centerline velocity and volume fraction results obtained from simulating the model did not vary significantly. Therefore no further refinement steps were required after Mesh C.

In order to determine which mesh to use the simulation residuals and simulation times were monitored, the information is presented below in Table 4.

Table 4: Mesh independence study results.

Mesh		Mesh A	Mesh B	Mesh C
Number of Cells		59,974	86,774	384,788
Continuity Residual		~ 10-3	~ 10-4	~ 10-4
Air Volume Fraction Residual		~ 10-5	~ 10-6	~ 10-4
Simulation Time to Reach 5 s (mins)		8	12	48
Rise Time (s)		~ 9.5	~ 8	~ 8
Centerline Velocity at Different Vertical Distances from Release Point (m/s)	1.75 m	~ 2.3	~ 2.7	~2.7
	3.8 m	~ 1.4	~ 2.3	~ 2.3
	5.88 m	~ 1.3	~ 2.0	~2.2
Centerline Volume Fraction at Different Vertical Distances from Release Point (%)	1.75 m	~ 13.3	~ 16.5	~ 16.9
	3.8 m	~ 10.4	~ 9.5	~ 9.6
	5.88 m	~ 9.9	~ 8.2	~8.2

Residuals are used as an indication of convergence. A residual error of 10^{-4} is considered acceptable. From Table 4 it is found that Mesh A has continuity residual greater than 10^{-4}, and also the mesh does not provide an independent result, therefore Mesh A is discarded. From Table 4 it can be seen that Mesh B and Mesh C have residuals for continuity and air volume fraction that are above or equal to 10^{-4}. Therefore these two meshes are further analyzed. Simulating the CFD model with Mesh B leads to the same results as when Mesh C is used, however with a much shorter simulation time. Therefore Mesh B is used for the development of the final CFD model.

7.3 Primary Phase Selection

In the fluent setup, when a multiphase model is selected, the number of phases are specified. Each phase is categorized as either the primary phase or secondary phase. Simulating the case for validation, air and water are the existing phases. It is recommended by Fluent to use compressible ideal gas phase as the primary phase if present to avoid stability problems. However it is also appropriate to use the continuous phase as the primary phase, as this is the bulk phase. Hence, in order to determine which material to set as the primary phase, two cases were simulated. In the first case air was the primary phase and in the second water was the primary phase. The results obtained were compared with experimental data and are shown in Figure 15. For these simulations no mass transfer effects were added, the turbulence model used is realizable $k-\varepsilon$, and a constant bubble diameter is used. The mass flow inlet for the air phase is set as 0.12 kg/s.

Figure 15 (a) shows the centerline velocity results. In general the simulation centerline velocities are only slightly smaller than the experiment values and follow the same trend. The centerline velocity decreases as the vertical distance from the release point increases. From Figure 15 (a) it can be seen that when water is selected as the primary phases the simulation centerline velocity results are closer to the experimental data for vertical distances 1.75 and 3.8 m. However

for vertical distance of 5.88 m the simulation results are closer to the experimental results when air is chosen as the primary phase. The average percentage error between the simulation and experimental results for primary phase air and water are 4.9 and 10.2 %, respectively. Figure 15 (b) shows that when water is selected as the primary phase the simulation volume fraction results compare better with the experiment then when air is chosen as the primary phase. However, Figure 15 (c) conveys that when air is the primary phases the simulation rise time of the dispersed gas is closer to the experimental rise time.

The overall error between all the simulation and experimental results for when the primary phase is air and water are 20.4 and 26 %, respectively. There is only a slight difference in the error. Additionally, for the final model setup a bubble size distribution is to be provided by means of activating the interfacial area concentration model and solving for the transport equation of interfacial area concentration. This only works well if the dispersed gas phase is selected as the secondary phase, and the continuous phase is selected as the primary phase. Therefore water is used as the primary phase in this project.

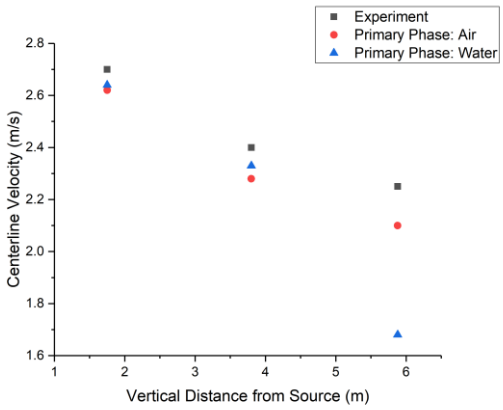

(a)Centerline Velocity

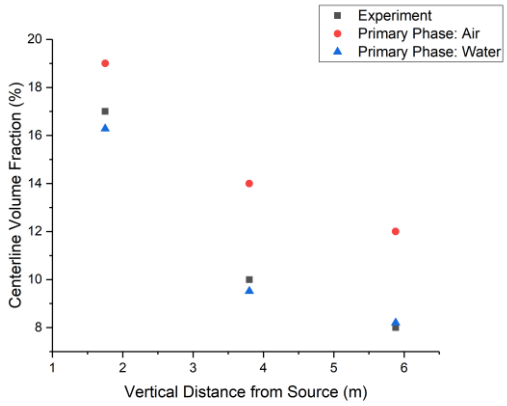

(b)Centerline Volume Fraction

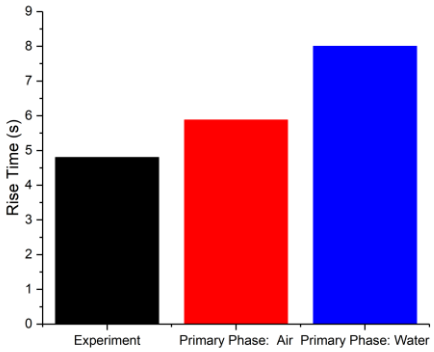

(c)Rise Time

Figure 15: Comparison of centerline velocity, volume fraction and rise time for simulations with different primary phases and experiment.

7.4 Turbulence Model Selection

There are several turbulence models available in Fluent. In 2017 Wu et al. tested turbulence models other than the 2-equation k-epsilon equations. It was concluded from the results that LES model produces the most accurate results when compared to experimental data. However LES model is not available with the Eulerian multiphase model and it is recommended only for meshes with approximately billion cells. Therefore, in this project, the 2-equation k-epsilon turbulence

models are used. There are three $k-\varepsilon$ models: Standard, RNG, and Realizable. The case where 0.12 kg/s of air is released underwater is simulated with all three turbulence models with air as the primary phase, and the results compared to experimental data. The comparison of results is shown below in Figure 16.

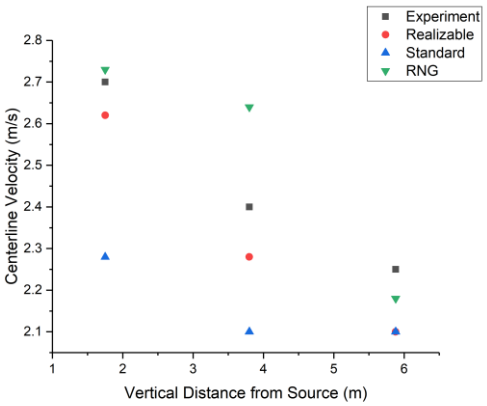

(a)Centerline Velocity

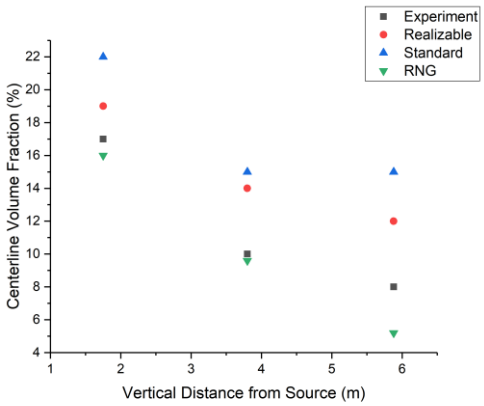

(b)Centerline Volume Fraction

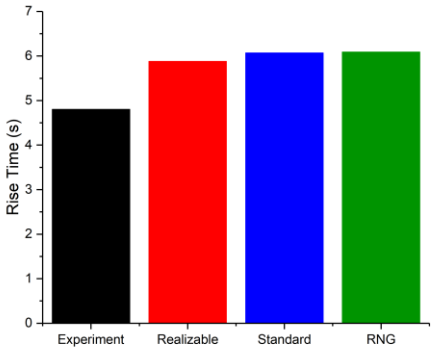

(c)Rise Time

Figure 16: Comparison of centerline velocity, volume fraction and rise time results for simulations with different turbulence models and experiment.

From Figure 16 it can be seen that the centerline velocity, volume fraction and rise time results for the case when the standard $k-\varepsilon$ model is used are the furthest away from the experimental results. So the standard $k-\varepsilon$ model will not be used in this project.

The results for the remaining two models are compared with experiment. The average percentage error between RNG centerline velocities and experimental values is 5 %. Also, the average percentage error for the realizable model centerline velocities is 5 %. The percentage errors are very similar, however the realizable model displays centerline velocity results with a similar trend as the experiment. As the vertical distance from the release point increases the centerline velocity decreases. Therefore Figure 16 (a) suggests that realizable $k-\varepsilon$ model is more suitable for this project.

The results for centerline volume fraction, displayed in Figure 16 (b), suggest otherwise. The average percentage errors between simulation volume fraction results and experimental volume fraction results for RNG and realizable models are 15 % and 34 %, respectively. The volume fraction results favor the RNG $k-\varepsilon$ model.

In addition, Figure 16 (c) shows that the different turbulence models generate similar rise time results When the realizable $k-\varepsilon$ turbulence model is used the rise time obtained agrees better with the experimental rise time compared to when RNG $k-\varepsilon$ model is used. The percentage errors between RNG and realizable rise times with experimental rise time result are 26.8 % and 22.5 %, respectively.

The results in Figure 16 suggest that realizable $k-\varepsilon$ model is best fit for this project. In addition, evaluating the transport equations of kinetic energy and dissipation rate for the realizable model, it is found that the realizable $k-\varepsilon$ model uses a different formulation compared to RNG

$k-\varepsilon$ models for the turbulence viscosity constant and transport equation for the dissipation rate. This makes it superior to the other $k-\varepsilon$ models as it gives improved predications for the spreading rate of jets, and it has the ability to better capture flows involving boundary layers under strong pressure gradients, rotation, separation and recirculation. Therefore realizable $k-\varepsilon$ model is used for this project.

8 VALIDATION OF CFD MODEL

In order to check the performance of the developed CFD model the results obtained from the model simulation have to be validated against experimental data. As mentioned previously, Engebretsen's (1997) experiment will be used for the validation. In this experiment air is released in a water tank with dimensions 6 m, 9 m, and 7 m in the X, Y and Z directions, respectively. The air is released from a nozzle, with a release diameter of 0.17 m. The release point is located at a 7 m depth. Three release rates are tested, which are shown below in Table 5.

Table 5: Release rates of gas used in the experimental work.

Volumetric Release Flow Rate (Nm^3/s)	Volumetric Release Flow Rate (m^3/s)
0.083	0.05
0.17	0.1
0.75	0.45

Some adjustments are required to the model setup, described above in section 6.2.3, to match the conditions of the experiment. A transient, Eulerian model is still being solved. The experiment releases air not sour gas, therefore only two phases are required, air and water. Mixture materials are not required, so the species model is not activated and fluids air and water are added for the materials. The water phase is selected as the primary phase. No mass transfer effects are added for the phase interactions, the remaining phase interactions, such as drag are set as default. All of the boundary conditions are the same except for the mass flow inlet, and pressure outlet for the sides of the water body. A mass flow rate is specified for the air phase. The mass flow rates

inputted into the system are shown below in Table 6. The boundary condition for the sides of the water body is set as walls, as the experiment is carried out in a basin. The remaining setup parameters are consistent with the above mentioned setup, so are not described here.

Table 6: Mass flow rate of air inputted in the model for the boundary condition.

Volumetric Release Flow Rate (m^3/s)	Release Mass Flow Rate (kg/s)
0.05	0.06
0.1	0.12
0.45	0.55

The developed CFD model was run for the three different release rates. Figure 17 shows the contour maps for the air volume fraction approximately 9 seconds after release. From Figure 17 it can be seen that as the release rate increases the gas rises faster. From the Figure it can also be deduced that the plume width at any given vertical distance is greater for a greater release rate.

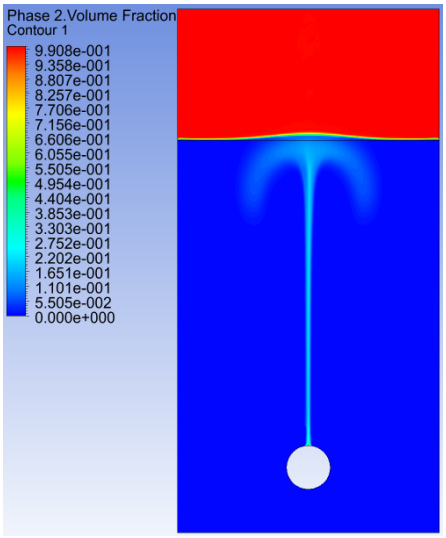

(a)Release Rate 0.05 m^3/s

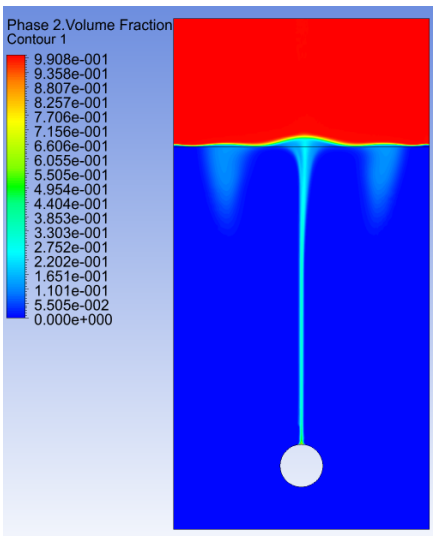

(b)Release Rate 0.1 m^3/s

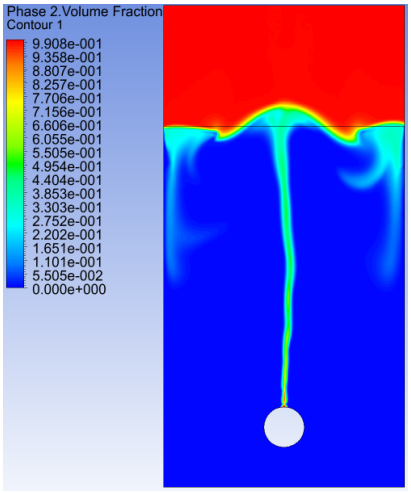

(c)Release Rate 0.45 m^3/s

Figure 17: Air volume fraction contours after 8 seconds of release for different release rates.

In the experimental work the results presented are; centerline velocities and void fractions at different vertical distances from the release point, the time taken for the first gas bubble to reach the surface (rise time), and the maximum fountain height generated. The centerline velocities and void fractions were measured at three different vertical distances from the release point for release

flow rates of 0.05 and 0.1 m^3/s. The vertical distances are 1.75, 3.8 and 5.88 m from the release point. For the third case, with release rate of 0.45 m^3/s the results were only recorded at a vertical distance of 5.88 m from the release point.

The results for the mentioned variables were obtained from the CFD model simulation, they were then analyzed and compared with the experimental values. For each case, results for the velocity and volume fraction were obtained for several points along the x-axis at different vertical distances (as shown in Figure 18) for all the time steps, up to at least 20 seconds. A matrix was created with time series of velocity and volume fraction results at different x positions at different vertical distances. The maximum velocity, and average volume fraction was extracted from the time series and the mean and standard deviation was calculated. The mean values were compared to the experimental values. The results obtained are described below.

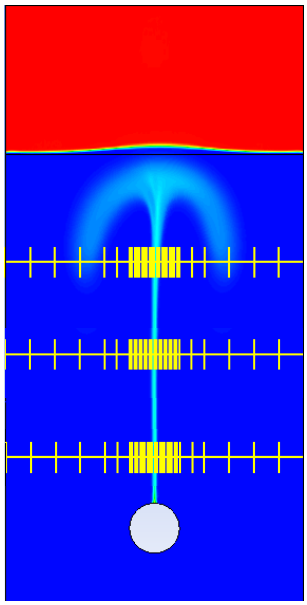

Figure 18: Diagram showing points at which velocity and volume fraction results were taken to perform analysis of CFD results.

Figure 19 shows a graph of vertical distance from release point against centerline velocity for the CFD simulation and experiment for different volumetric flow rates of release. The Figure suggests that for a given release rate the centerline velocity decreases as the vertical distance from the release point increases. This is due to the fact that as the gas rises, the gas expands due to the pressure distribution underwater resulting in a decrease in the velocity.

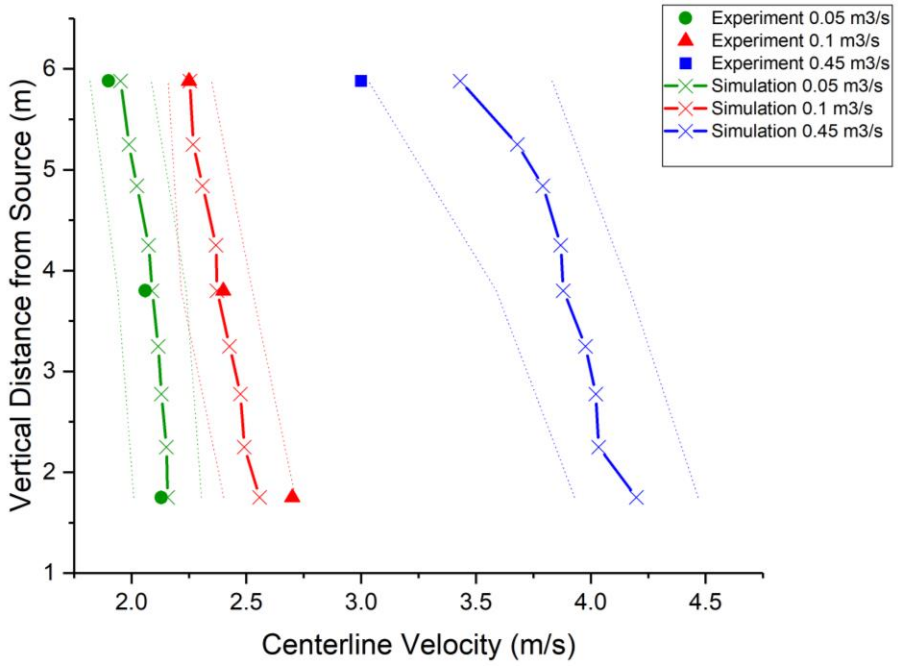

Figure 19: Comparison of simulation and experimental results for centerline velocity.

From Figure 19, it can be comprehended that for release rates of 0.05, 0.1 and 0.45 m^3/s the centerline velocities from the simulation are slightly higher than experimental observations. It is found that for release rate of 0.05 m^3/s the difference between the simulation and experiment centerline velocities increases with an increase of the vertical distance from the release point. The

percentage errors between the simulation and experiment for release of 0.05 m^3/s are 1.3, 1.5 and 2.8 % for vertical distances 1.75, 3.8 and 5.88 m, respectively. In contrast, for release rate of 0.1 m^3/s the difference in velocities between simulation and experimental values decreases with increasing vertical distance. The percentage errors are 5.3, 1.2, and 0.20 % for distances 1.75, 3.8 and 5.88 m, respectively. The percentage error between the simulation and experimental result of release rate of 0.45 m^3/s at a vertical distance of 5.88 m from the release point is 14 %. On average, the percentage error between the simulation and experimental values increases with increasing volumetric flow rate. On a whole, the simulations are consistent with the experimental data. The percentage errors between the results are minimal, and therefore can be accepted. The dotted lines on the Figure represent the error ranges of the simulation results, they indicate the deviations that exist in the simulation data. All the experimental points lie within the error ranges of the simulation results, suggesting that the results are reliable.

Next, Figure 20 displays a graph of vertical distance from release point against centerline volume fraction for simulation and experimental results. It is found from the Figure that the centerline volume fraction decreases as you move further away from the release point.

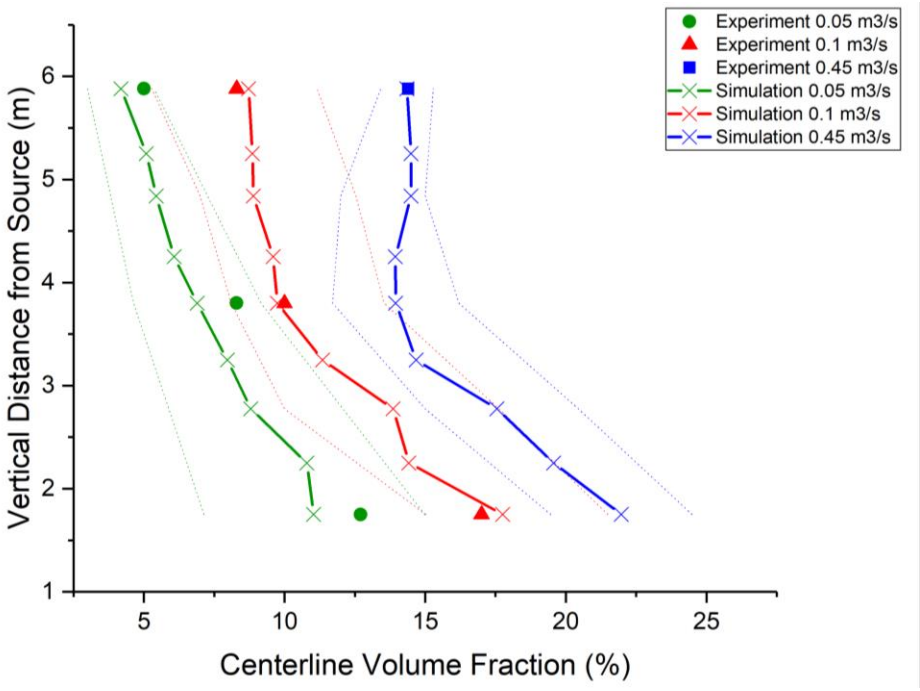

Figure 20: Comparison of simulation and experimental results for centerline volume fraction results.

From Figure 20 it is found that the simulation slightly under predicts the centerline volume fraction for release rate of 0.05 m^3/s, and slightly over predicts the results for 0.1 m^3/s. For release rate of 0.45 m^3/s the simulation value given at vertical distance 5.88 m is nearly equivalent to the experimental result. From the Figure it is also observed that for release rates of 0.05 and 0.1 m^3/s, in general the difference between the simulation and experimental centerline volume fraction decreases with increasing vertical distance from the release point. The percentage error between the simulation and experimental observations for release rate of 0.05 m^3/s are 13, 16 and 16 % at vertical distances 1.75, 3.8 and 5.88 m, respectively. Similarly, the errors for release rate of 0.1 m^3/s are 4.5, 2.5 and 5.1 % at distances 1.75, 3.8 and 5.88 m, respectively. For release rate of 0.45 m^3/s the percentage error between the simulation and experiment volume fraction is 0.33 % at distance of 5.88 m.

From the Figure it can be observed that the error range found from 0.1 m^3/s simulation results is much larger compared to the error range for 0.05 and 0.45 m^3/s results. This suggests that there is a larger deviation is the volume fraction results obtained for 0.1 m3/s release rate. In general the experimental data points lie within the standard errors for all simulations hence the simulation results are reliable. Overall, the average percentage error for the centerline volume fraction is 8.4 %, which is acceptable.

Furthermore, from Figure 19 and Figure 20 it is observed that as the release gas flow rate increases the centerline velocity and volume fraction increases.

Figure 21 shows the effect of gas flow rate on the time taken for the first gas bubble to reach the surface (rise time). It also shows the difference in simulation and experimental rise time results. It is found that as the gas flow rate increases the rise time decreases. This is due to the fact that as the flow rate increases the initial momentum and buoyancy force is greater, causing the gas to rise faster. From the Figure it can be deduced that the simulated rise times are greater than the experimental rise times. The percentage errors between the simulation and experiment rise times for release rates 0.05, 0.1 and 0.45 m3/s are 35, 46 and 53 %. This may be due to the fact that it is unknown how the rise time is described in the experiment; the value is obtained qualitatively by observing the flow and using a stopwatch. Whereas the rise time result is obtained using a quantitative approach from the simulations; by defining the volume fraction at the surface to a value and determining the time for the volume fraction to reach the prescribed value. This may be the cause of the consistent error different of approximately 2 seconds between the simulation and experimental values. Therefore it can be believed that the simulations are consistent with the experimental data.

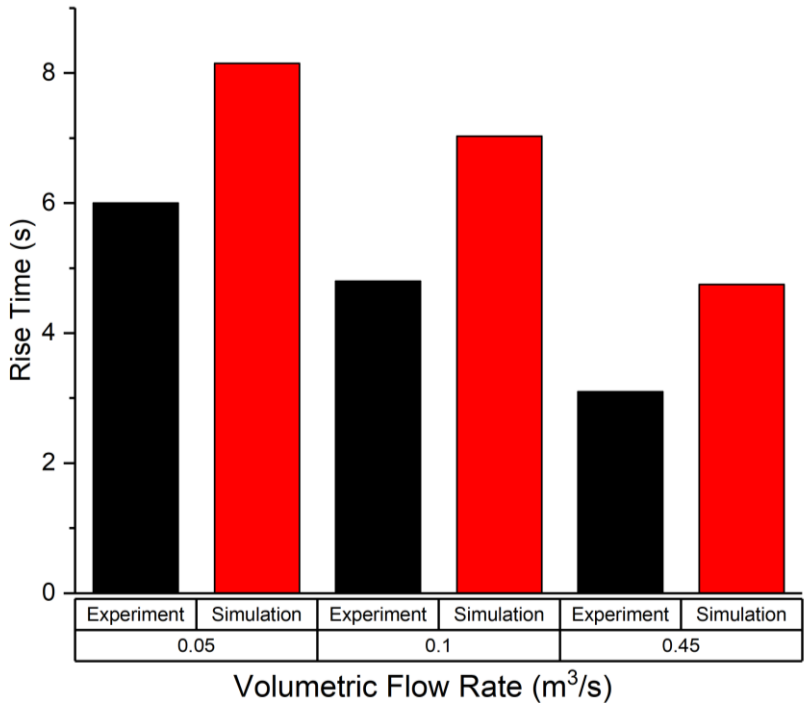

Figure 21: Comparison of simulation and experimental results for rise time.

Next, the results for maximum fountain height were analyzed. The results are presented in Figure 22. The experiment only provided data for the maximum fountain height for two release rates, 0.05 and 0.1 m^3/s, therefore only results for these points are presented. It is found that as the gas flow rate increases the maximum fountain height increases. This is because as the release rate increases the buoyancy, turbulence and drag increases which entrains the liquid upwards. Also, from the Figure it can be observed that the simulation fountain heights compared extremely well to the experimental data. The percentage errors between the simulation and experiment for release rates 0.05 m^3/s and 0.1 m^3/s are 3 % and 6 %, respectively.

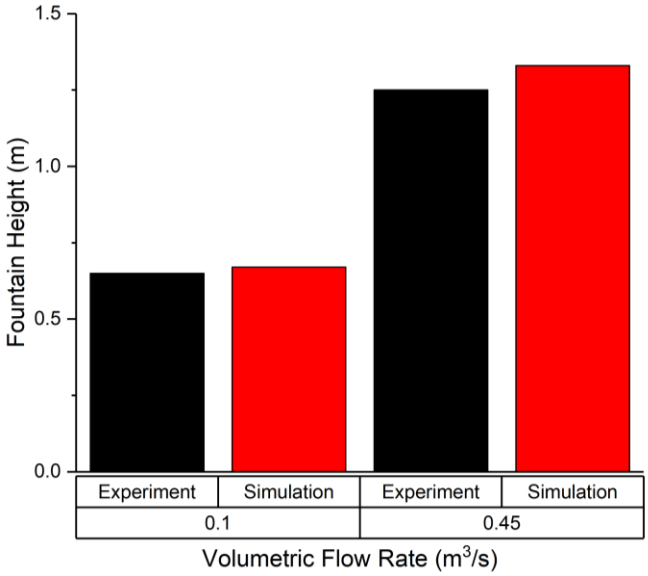

Figure 22: Comparison of simulation and experimental results for maximum fountain height, for two different volumetric flow rates.

After analyzing and comparing the simulation and experiment results for centerline velocity, centerline volume fraction, rise time and maximum fountain height it can be concluded that the simulations are consistent with the experimental data. The model is in good agreement with the experiment.

In general it was found that as the gas flow rate increased the discrepancies between the simulation and experiment increased. This was due to the fact that an increase in flow rate leads to an increase in the initial momentum of the jet, and unlike the experimental setup the CFD model does not have a momentum trap near the source to reduce the jet region. This is only a problem for very small release depths such as 7 m, and therefore the discrepancies can be overlooked in this project. This is because the goal of this project is to design a model for a real case scenario for Qatar, where the average water depth is around 50 m.

9 MODEL EXPANSION AND DATA COLLECTION

The main objective of this project is to develop a nomograph, for the release of sour gas in shallow waters such as the Arabian Gulf. In order to do this data must be collected in order to understand the behavior of the bubble plume when a subsea release occurs. Therefore the developed model that has been validated against experimental data will be expanded to test different scenarios and to obtain simulation results. Different release depths, release rates, hole diameters, and sour gas compositions will be tested. The Arabian Gulf has a minimum, average and maximum depth of 10, 50, and 100 m, respectively. Depths similar to the Arabian Gulf will be used for the analysis (Table 7). In 2016, Olsen et al. produced Figure 23.[1] The Figure is a plot of release rate versus release depth. Olsen et al. extracted all available literature data to construct the Figure. The authors identified that data is available for depths between 1 and 1000 m with release rates between 0.001 and 10 kg/s. However there is no existing data for release rate above 10 kg/s indicating a range of concern. Release rates within this range of concern, which are suitable for the developed model will be tested (Table 7). For subsea gas pipelines small, medium or large holes may result. A small hole is usually one with a diameter of 5 mm and a large hole with a diameter of 25 mm. Hole diameters within this range will be tested (Table 7). In general the content of H_2S in sour gas does not exceed 25% by mass, therefore concentrations of H_2S below this level will be tested (Table 7). A H_2S content of 11 % by mass is tested as it is the content found in sour gas from Qatar's North field.

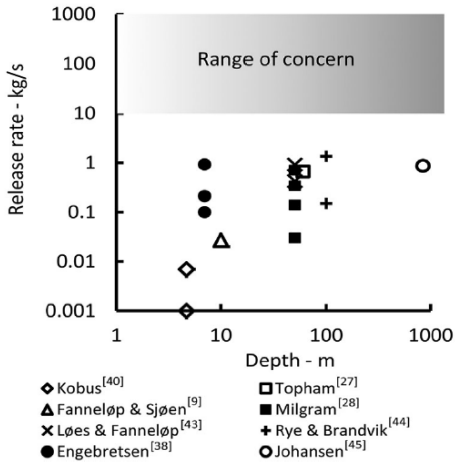

Figure 23: Graph showing depth/release rate range of concern.

Table 7: Different depths, release rates, hole diameters, hydrogen sulfide content used for sensitivity analysis

Release Depth (m)	25, 50, 100
Mass Release Flow Rate (kg/s)	20, 40, 80
Release Hole Diameter (mm)	5, 15, 25
H_2S Mass Fraction (%)	11, 22

In total 20 cases were simulated. From the 20 cases, 19 cases were simulated to obtain results for many different combinations of release depths, mass release rates and hole diameters with a constant H_2S content of 11% by mass. As it resembles the gas composition found in Qatar's sour gas reserves. The 20^{th} case was simulated for a depth of 50 m, release rate of 20 kg/s, hole diameter of 25 mm, and H_2S content of 22 % by mass. Results for only two H_2S gas contents were obtained.

In order to obtain the results the model geometry was modified, the water body depth was extended to 27, 52 and 102 m, and the atmosphere body was extended to 10 and 15 m. The width of the bodies was extended to 60 and 100 m. The hole diameters were changed depending on what case was being simulated. The mesh was updated automatically by the meshing in ANSYS Workbench. The sizes of the mesh elements were equivalent to those described above in the meshing methodology section. In the fluent setup the mass flow rate boundary condition was changed depending on what case was being simulated. The under relaxation factors were altered to achieve convergence of results. The simulations were completed using the Supercomputer hardware RAAD2 using 48 CPUs. The simulation times ranged between 5 to 15 days for different cases for approximately 20-30 s of release. For each case results regarding the surface mass flux, rise time and gas concentrations at the surface were collected. Time series was obtained for the surface mass flux, CH_4 and H_2S surface concentrations, as shown below in Figure 24. From the time series, the results were averaged when steady state was reached and recorded in a table. In order to obtain the rise time result, the time step at which the volume fraction of sour gas at the surface exceeds 0 was recorded.

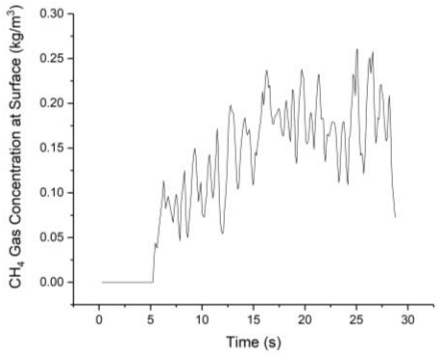

Figure 24: Graph showing the time series of CH_4 surface gas concentration.

Table 8 shows details of all simulations performed with the results obtained. This data is used for the sensitivity analysis and nomograph development.

Table 8: List of all simulations performed and the simulation results.

Case	Release Height	Release Diameter	Mass Flowrate	H_2S Gas Content	Surface Mass Flux	CH_4 Surface Concentration	H_2S Surface Concentration	Rise Time
	(m)	(m)	(kg/s)	(%)	(kg/m^2s)	(kg/m^3)	(kg/m^3)	(s)
1	25	0.05	20	11	0.006	0.0921	0.0114	3.534
2	25	0.05	40	11	0.0113	0.1554	0.0192	2.734
3	25	0.05	80	11	0.0242	0.1836	0.0107	2.009
4	25	0.15	20	11	0.0054	0.0741	0.0043	3.662
5	25	0.15	40	11	0.0131	0.1356	0.0079	2.941
6	25	0.15	80	11	0.0241	0.1449	0.0084	2.048
7	25	0.25	20	11	0.0055	0.076	0.0045	3.787
8	25	0.25	40	11	0.0116	0.0992	0.0058	3.787
9	25	0.25	80	11	0.0245	0.2035	0.0118	2.230
10	50	0.05	20	11	0.0015	0.0719	0.0089	6.507
11	50	0.05	40	11	0.0029	0.1552	0.0193	5.226
12	50	0.15	20	11	0.0016	0.0789	0.0098	6.661
13	50	0.15	40	11	0.003	0.1222	0.0152	5.364
14	50	0.15	80	11	0.0079	0.1467	0.0181	5.220
15	50	0.25	20	11	0.0018	0.0815	0.0101	6.957
16	50	0.25	20	22	0.0016	0.0834	0.0236	6.914
17	50	0.25	40	11	0.0035	0.1103	0.0136	6.043
18	50	0.25	80	11	0.008	0.1666	0.0206	4.786
19	100	0.15	80	11	0.0086	0.0782	0.0098	10.12
20	100	0.25	80	11	0.0057	0.0858	0.0109	10.17

10 SENSITIVITY ANALYSIS

10.1 Effect of Mass Release Flow Rate

To study the effect of gas release rate on the behavior of gas dispersion underwater, the simulations for three scenarios with release rates of 20, 40 and 80 kg/s (11 % by mass H_2S content) at water depth of 50 m from release hole diameter of 15 mm were conducted. The results are displayed in Figure 25. Figure 25(b) displays a graph of rise time against mass flow rate. Figure 25(b) conveys that as the mass release flow rate increases the rise time decreases. When the mass flow rate is smaller, the initial momentum from the release is smaller, so it takes longer for the bubble plume to rise to the surface. Figure 25(a) shows that when the mass flow rate increases the surface mass flux increases. Figure 25(c) and Figure 25(d) show that the amount of CH_4 and H_2S gas found on the surface increases with increasing mass flow rate. When the mass flow rate is greater more gas reaches the surface. There is almost a linear trend for the surface mass flux and surface gas concentrations. Figure 25(c) and Figure 25(d) have two lines indicating the Upper Flammability Limit (UEL) which is the maximum concentration of the gas that will burn in air and the Lower Flammability Limit (LEL) which is the minimum concentration of the gas that will burn in air. The concentration results in Figure 25(c) indicate that as the mass flow rate increases the CH_4 surface gas concentration increases beyond the UEL, going outside the flammability range. This suggests that there is higher risk of fire and explosion at the surface for smaller mass release flow rates. However as the gas disperses in the atmosphere the concentrations may dilute, falling within the flammability range somewhere away from the surface for all simulated cases. It is possible for the gas to ignite and result in fire or explosion issues. These results can be used as inputs for dispersion modeling in order to determine which offshore facilities will be in the vicinity of the flammable cloud. As from the dispersion modeling the concentration at a given distance

from the surface of sea can be found. In Figure 25(d) the green line represents 10 % of the LEL for H_2S and the orange line represents 50 % of the LEL of H_2S. The surface H_2S concentrations for all mass flow rates are below the LEL 40000 ppm, suggesting that the gas will not ignite as the concentrations are outside of the flammability range of H_2S. There is an additional line to the lines for 10 % and 50 % LEL showing the Immediately Dangerous to Life or Health (IDLH) limit which is the maximum exposure concentration for a toxic gas. From Figure 25(d) it can be seen that at all mass release flow rates the H_2S gas concentration at the surface is well above the IDLH limit of 100 ppm for H_2S gas, expressing a huge risk to human life. The Acute Exposure Guideline Levels, AEGL-3 is an estimate of the airborne concentration where individuals can experience life threatening health effects or death. The value of AEGL-3 for H_2S for an exposure duration of 1 hour is 50 ppm. The Emergency Response Planning Guidelines, EPRG-3 is the maximum concentration that individuals can be exposed to for an hour without facing adverse health effects or death. For H_2S the value is 100 ppm. At the surface the concentrations of H_2S for all cases is much larger than all the described toxic exposure limits. Individuals at the surface would die due to the high concentrations they are exposed to, based on their exposure times. Individuals within the vicinity of the toxic cloud may face irreversible adverse health effects or death. The sour gas composition found at the surface is almost equivalent to the initial sour gas composition, suggesting that very little H_2S is absorbed into the water, for all different mass flow rates.

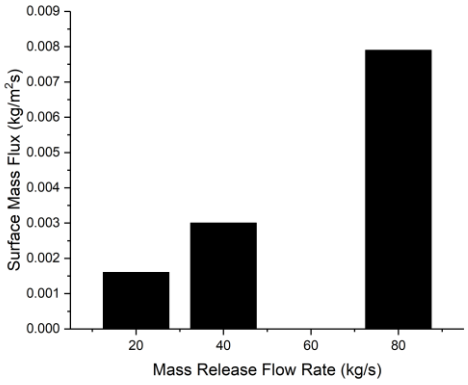

(a)Surface Mass Flux (kg/m2s)

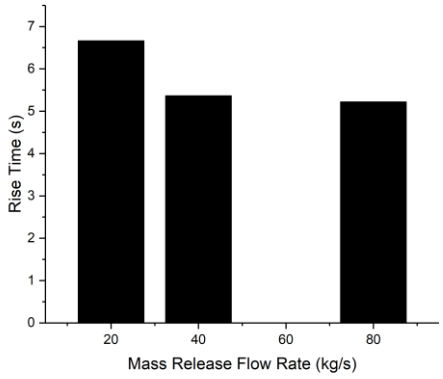

(b)Rise Time (s)

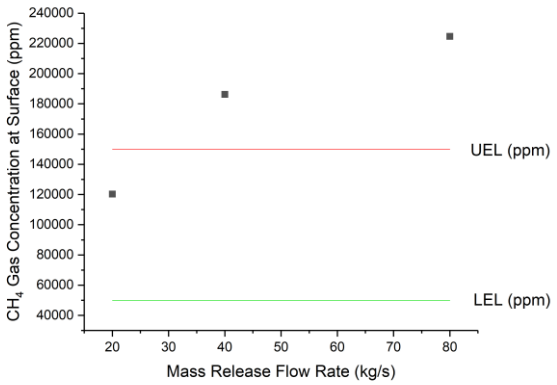

(c)CH4 Surface Gas Concentration (ppm) displayed along with the UEL and LEL of CH_4

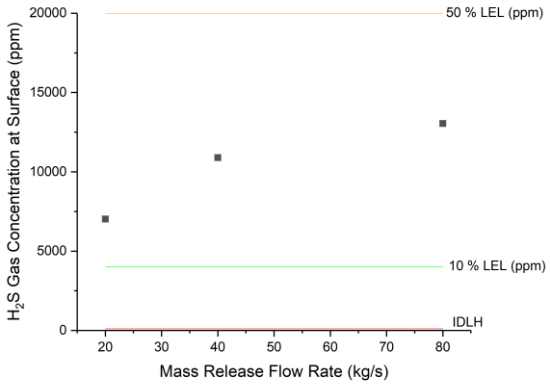

(d)H2S Surface Gas Concentration (ppm) displayed along with 10 % and 50% of the LEL and the IDLH limit

Figure 25: Effect of mass flow rate on surface mass flux (a), rise time (b), CH_4 surface gas concentration (c), and H_2S surface gas concentration (d) results for underwater gas release from 50 m depth and 15 mm hole diameter.

10.2 Effect of H_2S Content in Released Gas

To study the effect of the H_2S content in the sour gas on the behavior of underwater gas dispersion, the simulations of underwater release of 20 kg/s of gas from a hole size of 25 mm at a

depth of 50 m were conducted for two scenarios with H_2S gas content of 11 and 22 % by mass. Figure 26 presents the comparison results. Figure 26(a) indicates that as the H_2S sour gas content is doubled from 11 % to 22 % the surface mass flux decreases. Figure 26(b) indicates that the H_2S content has no significant effect on the rise time. Almost the same amount of time is required for the gas to rise to the surface. Figure 26(d) shows that as the H_2S gas content increases from 11 % to 22 % the amount of H_2S that rises above the surface increases. As the H_2S content is increased the H_2S surface concentration is closer to 50 % of the LEL. For both cases, the H_2S concentration is above the IDLH exposure limit.

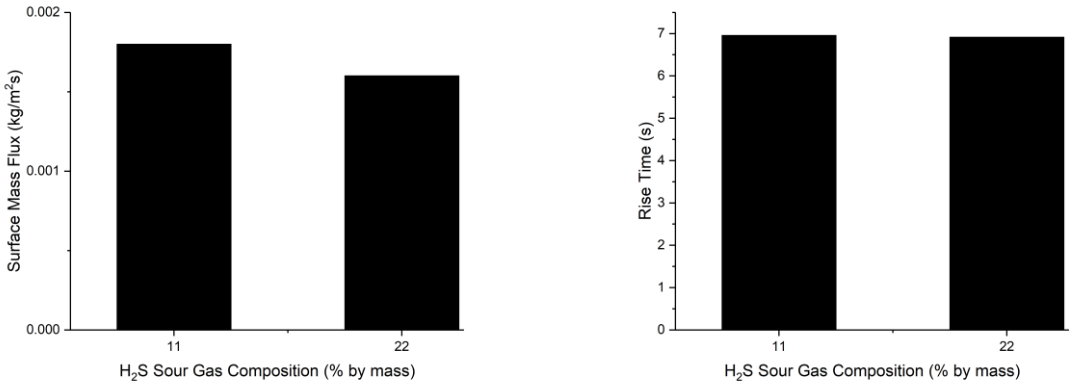

(a)Surface Mass Flux (kg/m^2s) (b)Rise Time (s)

Figure 26: Effect of H_2S content in sour gas on surface mass flux (a), rise time (b), CH_4 surface gas concentration (c), and H_2S surface gas concentration (d) results for underwater gas release of 20 kg/s from 50 m depth and 25 mm hole diameter.

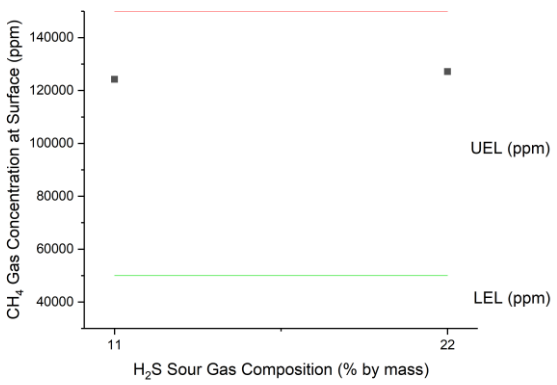

(c)CH_4 Surface Gas Concentration (ppm) displayed along with the UEL and LEL of CH_4

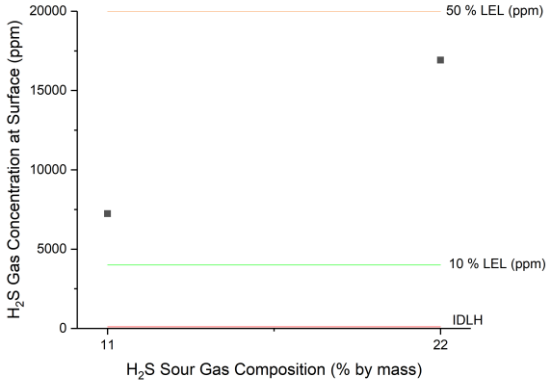

(d)H_2S Surface Gas Concentration (ppm) displayed along with 10 % and 50% of the LEL and the IDLH limit

Figure 26: Continued.

10.3 Effect of Release Depth

Different regions of the Arabian Gulf have different depths, therefore is it important to understand the effect of release depth on the dispersion of underwater release of sour gas. To study the effect of release depth, simulations for release of 80 kg/s of sour gas (11% by mass of H_2S) from a hole diameter of 25 mm were conducted for three scenarios 25 m, 50 m and 100 m depth. Figure 27 displays the results for comparison. Figure 27(a) and Figure 27(b) indicate that as the release depth increases the rise time increases and the surface mass flux decreases. When gas is released in deeper water it takes more time for the bubbles to reach the surface generating greater rise times and smaller surface mass fluxes. Similarly, Figure 27(c) shows that as the release depth increases, the amount of CH_4 on the surface decreases. For release depths of 25 and 50 m the surface concentration of CH_4 fall outside the flammability range. However for release depth of

100 m the CH_4 surface concentration is within the flammability range and so the gas can ignite resulting in a fire or explosion. From Figure 27(d) it can be seen that the general trend is followed, the H_2S surface gas concentration decreases with increasing release depth. However there is an anomalous point for 50 m depth, which should be discarded from the data set. The H_2S gas concentration is above 10 % of the LEL and exceeds the IDLH exposure limit, suggesting a highly toxic area around the surface.

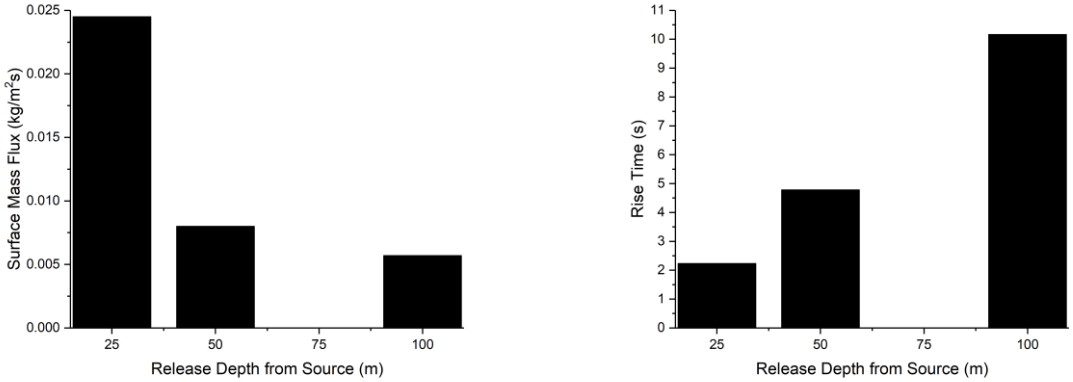

(a)Surface Mass Flux (kg/m^{2}s) (b)Rise Time (s)

Figure 27: Effect of release depth on surface mass flux (a), rise time (b), CH_4 surface gas concentration (c), and H_2S surface gas concentration (d) results for underwater gas release of 80 kg/s from 25 mm hole diameter.

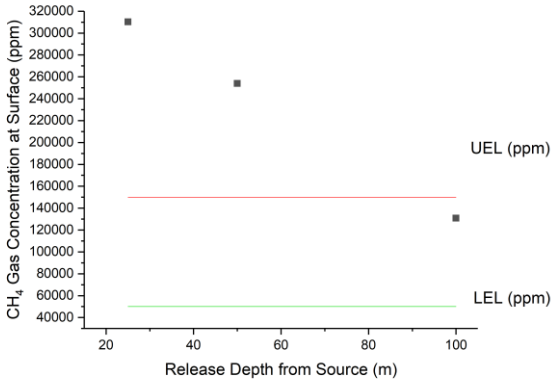

(c)CH_4 Surface Gas Concentration (ppm) displayed along with the UEL and LEL of CH_4

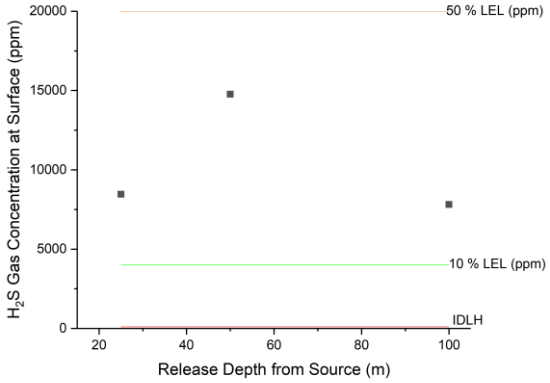

(d)H_2S Surface Gas Concentration (ppm) displayed along with 10 % and 50% of the LEL and the IDLH limit

Figure 27: Continued.

10.4 Effect of Hole Diameter

Due to uncertainty of the accident, release may happen from different sized holes in a subsea gas pipeline. To study the effect of release hole size on the dispersion simulations for release of 20 kg/s of sour gas (11% by mass of H2S) at water depth of 50 m from release point were conducted for three scenarios 0.05 m, 0.15 m and 0.25 m hole diameters. The results are presented in Figure 28. Figure 28(b) shows that as the hole diameter increases there is a slight increase in rise time. As the mass flow rate is kept constant, an increase in hole diameter, suggests a decrease in the initial velocity which leads to a longer rise time. From Figure 28(a), Figure 28(c) and Figure 28(d) it can be found that as the release hole diameter increases more gas rises to the surface, as the surface mass flux, CH_4 and H_2S surface gas concentration increases. The gas concentrations fall between the flammability limits for CH_4 suggesting that a flammable cloud is

present at the surface. The H_2S concentrations exceed the IDLH for H_2S suggesting a toxic environment at the surface for human and industry activities.

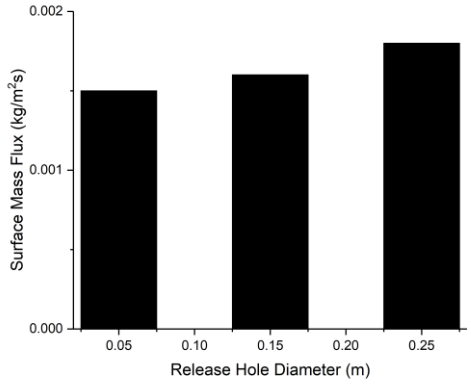

(a)Surface Mass Flux (kg/m^{2}s)

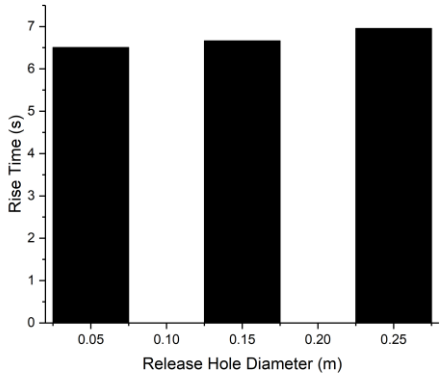

(b)Rise Time (s)

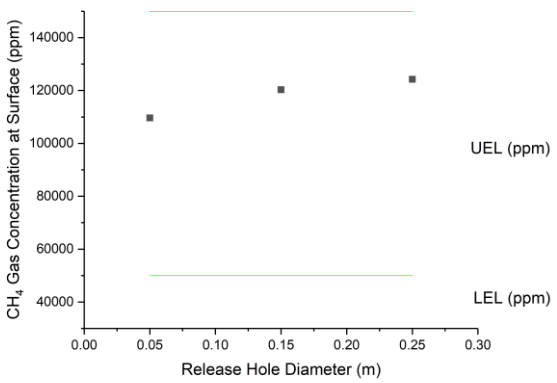

(c)CH_4 Surface Gas Concentration (ppm) displayed along with the UEL and LEL of CH_4

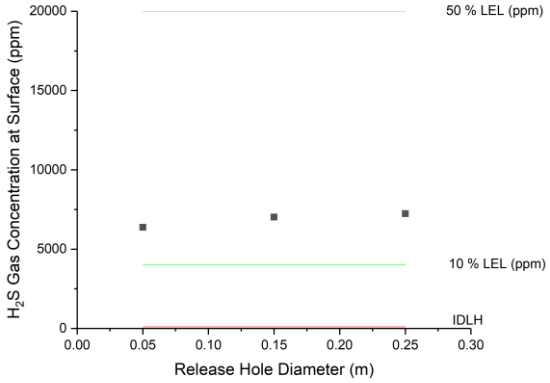

(d)H_2S Surface Gas Concentration (ppm) displayed along with 10 % and 50% of the LEL and the IDLH limit

Figure 28: Effect of release hole diameter on surface mass flux (a), rise time (b), CH_4 surface gas concentration (c), and H_2S surface gas concentration (d) results for underwater gas release of 20 kg/s from 50 m depth.

11 DIMENSIONLESS ANALYSIS

Dimensionless analysis is performed in order to determine the relationships between various parameters that are used to describe the phenomena of a subsea gas release. Considering all the main factors affecting the behavior of the bubble plume from the developed CFD model, the independent variables are defined, for an isothermal system with constant H_2S sour gas content. The dependent variables; rise time, surface mass flux, and surface gas concentrations are affected by the following independent parameters:

1. The height from the release point, H_o
2. The pipeline hole diameter, D_h
3. The release mass flow rate, $\dot{m}$

The dimensions of the variables are displayed below in Table 9.

Table 9: Dimensions of all variables used for dimensionless analysis.

Variables In the System				
Name	Symbol	Units		
		L (m)	M (kg)	T (s)
Release Height	H_o	1	0	0
Release Hole Diameter	D_h	1	0	0
Release Mass Flowrate	$\dot{m}$	0	1	-1
Gravitational Acceleration	g	1	0	-2
Rise time	Rt	0	0	1
Surface Mass Flux	SMF_g	-2	1	-1
Surface Gas Concentration	SC_g	-3	1	0

According the Buckingham π theorem, using dimensionless analysis the general functional form for the dependent variables is the following:

$$Surface\ Mass\ Flux, SMF_g = f(H_o, D_h, \dot{m}, g) \quad \textbf{Equation 59}$$

$$Rise\ Time, Rt = f(H_o, D_h, \dot{m}, g) \quad \textbf{Equation 60}$$

$$Surface\ Gas\ Concentration, SC_g = f(H_o, D_h, \dot{m}, g) \quad \textbf{Equation 61}$$

Using the analysis of Buckingham π theorem, the number of dimensionless groups were determined, which is equivalent to number of variables minus the number of different dimensions of the variables.

$$Number\ of\ Dimensionless\ Groups = 7 - 3 = 4$$

As there are three different dimensions for the variables, three reference variables are chosen; H_o, $\dot{m}$, and g.

$$\Pi_1 = (H_o)^{a_1}(\dot{m})^{b_1}(g)^{c_1}D_h \quad \textbf{Equation 62}$$

$$\Pi_2 = (H_o)^{a_2}(\dot{m})^{b_2}(g)^{c_2}Rt \quad \textbf{Equation 63}$$

$$\Pi_3 = (H_o)^{a_3}(\dot{m})^{b_3}(g)^{c_3}SMF_g \quad \textbf{Equation 64}$$

$$\Pi_4 = (H_o)^{a_4}(\dot{m})^{b_4}(g)^{c_4}SC_g \quad \textbf{Equation 65}$$

For Π_1 writing the dimensions for all the variables the following equation is obtained:

$$L^0M^0T^0 = (L)^{a_1}(MT^{-1})^{b_1}(LT^{-2})^{c_1}(L) \quad \textbf{Equation 66}$$

From the above equation the following exponential equations are obtained:

$$L: a_1 + c_1 + 1 = 0 \quad \textbf{Equation 67}$$

$$M: b_1 = 0 \quad \textbf{Equation 68}$$

$$T: -b_1 - 2c_1 = 0 \quad \textbf{Equation 69}$$

Solving for the constants, $b_1 = 0$, $c_1 = 0$, and $a_1 = -1$, therefore the first dimensionless group is:

$$\Pi_1 = \frac{D_h}{H_o} \quad \textbf{Equation 70}$$

Similarly, constants for the other groups are obtained giving the following dimensionless numbers:

$$\Pi_2 = \frac{g^{\frac{1}{2}} Rt}{{H_o}^{\frac{1}{2}}} \quad \textbf{Equation 71}$$

$$\Pi_3 = \frac{{H_o}^2 SMF_g}{\dot{m}} \quad \textbf{Equation 72}$$

$$\Pi_4 = \frac{{H_o}^{\frac{5}{2}} g^{\frac{1}{2}} SC_g}{\dot{m}} \quad \textbf{Equation 73}$$

From the list of dimensionless numbers created, it can be seen that no dimensionless group exists that contains the mass flow rate and other independent variables. The inclusion of such a dimensionless number will allow for the identification of relationships of dependent variables with dimensionless groups consisting of only independent variables. Therefore an additional variable will be added, gas density. The gas density is a known quantity that remains constant for all

simulation scenarios, as the gas composition is constant. The additional dimensionless number created with the gas density is:

$$\Pi_5{}' = \frac{H_o{}^{\frac{5}{2}}\, g^{\frac{1}{2}}\, \rho_g}{\dot{m}} \qquad \textbf{Equation 74}$$

The inverse of this dimensionless group is used in the following sections:

$$\Pi_5 = \frac{\dot{m}}{H_o{}^{\frac{5}{2}}\, g^{\frac{1}{2}}\, \rho_g} \qquad \textbf{Equation 75}$$

12 NOMOGRAPH DEVELOPMENT

12.1 Steps Preformed to Construct Nomograph

The dimensionless groups generated in the previous section will be utilized to create a nomograph that can be used to determine important subsea gas release parameters such as rise time, surface mass flux and surface gas concentrations from known variables such as release depth, release hole diameter and release mass flow rate.

In order to create the nomograph relationships between the different dimensionless groups need to be determined. All simulation results shown in Table 8 were converted into their dimensionless forms. Using Origin 2017 a correlation matrix was constructed to visualize the correlations between all combinations of the dimensionless groups (Figure 29).

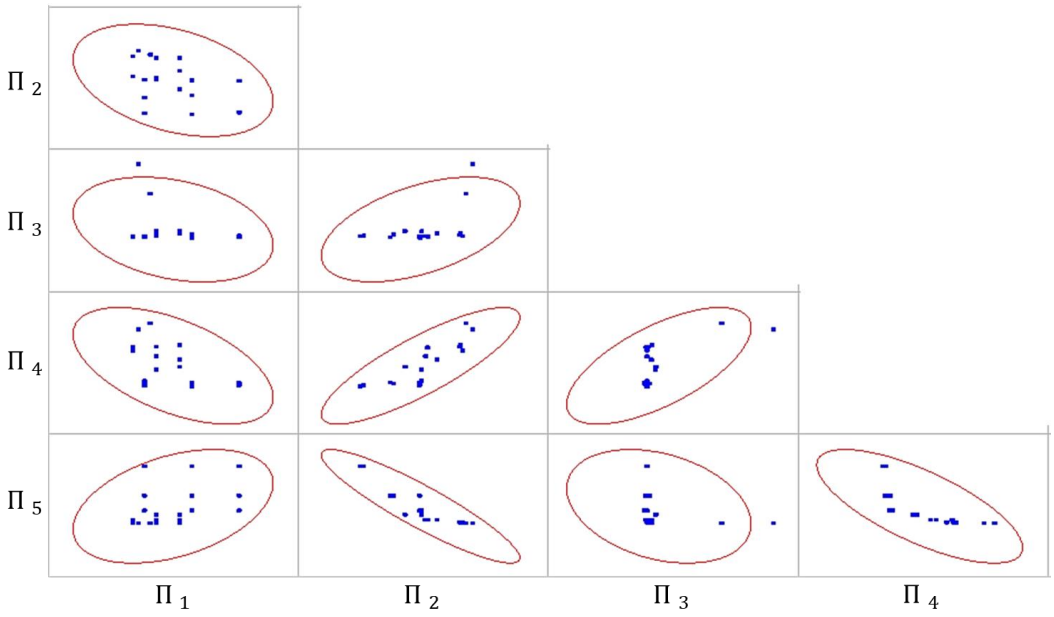

Figure 29: Correlation matrix showing the correlations between different combinations of the derived dimensionless groups.

From the correlation matrix it can be observed that there is a very strong correlation between Π_5 and Π_2 and between Π_2 and Π_4. The matrix also suggests that there are no significant relationships between Π_1 and any dimensionless group, the results are scattered. Observing the graphs consisting of dimensionless group Π_3 it can be concluded that 2 data points for the surface mass flux are anomalous, and should be discarded to obtain better correlations. After discarding the anomalies Pearson's correlation coefficient was calculated for three scenarios, Π_2 against Π_3, Π_4 against Π_3, and Π_5 against Π_3. Pearson's correlation coefficient is a statistic that measures the linear correlation between a pair of variables. The values obtained for Pearson's correlation coefficient for the three scenarios are 0.16, 0.33, and -0.27 suggesting that Π_3 is the most related to Π_4.

Using the information obtained from the correlation matrix relationships between different dimensionless groups can be formed to generate the nomograph. Knowing that Π_2 a dimensionless group consisting of the rise time is a function of Π_5 which is a group containing the independent variables mass flow rate and release height, the data for these variables can be fitted to determine the form of the function. Figure 30(a) shows the graph of Π_2 versus Π_5 for different hole diameters. The graph conveys that the data fits a logarithmic distribution. The fit for each hole diameter follows the same trend. The plot is shifted upwards by a factor when the hole diameter is increased. Another dimensionless group can be introduced to account for the effect of hole diameter on the Π_2 results. Depending on the value of $\frac{D_h}{D_{h_0}}$ where D_{h_0} is the reference hole diameter 0.05 m, a correction factor can be determined to compute the value of Π_2 for a specific hole diameter based on the value of Π_2 for a 0.05 m hole diameter. This procedure is displayed below in Figure 30(b). When the results obtained from the black line (hole diameter equal to 0.05 m) are multiplied by 1.026 the light blue line is formed which is equivalent to the results obtained

when the hole diameter is equal to 0.15 m. When the results obtained from the black line are multiplied by 1.067 the red line is formed which is equivalent to the results obtained when the hole diameter is 0.25 m. A relationship is obtained between the correction factor and hole diameter shown in Figure 31 which can be used along with the logarithmic relationship of Π_2 versus Π_5 for hole diameter of 0.05 m to determine the value for Π_2 for different hole diameters.

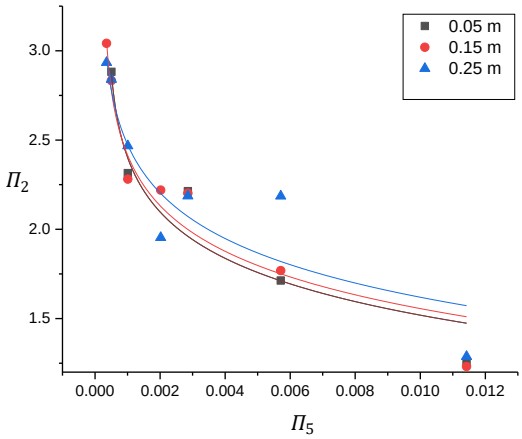

(a) Data points and logarithmic fittings

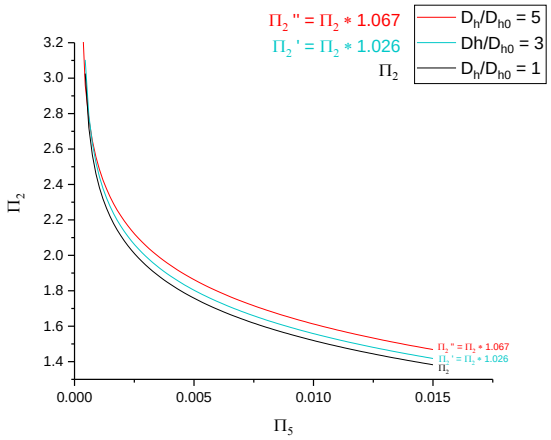

(b) Graph showing how a correction factor can be used to determine the value of Π_2 for different release hole diameters given a curve for a hole diameter of 0.05 m.

Figure 30: Graph of Π_2 versus Π_5 for different hole diameters.

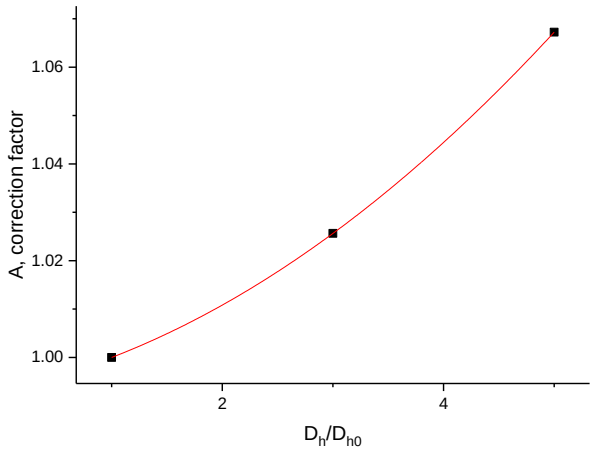

Figure 31: Graph used to obtained the correction factor from the given hole diameter and reference hole diameter of 0.05 m

From the correlation matrix it is also known that there is a relationship between Π_2 and Π_4. Figure 32 shows a plot of all data points of Π_4 against Π_2. From the Figure it can be determined that the data fits a polynomial of order 2. For this plot the R squared value is found to be 0.80. The R squared value is a statistical measurement of the fitting showing how much of the variation of a dependent variable can be explained by the independent variable. As the value obtained is very close to 1 the polynomial model is a good fit for the data.

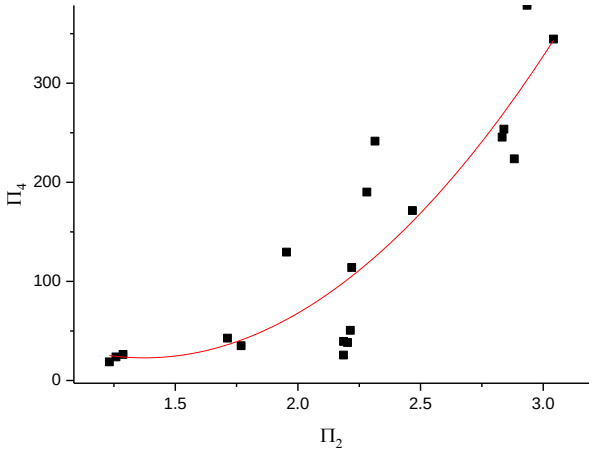

Figure 32: Graph of Π_4 versus Π_2 showing the data points and polynomial fitting.

Additionally from the correlation matrix we concluded that Π_3 is correlated to Π_4. Figure 33 shows that the data is fitted linearly. The data points are slightly scattered from the linear fit and the calculated R squared value is lower than 0.5. Therefore it is recommended to obtain more simulation results in order to accurately predict the relationship between Π_3 and Π_4. For the current situation, only 20 data points are used for this graph, we can assume that the fit is a good fit for the data, as the basic trend seen in the results, an increase in Π_3 for an increase is Π_4 is visualized.

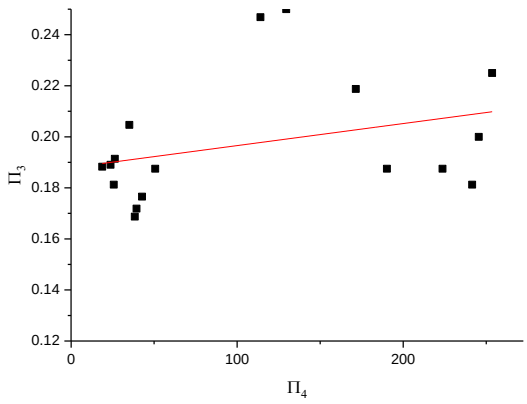

Figure 33: Graph of Π_3 versus Π_4 showing the data points and linear fitting.

12.2 Nomograph and How to Use it

The above mentioned relationships were combined to generate the nomograph shown in Figure 34. For a underwater sour gas release of gas composition 11 % H_2S and 89 % CH_4 by mass from a known release height, release hole diameter and release mass flow rate, the value of dimensionless group $\frac{\dot{m}}{H_o^{\frac{5}{2}} g^{\frac{1}{2}} \rho_g}$ can be calculated. Lay a ruler and draw a straight line from this calculated value on the scale on the left hand side of the nomograph and draw a straight line to the solid black logarithmic curve. Then rotate the ruler 90 degrees clockwise and draw a straight line crossing the scale at the bottom of the nomogram for the dimensionless group $\frac{g^{\frac{1}{2}} Rt}{H_o^{\frac{1}{2}}}$. Then using the known release hole diameter calculate the value for $\frac{D_h}{D_{h_0}}$ given that D_{h_0} is equal to 0.05 m. Use this value on the x- axis of the small graph placed in the center, top part of the nomograph to find the value of A the correction factor. Multiply the value of the correction factor with the obtained value of $\frac{g^{\frac{1}{2}} Rt}{H_o^{\frac{1}{2}}}$ to determine the corrected value for the dimensionless group consisting of the rise

time. Lay a ruler at the corrected value of $\frac{g^{\frac{1}{2}} Rt}{H_o^{\frac{1}{2}}}$ on the bottom scale of the nomograph and draw a straight line to the dotted black polynomial curve. Rotate the ruler 90 degrees clockwise and draw a straight line crossing the scales on the right side of the nomograph. From the first scale on the right hand side read the value of $\frac{H_o^{\frac{5}{2}} g^{\frac{1}{2}} SC_g}{\dot{m}}$ and from the second scale on the right side read the value of $\frac{{H_o}^2 SMF_g}{\dot{m}}$. From the numbers obtained and the given information of release height, mass flow rate and release hole diameter calculate the rise time, surface mass flux and surface gas concentration. The surface CH_4 and H_2S concentrations can be determined by multiplying the surface gas concentration obtained from the nomograph by 0.89 and 0.11, respectively. These parameters can aid in risk assessments. The rise time gives an indication of how long it will take the gas to surface after release. The surface mass flux and surface gas concentrations can be used as inputs for dispersion modelling to evaluate if offshore facilities are within the vicinity of flammable or toxic clouds. For subsea gas releases, valuable parameters related to safety concerns such as the behavior of the gas plume, when the gas will surface, how much gas is released can be obtained from the nomograph in a quick and easy way. These parameters provide guidance for further consequence modelling and defining exclusion zones that can aid in risk assessment and emergency response planning.

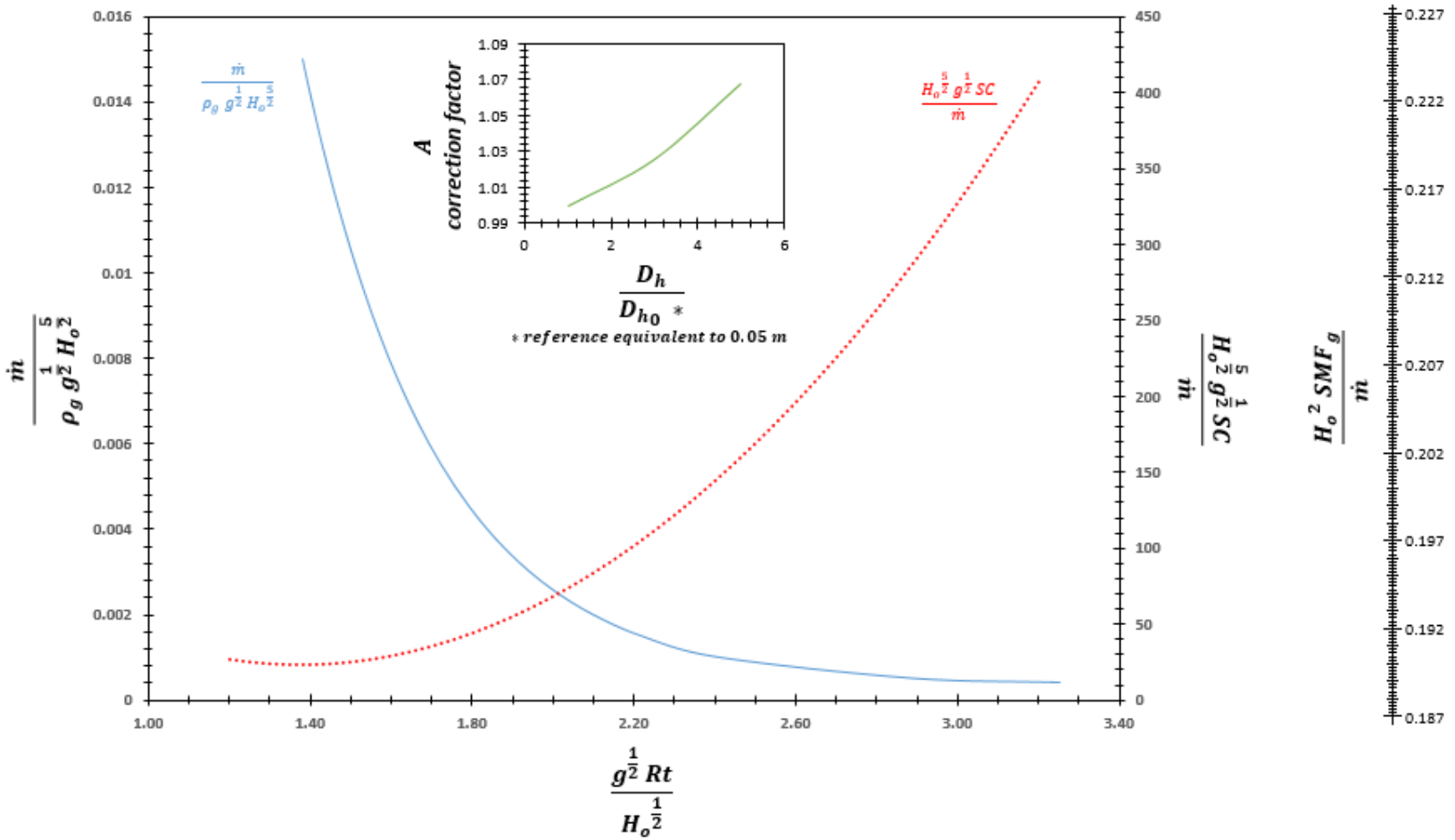

Figure 34: Nomograph developed to determine rise time, surface mass flux, and surface gas concentration for subsea release of sour gas (11 % H_2S and 89 % CH_4 by mass) from a rupture in a pipeline, for given release height, release hole diameter and release mass flow.

12.3 Uncertainty Analysis

An uncertainty analysis will be performed on the developed nomograph to determine the reliability of the predication of parameters from the nomograph. There a numerous problems that lead to uncertainties in prediction of parameters:

- Uncertainties due to measurements of release height, release mass flow rate, release hole diameter and gas density.
- Precision uncertainties arising due to the regression modeling performed to determine relationships between dimensionless groups. These models are developed using the simulation results obtained and therefore the uncertainties are linked to the uncertainties of the simulations.
    - Uncertainties due to goodness of fit of regression model between $\frac{\dot{m}}{{H_o}^{\frac{5}{2}} g^{\frac{1}{2}} \rho_g}$ and $\frac{g^{\frac{1}{2}} Rt}{{H_o}^{\frac{1}{2}}}$.
    - Uncertainties due to goodness of fit of regression model between $\frac{D_h}{D_{h_0}}$ and A the correction factor.
    - Uncertainties due to goodness of fit of regression model between $\frac{g^{\frac{1}{2}} Rt}{{H_o}^{\frac{1}{2}}}$ and $\frac{{H_o}^{\frac{5}{2}} g^{\frac{1}{2}} SC_g}{\dot{m}}$.
    - Uncertainties due to goodness of fit of regression model between $\frac{{H_o}^{\frac{5}{2}} g^{\frac{1}{2}} SC_g}{\dot{m}}$ and $\frac{{H_o}^2 SMF_g}{\dot{m}}$.

12.3.1 Assumptions

Measurement uncertainties for the release depth, mass flow rate, hole diameter and gas density are assumed to compute the uncertainties of the desired variables from the nomograph.

- It is assumed that for the release depth the uncertainty is 5 m plus 5 % of the depth:
    - For 25 m depth the uncertainty is ± 6.25 m
    - For 50 m depth the uncertainty is ± 7.5 m
    - For 100 m depth the uncertainty is ± 10 m
- For the release mass flow rate the uncertainty is assumed to be ± 0.5 kg/s as it is likely that for a measured flow rate of 20 kg/s the actual flowrate lies between 19.5 and 20.5 kg/s.
- For the release hole diameter the uncertainty is assumed to be ± 0.01 m, considering that the hole diameter can precisely be measured up to the millimeter.
- It is assumed that the uncertainty for gas density is approximately 5 % of the gas density, giving an uncertainty of ± 0.03 kg/m^3 for the nomograph.

12.3.2 Computation of Uncertainties of Results Obtained from Nomograph

In order to calculate the uncertainties for the rise time, surface gas concentration and surface mass flux results, the following error propagation formulas are used:

For a quantity (y) that is a function of one variable (x) the uncertainty (δy) is:

$$\delta y = \left|\frac{dy}{dx}\right| \delta x \qquad \textbf{Equation 76}$$

For a quantity (y) that is a function of many variables $(x, w \ldots, z)$ the uncertainty (δy) is:

$$\delta y = \sqrt{\left(\frac{\partial y}{\partial x}\,\delta x\right)^2 + \left(\frac{\partial y}{\partial w}\,\delta w\right)^2 + \cdots + \left(\frac{\partial y}{\partial z}\,\delta z\right)^2} \qquad \textbf{Equation 77}$$

A number of cases are listed with different combinations of independent variables, such as the release depth, mass flow rate and hole diameter. The nomograph is used to obtain the results for rise time, surface gas concentration and surface mass flux. These results will be used in the error propagation formulas to calculate the uncertainties for each parameter.

12.3.2.1 Rise Time Uncertainty

To calculate the uncertainty in the rise time results, the uncertainty of the dimensionless groups, $\frac{\dot{m}}{H_o{}^{\frac{5}{2}}\, g^{\frac{1}{2}}\, \rho_g}$ and $\frac{D_h}{D_{h_0}}$ are calculated. These groups have measurement uncertainties of the independent variables associated to them. The formulas used to calculate the uncertainties are as follows:

$Uncertainty\ of\ \Pi_5\ , \delta\Pi_5$

$$= \sqrt{\left(\frac{1}{H_o{}^{\frac{5}{2}}\, g^{\frac{1}{2}}\, \rho_g}\,\delta\dot{m}\right)^2 + \left(-\frac{5}{2}\,\frac{\dot{m}}{H_o{}^{\frac{7}{2}}\, g^{\frac{1}{2}}\, \rho_g}\,\delta H_0\right)^2 + \left(-2\,\frac{\dot{m}}{H_o{}^{\frac{7}{2}}\, g^{\frac{1}{2}}\, \rho_g{}^2}\,\delta\rho_g\right)^2}$$

$$Uncertainty\ of\ \frac{D_h}{D_{h_0}}\ , \delta D = \frac{\delta D_h}{D_{h_0}}$$

The uncertainties of A the correction factor and the dimensionless group $\frac{g^{\frac{1}{2}}\, Rt}{H_o{}^{\frac{1}{2}}}$ are calculated using the formulas shown below. These variables have precision uncertainties arising from regression modeling associated to them.

$$Uncertainty\ of\ A\ ,\delta A = \left| 0.004\frac{D_h}{D_{h_0}} + 0.0048 \right| *\ \delta D$$

$$Uncertainty\ of\ \Pi_2\ ,\delta\Pi_2$$

$$= \sqrt{\left(\frac{-0.327\ A}{\Pi_5 - 0.000352} *\ \delta\Pi_5\right)^2 + (-0.327\ Ln(\Pi_5 - 0.000352) *\ \delta A)^2}$$

The uncertainty for rise time is calculated by the following formula:

$$Uncertainty\ of\ Rise\ Time, \delta Rt = \sqrt{\left(\frac{{H_o}^{\frac{5}{2}}}{g^{\frac{1}{2}}}\ \delta\Pi_2\right)^2 + \left(\frac{1}{2}\frac{\Pi_2}{g^{\frac{1}{2}}\ {H_o}^{\frac{1}{2}}}\ \delta H_0\right)^2}$$

The uncertainty for the different cases with different variations of release depth, hole diameter and mass flow rate were calculated. The percentage uncertainty was computed by divided the uncertainty from the result value obtained from the nomograph. The average percentage uncertainty obtained for the rise time is ± 7 % of Rise Time Result.

12.3.2.2 Surface Gas Concentration Uncertainty

For the desired parameter the surface gas concentration the uncertainty is a function of the uncertainty of the dimensionless group $\frac{g^{\frac{1}{2}}\ Rt}{{H_o}^{\frac{1}{2}}}$. The uncertainty of $\frac{g^{\frac{1}{2}}\ Rt}{{H_o}^{\frac{1}{2}}}$ is further propagated due to the precision uncertainties arising from regression modeling performed to determine the relationship between Π_2 and Π_4. The uncertainty is calculated by the following steps:

$$Uncertainty\ of\ \Pi_4\ ,\delta\Pi_4 = |-317 + 230\ \Pi_2\ | *\ \delta\Pi_2$$

$$Uncertainty\ of\ Surface\ Gas\ Concentration\ ,\delta SC_g$$

$$= \sqrt{\left(\frac{\dot{m}}{H_o^{\frac{5}{2}}\, g^{\frac{1}{2}}}\ \delta\Pi_4\right)^2 + \left(\frac{\Pi_4}{H_o^{\frac{5}{2}}\, g^{\frac{1}{2}}}\ \delta\dot{m}\right)^2 + \left(-\frac{5}{2}\frac{\Pi_4\, \dot{m}}{H_o^{\frac{7}{2}}\, g^{\frac{1}{2}}}\ \delta H_0\right)^2}$$

The average percentage uncertainty obtained for the surface gas concentration is ± 58 % of Surface Gas Concentration Result.

12.3.2.3 Surface Mass Flux Uncertainty

For the desired parameter the surface mass flux the uncertainty is a function of the uncertainty of dimensionless group $\frac{H_o^{\frac{5}{2}}\, g^{\frac{1}{2}}\, SC_g}{\dot{m}}$. The uncertainty for the surface mass flux is the greatest as it depends on all the uncertainties present in the nomograph, shown above. The uncertainty is calculated by the following steps:

$$Uncertainty\ of\ \Pi_3\ ,\delta\Pi_3 = |0.00009\,| * \delta\Pi_4$$

$$Uncertainty\ of\ Surface\ Mass\ Flux\ ,\delta SMF_g$$

$$= \sqrt{\left(\frac{\dot{m}}{{H_0}^2}\ \delta\Pi_3\right)^2 + \left(\frac{\Pi_3}{{H_0}^2}\ \delta\dot{m}\right)^2 + \left(\frac{\Pi_3\, \dot{m}}{{H_0}^3}\ \delta H_0\right)^2}$$

The average percentage uncertainty obtained for the surface mass flux is ± 21 % of Surface Mass Flux Result.

12.3.2.4 Comparison of Uncertainties of Results Obtained from the Nomograph and from the Simulations

The uncertainty for rise time, surface mass flux, and surface gas concentration for the different CFD simulated cases were calculated and compared to the uncertainties obtained from the nomograph calculated results.

For the simulation cases the rise time value is obtained by visualizing and recording the time at which the volume fraction at the surface exceeds zero. The uncertainty depends on the time step size, the number of time steps results are recorded for and the methodology used to determine the volume fraction at the surface. Taking into account the mentioned problems, the uncertainty for simulation rise time is assumed to be ± 5 % of Value.

For the simulation surface mass flux and surface gas concentration, results over time were provided by the simulation, therefore to determine the uncertainties the temporal standard deviations were computed for all simulation results and the maximum uncertainty found. The uncertainty for surface gas flux and surface gas concentration was assumed to be ± 20 % of Value and ± 24 % of Value, respectively.

The simulation uncertainties obtained are very similar to the nomograph uncertainties, which was expected as the simulation results were used to construct the nomograph. The nomograph uncertainties are directly related to the simulation uncertainties, suggesting that to improve the current nomograph the CFD model used must be improved.

13 CONCLUSIONS

There have been numerous subsea gas release incidents in the oil and gas industry. These incidents have created the need of understanding the phenomena of subsea gas releases. Understanding of the phenomena will aid in controlling the risks associated with subsea gas releases. To control the risks quantification of the likelihood of the release and the severity of the consequences is essential. A literature review study has been conducted to identify all available experimental work, integral and CFD models that are used to quantify the severity of risks associated with subsea gas releases. There is an increasing number of sour gas reserves in the Middle East, Qatar leading to greater risks to human life due to the toxicity of H_2S present in the released gas. There appears to be a lack of a model that is used to model subsea release of sour gas. Thus in this project a CFD model will be developed to model the release of sour gas in shallow waters such as the Arabian Gulf Sea in Qatar. The usage of CFD models is expensive and time consuming hence using the results obtained from the developed CFD model a nomograph was generated in order to extract data for risk assessment in an easier and more efficient way.

The CFD model was developed using Eulerian-Eulerian approach in ANSYS Fluent version 18.2. The following steps were carried out to develop the model; geometry design construction, meshing, and Fluent setup for the simulation. Various parameters were tested in order to optimize the model's performance; geometry design, choice of primary phase and choice of turbulence model. The continuous phase was selected as the primary phase and realizable k-ε model was selected for turbulence. The model was validated against Engebretsen's 1997 experiment. Results for centerline velocity and centerline volume fraction were found at three different vertical distances from the release point from the simulation results and compared to the experimental data. Rise time and maximum fountain height results were also obtained from the

simulations and compared to experimental results. Small differences were found between the simulation results and experimental data. The simulation results showed good agreement with the experimental data and therefore it was concluded that the model can predict the behavior of subsea gas release.

The validated model was expanded to predict the behavior of the bubble plume for several scenarios that fall within the range of concern for Qatar's industry, for release depths ranging between 25 and 100 m, for release mass flow rates ranging between 20 and 80 kg/s, for release hole diameters ranging between 0.05 and 0.25 m and for sour gases with H_2S compositions of 11 and 22 % by mass. The simulation results were used to perform a sensitivity analysis. From the sensitivity analysis it was concluded that for values of release depths, release mass flow rates, release hole diameters and H_2S compositions within the abovementioned ranges the H_2S levels on the surface are always above the IDLH and therefore present a serious risk to human life. Additionally the CH_4 levels on the surface are mostly within the flammability range and present risk of fire or explosion on the surface. The sensitivity analysis indicated that the results obtained are very useful as they can be used as inputs for dispersion modelling to determine what offshore facilities are within the vicinity of flammable and toxic clouds.

Finally, a dimensionless analysis was performed using the independent and dependent variables in the subsea gas release system. The simulation results for rise time, surface mass flux and surface gas concentrations from the expanded model were converted into their dimensionless forms and utilized to generate a nomograph. The nomograph was constructed for the subsea release of sour gas with H_2S composition of 11 % by mass from shallow waters such as the Arabian Gulf. The uncertainty of the parameters computed from the nomograph are dependent on the uncertainties of the simulations results and are reasonable. Therefore the nomograph can be used

by safety engineers to obtain valuable parameters that will provide guidance for further consequence modeling and defining exclusions zones that will aid in risk assessment and emergency response planning.

14 FUTURE WORK

Further work on the model and nomograph is necessary to improve the accuracy and reliability of the risk assessment of subsea sour gas releases in shallow waters.

The future work for the CFD model is as follows:

- Implementation of ocean stratification, include effects of water salinity on the different mechanisms governing the bubble plume.
- Account for the effects of ocean currents on the gas released underwater, by including velocity inlet boundary conditions for the sides of the water body.
- Usage of a mass transfer coefficient formulation that is more specific to the case of H_2S gas in water, by adding user defined functions to the model.
- Performing a sensitivity analysis using different drag models to determine the model that models the susbsea gas release phenomena closed to reality.

The future work for the nomograph is as follows:

- Conduct more simulations for more release depths, release mass flow rates, and release hole diameters to capture the relationships between results more accurately. This will aid is reducing the uncertainties arising from the regression modeling in the results obtained from the nomograph.
- Account for different sour gas compositions so a more generalized nomograph can be constructed.
- Account for different release directions, as in reality the hole in the pipeline can be found sideways or downwards instead of vertically upwards.

REFERENCES

1. Olsen JE, Skjetne P. Current Understanding of Subsea Gas Release: A Review. *Can J Chem Eng*. 2016;94:209-219.

2. Premathilake LT, Yapa PD, Nissanka ID, Kumarage P. Impact on Water Surface due to Deepwater Gas Blowouts. *Mar Pollut Bull*. 2016;112(1-2):365-374. doi:10.1016/j.marpolbul.2016.07.038

3. Xinhong L, Guoming C, Renren Z, Hongwei Z, Jianmin F. Simulation and Assessment of Underwater Gas Release and Dispersion from Subsea Gas Pipelines Leak. *Process Saf Environ Prot*. 2018;119:46-57. doi:10.1016/j.psep.2018.07.015

4. Ditmars JD, Cederwall K. *Analysis of Air-Bubble Plumes*. Pasadena, California; 1970.

5. Milgram JH, Burgess JJ. Measurements of the Surface Flow Above Round Bubble Plumes. *Appl Ocean Res*. 1984;6(1):40-44.

6. Bettelini MSG, Fanneløp TK. Underwater Plume from an Instantaneously Started Source. *Appl Ocean Res*. 1993;15(4):195-206. doi:10.1016/0141-1187(93)90008-L

7. Swan C, Moros A. The Hydrodynamics of a Subsea Blowout. *Appl Ocean Res*. 1993;15(5):269-280. doi:10.1016/0141-1187(93)90016-Q

8. Cloete S, Olsen JE, Skjetne P. CFD Modeling of Plume and Free Surface Behavior Resulting from a Sub-sea Gas Release. *Appl Ocean Res*. 2009;31(3):220-225. doi:10.1016/j.apor.2009.09.005

9. Skjetne P, Olsen JE. A Parcel Based Modelling Concept for Studying Subsea Gas Release and the Effect of Gas Dissolution. *Prog Comput Fluid Dyn*. 2012;12:187-195.

10. Olsen JE, Skjetne P. Modelling of Underwater Bubble Plumes and Gas Dissolution with an Eulerian-Lagrangian CFD Model. *Appl Ocean Res*. 2016;59:193-200. doi:10.1016/j.apor.2016.06.001

11. Wu K, Cunningham S, Sivandran S, Green J. Modelling Subsea Gas Releases and Resulting Gas Plumes Using Computational Fluid Dynamics. *J Loss Prev Process Ind*. 2017;49:411-417. doi:10.1016/j.jlp.2017.08.008

12. Friedl MJ, Fanneløp TK. Bubble Plumes and their Interaction with the Water Surface. *Appl Ocean Res*. 2000;22(2):119-128. doi:10.1016/S0141-1187(99)00022-X

13. Innomar. Surveys in Shallow Water. Innomar Technologie GmbH. https://www.innomar.com/application-shallow-water.php. Accessed January 9, 2018.

14. Olsen JE, Skjetne P. Governing Physics of Shallow and Deep Subsea Gas Release. *Prog Appl CFD*. 2014:217-222.

15. Markatos NC. The Mathematical Modelling of Turbulent Flows. *Appl Math Model*. 1986;10:190-220. doi:10.1016/B978-0-7506-6165-2.50036-9

16. Argyropoulos CD, Markatos NC. Recent Advances on the Numerical Modelling of Turbulent Flows. *Appl Math Model*. 2015;39(2):693-732. doi:10.1016/j.apm.2014.07.001

17. Janicki G, Schlöter S, Hennig T, Deerberg G. Simulation of Subsea Gas Hydrate Exploitation. *Energy Procedia*. 2014;59:82-89. doi:10.1016/j.egypro.2014.10.352

18. Levine JS, Haljasmaa I, Lynn R, Shaffer F, Warzinski RP. *Detection of Hydrates on Gas Bubbles During a Subsea Oil/Gas Leak*. Pittsburgh: EPAct Technical Report Series; 2015. http://www.netl.doe.gov/research/on-site-research/publications/featured-technicalreports.

19. Socolofsky SA, Adams EE, Sherwood CR. Formation Dynamics of Subsurface Hydrocarbon Intrusions Following the Deepwater Horizon Blowout. *Geophys Res Lett*. 2011;38(9):2-7. doi:10.1029/2011GL047174

20. Socolofsky SA, Adams EE. Role of Slip Velocity in the Behavior of Stratified Multiphase Plumes. *J Hydraul Eng*. 2005;131(4):273-282. doi:10.1061/(ASCE)0733-9429(2005)131:4(273)

21. Socolofsky SA, Adams EE. Multi-phase Plumes in Uniform and Stratified Crossflow. *J Hydraul Res*. 2002;40(6):661-672. doi:10.1080/00221680209499913

22. Kobus HE. Analysis of the Flow Induced by Air-Bubble Systems. In: *11th Conference on Coastal Engineering*. London: Coastal Engineering Research Council; 1968:1016-1031.

23. Topham DR. *Hydrodynamics of an Oilwell Blowout*. Victoria, BC; 1975.

24. Milgram JH. Mean Flow in Round Bubble Plumes. *J Fluid Mech*. 1983;133:345-376.

25. Rye H, Brandvich PJ. Verification of Substance Oil Spill Models. In: *International Oil Spill Conference*. Fort Lauderdale, FL, USA; 1997.

26. Li X, Chen G, Khan F. Analysis of Underwater Gas Release and Dispersion Behavior to Assess Subsea Safety Risk. *J Hazard Mater*. 2019;367(December 2018):676-685. doi:10.1016/j.jhazmat.2019.01.015

27. Fanneløp TK, Sjoen K. *Hydrodynamics of Underwater Blowouts*. Pasadena, California; 1980.

28. Einarsrud KE, Brevik I. *Kinetic Energy Approach to Dissolving Axisymmetric Multiphase Plumes*. Trondheim; 2013. doi:10.1061/(ASCE)HY.1943-7900.0000128

29. Hussein MA. *Investigating the Gas Dispersion from Subsea Gas Releases in Shallow Waters*. [masters thesis] Doha: Texas A&M University at Qatar; 2018.

30. ANSYS Fluent Theory Guide. http://www.pmt.usp.br/academic/martoran/notasmodelosgrad/ANSYS Fluent Theory Guide 15.pdf. Published 2013.

31. Versteeg HK, Malalasekera W. *An Introduction to Computational Fluid Dynamics The Finite Volume Method*. second edi. Pearson Education Limited; 2007.

32. Dewar M, Sellami N, Chen B. Dynamics of Rising CO_2 Bubble Plumes in the QICS Field Experiment Part 2 – Modelling. *Int J Greenh Gas Control*. 2015;38:52-63. doi:10.1016/j.ijggc.2014.11.003

33. Hibiki T, Ishii M. Two-Group Interfacial Area Transport Equations at Bubbly-to-Slug Flow Transition. *Nucl Eng Des*. 2000;202:39-76.

34. Hughmark GA. Mass and Heat Transfer from Rigid Spheres. *AIChE J*. 1967;13(6):1219-1221. doi:10.1002/aic.690130638

35. Milgram JH, Van Houten RJ. Plumes from Subsea Well Blowouts. In: *Conference on the Behavior of Off-Shore Structures*. 1982:659-684.

36. Løes M, Fanneløp TK. Concentration Measurements Above an Underwater Release of Natural Gas. *SPE Drill Eng*. 1989;(June):171-178.

37. Engebretsen T, Sjoen K, Northug T, Fannelop TK. Surface Flow and Gas Dispersion from a Subsea Release of Natural Gas. *Int Soc Offshore Polar Eng*. 1997.

38. Johansen Ø, Rye H, Cooper C. DeepSpill — Field Study of a Simulated Oil and Gas Blowout in Deep Water. *Spill Sci Technol Bull*. 2003;8(5-6):433-443. doi:10.1016/S1353-2561(02)00123-8

39. Diffusion Coefficients of Gases in Water. Engineering Toolbox. https://www.engineeringtoolbox.com/diffusion-coefficients-d_1404.html. Published 2008. Accessed November 4, 2020.

40. Warneck P, Williams J. The Atmospheric Chemist's Companion: Numerical Data for Use in the Atmospheric Sciences. *Springer Verlag*. 2012. doi:10.1007/978-94-007-2275-0

41. Sander SP, Abbatt J, Barker JR, et al. Chemical Kinetics and Photochemical Data for Use in Atmospheric Studies. *Jet Propuls Lab*. 2011;17(10-6). http://jpldataeval.jpl.nasa.gov.